666

NACA TN 2626

TECH LIBRARY KAFB, NM
0065728

NATIONAL ADVISORY COMMITTEE FOR AERONAUTICS

TECHNICAL NOTE 2626

AN INVESTIGATION OF BENDING-MOMENT DISTRIBUTION ON A MODEL HELICOPTER ROTOR BLADE AND A COMPARISON WITH THEORY

By John R. Meyer, Jr.

Massachusetts Institute of Technology

Washington
February 1952

AFMDC
TECHNICAL LIBRARY
AFL 2811

TECH LIBRARY KAFB, NM
0065728

NATIONAL ADVISORY COMMITTEE FOR AERONAUTICS

TECHNICAL NOTE 2626

AN INVESTIGATION OF BENDING-MOMENT DISTRIBUTION ON A MODEL HELICOPTER ROTOR BLADE AND A COMPARISON WITH THEORY

By John R. Meyer, Jr.

SUMMARY

Bending-moment distributions were measured on a model helicopter rotor blade under hovering and simulated forward-flight conditions. The hinged-blade configuration was tested up to an advance ratio μ of 0.50, whereas the fixed-at-root configuration was investigated up to and including $\mu = 0.90$.

Curves of maximum-bending-moment distribution are presented for all test conditions. Harmonic bending moments have been found as a result of a harmonic analysis of the data for $\mu = 0.22$ and $\mu = 0.47$. Theoretical calculations have been carried out at advance ratios of 0.22 and 0.47 for the hinged- and fixed-at-root conditions, respectively, and comparisons are made between experimental and theoretical results. Agreement between the results is reasonable in view of the assumptions made in the theory and the experimental errors involved.

Resonance studies have been made on three sets of blades of different stiffnesses for the purpose of comparing the experimentally determined resonance peaks with those indicated by theory.

Aerodynamic-loading expressions are developed for the fixed-at-root blade which include the effect of elastic flapping. These results are used in the Goodyear method which is modified for the fixed-at-root condition.

INTRODUCTION

The purpose of the present program, which was conducted at M.I.T. under the sponsorship and with the financial assistance of the National Advisory Committee for Aeronautics, was to investigate the possibility of measuring bending moments on a small-scale wind-tunnel model at advance ratios up to $\mu = 1.0$.

Present theory permits the calculation of blade bending-moment distributions which are correct only to the degree of validity of the aerodynamic loading applied to the blade. At the present stage of development of rotor aerodynamic theory no method exists for the evaluation of the induced flow through the rotor in forward flight, and it is therefore necessary to approximate the aerodynamic loading. Consequently, the bending moment takes on a distribution and maximum value which is known to be in error. A reliable method of measuring bending-moment distributions on a rotor blade by means of wind-tunnel tests with small-scale models offers a possibility of checking present theory, determining the extent of the errors involved, and establishing the importance of higher harmonic bending moments not readily susceptible to theoretical analysis.

Since one of the important limitations on more general helicopter utility is the relatively low maximum speed attainable with flexible flapping blades, it may be desirable to extend the helicopter speed range possible by using rigid nonflapping blades. This immediately imposes a structural problem since the alternating stresses are expected to be high. This program has therefore also included tests beyond the present-day normal operating range for the purpose of contributing some information toward the evaluation of these stresses.

SYMBOLS

a	slope of lift curve
c	blade-section chord, feet
L	rotor lift, pounds
m	mass of blade per foot of radius, slugs per foot
r	radial distance to blade element, feet
R	blade radius, feet
U_T	component at blade element of resultant velocity perpendicular to blade-span axis and to axis of no feathering, feet per second
U_P	component at blade element of resultant velocity perpendicular both to blade-span axis and U_T, feet per second
v	induced inflow velocity at rotor, feet per second

V true airspeed of helicopter along flight path, feet per second

α rotor angle of attack, positive when shaft axis is pointing rearward

β blade flapping angle at particular azimuth position

θ blade-section pitch angle

μ tip-section ratio $\left(\frac{V \cos \alpha}{\Omega R}\right)$

ρ mass density of air, slugs per cubic foot

τ aerodynamic loading, pounds per foot

ψ blade azimuth angle measured from downwind position in direction of rotation

λ inflow ratio $\left(\frac{V \sin \alpha - v}{\Omega R}\right)$

Ω rotor angular velocity, radians per second

DESCRIPTION OF APPARATUS

The model rotor under test in this program consisted of a three-blade system 5 feet in diameter. The blades had the NACA 0015 profile, a rectangular plan form with no twist, and a chord of 3 inches. The rotor hub had horizontal hinges located at a radius of $1\frac{1}{8}$ inches to permit flapping motion and lag hinges with damping located at a radius of $2\frac{7}{8}$ inches. Each blade had a 3/8-inch screw at its root coincident with the quarter-chord line which fitted into a tapped split sleeve with clamping screws on the hub which enabled the blade to be set and held at any desired pitch.

The blade construction consisted of an aluminum tubular spar enclosed in a balsa profile as shown in figure 1. These pictures show the stages of assembly and the resulting aerodynamically clean surface of the instrumented blade. A 3/4-inch-diameter aluminum tube (1/32-in. wall thickness) was rolled down into one having an oval cross section

measuring 0.30 by 1.00 inch. A root fitting was then inserted and riveted in one end and 10 pairs of strain gages were attached to the tube at radial stations shown in figure 2. Two balsa sheets were routed out so that one-half of the spar would fit into each piece. The three parts were then glued and clamped together and the profile was cut by a special tool placed in a jointer. After sanding to the proper shape, the blade was balanced about the quarter chord by inserting small lead weights in the leading edge. The two dummy blades were constructed in the same manner but did not have strain gages attached to the spar. The resulting blades had a bending stiffness of 16,000 pound-inches^2.

The slip-ring and brush assembly consisted of a total of seven rings and three sets of brushes. Six rings were made of coin silver, whereas the seventh consisted of Bakelite equipped with contacts for the purpose of indicating azimuth position. The silver graphite brushes were mounted in Bakelite holders and brush pressure was supplied by a coil spring fitted into a brass cap which screwed into the brush holder.

In order to measure the bending moment at different stations successively without stopping the rotor between readings, a solenoid stepping switch was provided which made it possible to insert any desired pair of strain gages into the bridge. The axially symmetric switch was mounted coaxially with the center of rotation and the two leads from the solenoid were attached to two of the six silver rings.

It was found that, in order to minimize the effects of slip-ring and brush resistance variations, it was necessary to mount all four arms of the resistance bridge on the rotor. Two dummy strain gages were therefore mounted on small metallic blocks which in turn were mounted on rubber pads and placed close to the center of rotation. It should be noted that a pair of strain gages forming two arms of a Wheatstone bridge are mounted at each station so as to cancel out centrifugal strains and to measure pure bending.

A Hathaway type MRC-12 strain-gage control unit was used for the purpose of amplifying the bridge unbalance. This unit is a compact, portable six-channel amplifier and power supply. The unit contains a 2000-cycle-carrier oscillator element which supplies voltage to the bridge circuit. Its amplifier drives a Consolidated oscillograph galvanometer type 7-112 having a sensitivity of 30 inches per milliampere from the voltage output of a strain-gage bridge.

Since there were 10 strain-gage stations on the blade and only 6 channels for amplification, it was necessary to have two stations alternately on one channel. A channel-selector control box was made with a stepping switch identical to the one on the rotor and synchronized with it so as to insert the gages into the proper channels. It should be noted that only one galvanometer was used since four slip rings

allow only one strain-gage bridge to be energized at any instant. The switch in the channel-selector control box also connected the galvanometer to the proper amplifier output channel.

Two rotor mounts were provided for the hovering and tunnel tests. The conical hovering mount is shown in figure 3 where the rotor disk was approximately 10 feet above the floor. The drive motor was mounted with its shaft in a vertical position inside the cone and the rotor was connected to the motor by means of two universal couplings and a short shaft. Figures 4 and 5 show the streamline mount for the 5- by $7\frac{1}{2}$-foot wind-tunnel tests. Here the motor was slung underneath the mount and a comparatively long shaft was provided with a universal joint at each end. The mount could be tilted in the fore-and-aft direction to obtain the desired inclination of the shaft axis.

PROCEDURE

The sensitivity of the entire strain-gage and recording system was obtained by a calibration of the galvanometer deflection against known bending moments which were applied to the instrumented blade. The flapping hinge was locked so that the blade was horizontal and known forces were applied at the tip of the blade. The sensitivity of each station was thereby obtained in terms of bending moment per inch of galvanometer deflection. The radial load was not simulated in general during calibration since centrifugal loads theoretically cancel at each station when the top and bottom strain gages occupy adjacent arms of a bridge. A check was made by putting a typical test blade in tension on a test rig with the result that there was not a complete cancellation of stresses probably because of small eccentricities. In any event if there were a possibility that the centrifugal loads would not cancel exactly, the effect would be taken into account in the zero reading recorded at each test rotational speed.

The general procedure for obtaining bending-moment data was to set the blades at zero pitch and balance out 5 of the 10 stations successively. The rotor was then brought up to a desired speed and the galvanometer reading for each of the five stations was recorded. The same procedure was carried out for the remaining five stations. The pitch setting was then changed to that desired for the test and the procedure described above was repeated. In the tunnel tests, the zero pitch-setting readings were taken with the tunnel off so that only the effects of centrifugal force and blade weight were taken into account. The bending moment was then a measure of the distance from the line of the record established at $\theta = 0^{\circ}$ and the trace at another pitch setting multiplied by the proper sensitivity factor.

With regard to blade twist due to the inclination of the blade principal axis of inertia to the plane of rotation, the effect was found to be small so no correction to θ_0 was made. This was concluded from the knowledge of the blade torsional stiffness and a calculation of the torsional moments acting on the blade at operating rotor speeds.

DISCUSSION

Instrumentation

Since the hinged rotor blade described was expected to be subjected to a maximum bending moment of the order of only 10 inch-pounds, it was necessary to use a rather sensitive system in this investigation. A direct recording galvanometer (Consolidated type 7-112) in conjunction with an amplifier was found satisfactory and resulted in an over-all system sensitivity of approximately 10 inch-pounds per inch (ratio of bending moment applied to blade over oscillograph screen deflection). This figure varied slightly with the station and channel. Under these conditions the slip-ring and brush disturbances were at first intolerable but eventually were reduced to a negligible level by insuring against dirt on the rings, providing a good running fit between brush and bushing, and eliminating any movement between the spring and cap in the brush holder by soldering the spring in the cap. When the fixed-at-root condition was tested, a system sensitivity of approximately 40 inch-pounds per inch was used, since the moments were larger, with the result that the slip-ring hash was at an even lower level.

A number of blades of different stiffnesses were tested in the hovering condition with strain gages at only one station inboard. A blade having a bending stiffness of 3000 pound-inches^2 was available whose construction consisted of an aluminum spar (1/8 by 3/4 in.) inserted in the leading edge of an NACA 0012 balsa profile. It was found that this blade underwent appreciable strain during rotational tests but very small bending moments resulted because of the low stiffness. The errors in the bending-moment measurements resulting from this condition were as much as 25 percent. Consequently, a blade having a stiffness of 60,000 pound-inches^2 was made in a manner similar to the final test blade described in the section "Description of Apparatus" using a steel tubular spar in an NACA 0015 profile with a pair of strain gages located at $r/R = 0.40$. The result was a blade with larger bending moments under operating conditions but smaller strains which were difficult to record with any degree of accuracy. From these considerations a blade having a stiffness of 20,000 pound-inches^2 was decided upon and an aluminum-spar blade was constructed with a pair of strain gages located at $r/R = 0.35$. The actual stiffness on the resulting blade was 16,000 pound-inches^2 and it was found to be satisfactory in the hovering

tests since the degree of accuracy with which bending moments could be measured was within 10 percent. The final set of three blades was then made with this stiffness as discussed in the section "Description of Apparatus." Compared with the Sikorsky R-6 full-scale rotor blade which has a stiffness of 3.24×10^6 pound-inches^2 at the 50-percent-spar station, the model blade used in these tests is 94 times stiffer based on the results of the development in appendix A.

Test Results

Hovering condition.- Typical hovering test results are shown in figures 6(a) and 6(b) for the hinged- and fixed-at-root conditions, respectively. Theoretical calculations have been carried out and the results are superimposed on the experimental results for the ease of comparison. A number of aerodynamic loadings were put into the Goodyear method (reference 1) for calculating steady-state bending-moment distributions of hinged rotor blades. Figure 6(a) shows the experimental curve and the theoretical distributions for uniform inflow with no tip loss, uniform inflow with 3-percent tip loss, and inflow variation with no tip loss. The effect of including a 3-percent tip loss lowers the curve in general compared with the no-tip-loss curve and produces a region of negative bending moment in the neighborhood of the tip. Although no negative bending moments were obtained near the tip, the possibility of a bending-moment reversal occurring farther outboard than the last strain-gage station is allowed for as shown in figure 6(a). The inflow variation (no tip loss included) was calculated according to Knight (reference 2) and the modified aerodynamic loading was used in the bending-moment calculation. The resulting distribution conforms quite closely to that of the experimental result in the region of the outboard 50 percent of the blade but fails to agree with the maximum moment indicated by the tests.

Figure 6(b) shows a comparison of theoretical and experimental rotor-blade bending-moment distributions for the hovering, fixed-at-root condition. The theoretical calculations were made in accordance with the modified Goodyear method developed in appendix E of this report. The aerodynamic loadings used in this method were the same as for the case of the hinged blade. It can be seen from figure 6(b) that there is little difference between the results when using a tip loss of 3 percent and an inflow variation. The experimental distribution is shown to be in good agreement with the theoretical calculations.

In the above calculations for the aerodynamic loading a two-dimensional lift-curve slope of 6.0 per radian was assumed for the hinged- and fixed-at-root conditions.

Simulated forward flight.- The wind-tunnel tests for the hinged-at-root condition were run at a constant rotor speed, pitch setting, and shaft inclination. The tunnel speed was varied to obtain advance ratios of 0.10, 0.22, 0.30, 0.40, and 0.50. It was found that a μ of 0.50 was the maximum that could be safely obtained because of an excessive amount of flapping and vibration. Figures 7(a) to 7(e) are traces from the oscillograph records. The different scales on the ordinates of these tracings are due to the different sensitivities of the amplifier channels and bridges. For a given station the bending-moment trace varied within 10 percent from one cycle to the next for the hinged-at-root condition. An average cycle was therefore chosen for presentation in these plots. The pronounced fifth-harmonic bending moment is present because of resonance with first-mode blade bending and contributed a large amount to the total bending moment. Stations 1 to 3 are not shown since the signals were small compared to the hash level.

Figure 8 shows the family of maximum-bending-moment curves and the test conditions under which the data were obtained. These bending moments occurred at an azimuth angle of approximately 235° for all the advance ratios tested. The bending moments decreased in going from a μ of 0.10 to $\mu = 0.30$ because of the rather fictitious conditions which were set up in the tunnel since the effect of a variation in μ alone (by changing tunnel speed and keeping rotational speed constant) on bending moment was desired. The bending-moment traces show a decrease in the steady-state (mean) value as μ is increased at a constant α, θ, and rotor speed indicating a decrease in lift. However, as μ is increased above 0.30, the first- and fifth-harmonic contributions have become larger and account for the increases in the magnitudes of the maximum-bending-moment distribution.

The bending moment at a station on the blade may be expressed as a Fourier series:

$$M = M_0 + M_a \cos\psi + M_b \sin\psi + M_{2a} \cos 2\psi + M_{2b} \sin 2\psi +$$

$$M_{3a} \cos 3\psi + M_{3b} \sin 3\psi + \ldots$$

The coefficients of this harmonic series have been determined by a graphical method presented in appendix B. The results of a harmonic analysis for $\mu = 0.22$ are presented in figure 9. It can be seen here how large the fifth-harmonic sine coefficient is when compared with the other components. The second, third, and fourth harmonics were negligible and the fifth-harmonic cosine component is not shown since it was also small. It should be mentioned that more points do not appear on the plots in the vicinity of the tip since the moments are small here and a harmonic analysis is difficult and probably inaccurate under these

circumstances. It is felt that the points which determine the critical portion of the curve are presented.

It was desirable to obtain some theoretical check on the data discussed above. Therefore calculations were carried out using the Goodyear tabular-dynamic method (reference 1) to find the first-harmonic sine component of the bending-moment distribution. The steady-state component was also computed from this reference. Another method for calculating harmonic bending moments was investigated since it was considered a relatively new approach to the problem which offered possible advantages over other methods. The De Guillenchmidt method (reference 3) is discussed in appendix C and calculation tables with an example are presented. The results of the above computations are presented in figures 10 and 11 where a comparison between the two theoretical approaches and the experimental results can be made. It should be emphasized that the same aerodynamic loadings were used in the Goodyear and De Guillenchmidt methods so that any differences in the results are due to the methods alone. In obtaining these aerodynamic loadings, no tip loss, constant induced flow, and a lift slope of 6.0 were assumed. The magnitudes of the corresponding bending-moment distributions are in reasonable agreement. However, the shapes of the theoretical and experimental curves are different probably because of the aerodynamic loading which was assumed for the calculations. There is good agreement between theory and experiment in regard to the azimuth position at which the maximum bending moment occurs as noted in figure 10. It may be seen from this figure that the magnitude of the experimental curve is larger than the theoretical result. The factor contributing to the discrepancy here is the fifth harmonic present in the experimental result but lacking in the theoretical result since no fifth-harmonic loadings were put into the calculations and therefore a fifth-harmonic bending moment could not possibly result. In general, comparison between theory and experiment indicates that present methods of computing blade bending moments are not satisfactory probably because of the inability of theory to provide the aerodynamic loading to make it possible to calculate the bending-moment distribution which actually exists on a given blade under operating conditions.

It was also planned to carry out the wind-tunnel tests for the fixed-at-root condition at a constant rotor speed, pitch setting, and shaft-axis inclination, but as high advance ratios were approached it was found necessary to decrease the rotor speed to 500 rpm in order to insure against overloading the blade. Data were therefore obtained at advance ratios of 0.80 and 0.90 at a lower rotor speed than the lower values of μ, but, in spite of these precautions, on attempting to obtain $\mu = 1.0$ the instrumented blade failed in fatigue and proceeded down the diffuser section of the tunnel. The aluminum-spar failure occurred just outboard of a steel insert at the root of the blade.

Figures 12(a) to 12(f) are the bending-moment traces from the oscillograph records for the fixed-at-root condition from $\mu = 0.15$ to $\mu = 0.90$. The scale of the vertical axis (bending moment) varies from one station to another again because of the difference in the sensitivities of the amplifier channels. The cycles presented in these figures are considered typical of those occurring over the short time interval during which records were made. It should be noted that the cycles for a given condition repeated with negligible difference for the fixed-at-root condition. Data for stations near the tip are not shown since the oscillograph records showed mere ripples, indicating very small bending moments. At advance ratios of 0.80 and 0.90 the signal from station 10 was not available since the strain gage at this station failed.

Plots from the oscillograph records are given in figure 13 which shows the variation of bending moment at station 9 with azimuth position for the values of advance ratios tested. It may be noted that the azimuth position at which the maximum moment occurs changes as μ increases. The drop in bending moment from $\mu = 0.60$ to $\mu = 0.80$ is in agreement with the decrease in rotor speed and hence aerodynamic loading. However, at $\mu = 0.90$ with the lower rotor speed, the maximum bending moment exceeds that at $\mu = 0.60$ because of the increase in tunnel speed which resulted in an increase in aerodynamic loading. It is suspected that the maximum bending moment on the blade at failure was in the neighborhood of 200 inch-pounds which corresponds to a tensile stress of 20,000 pounds per square inch.

The oscillograph records for all the runs were analyzed for the purpose of obtaining the maximum spanwise bending-moment distributions and the azimuth positions at which they occurred. The results of this analysis are shown in figure 14 where the maximum spanwise bending-moment distributions for various μ conditions are given. Implicitly, these curves show the change in spanwise moment distribution for corresponding changes in tunnel or simulated forward-flight velocity for the fixed-at-root rotor configuration up to a μ of 0.60. The curves have been extrapolated to the center of rotation since no strain gages were located on the hub. The curve for $\mu = 0.80$ is below that for $\mu = 0.60$ because of the particular combinations of tunnel and rotor speeds used to obtain these advance ratios.

A harmonic analysis was carried out on the bending-moment traces for the $\mu = 0.47$ condition and the results are shown in figure 15. It is of interest to note that the first-harmonic components are of the same order of magnitude but of opposite sign and that there is a large contribution from the second-harmonic cosine component. The higher harmonics were found to be negligible.

In order to check the experimental results against theory for the fixed-at-root condition, it was first necessary to derive some convenient

expressions for the aerodynamic loadings under these conditions. This development is given in appendix D and considers only first-harmonic effects. The Goodyear method (reference 1) has been modified in appendix E for the purpose of calculating steady-state and first-harmonic bending-moment distributions for the fixed-at-root blade. Also included in appendix E is a method of iteration which is used to cope with the problem of coupling between the aerodynamic-loading components.

A comparison of the theoretical and experimental harmonic-bending-moment distributions for the fixed-at-root condition at $\mu = 0.47$ is presented in figure 16. There are a number of factors here which lead to the discrepancy between theory and experiment, namely the assumed constant induced velocity, the neglect of the reversed-flow region, and a probably high two-dimensional lift-curve slope ($a = 6.0$). In addition, no wind-tunnel wall corrections were applied since there are no reliable methods available by which such corrections can be estimated, particularly as they may affect harmonic bending moments. A comparison between maximum bending moments as discussed for the hinged-at-root case was not made since the second-harmonic cosine component of bending moment, which apparently plays a large part in determining the total bending moment on the fixed-at-root rotor blade, could not be readily calculated with the present development.

Resonance Studies

The problem of rotor-blade flapping vibration in the hovering condition was met with early in the investigation and an attempt was made to understand the problem and alleviate this condition. Rotor balance and shaft alinement were improved with the result that blade vibration was reduced only a small amount. It was noted that the vibration was a function of pitch setting, the effect being rather small at zero pitch. This indicated the source of trouble to be of an aerodynamic nature and further investigation showed that the vibratory frequency (cycles per revolution) of the rotor blade varied with rotational speed. A resonance condition was suspected.

A theoretical survey of blades having three different stiffnesses was made by carrying out a calculation of their natural bending frequencies as a function of rotational speed by the method of reference 4. The results of this calculation for the hinged- and fixed-at-root conditions are shown in figures 17(a) and 17(b), respectively, for blades having stiffnesses of 3000, 16,000, and 60,000 pound-inches^2. The intersections of these curves and the straight "per rev" lines are resonance conditions.

The resonance problem was further investigated to obtain a better understanding of the phenomenon. Tests were run on three sets of blades having stiffnesses of 3000, 16,000 and 60,000 pound-inches^2 in the

hovering condition. Oscillograph records, taken at small increments in rotational speed, gave the strain-gage response to blade vibration at pitch settings of 0° and 12°. These records were analyzed to obtain the steady-state or mean bending moment and the vibratory or resonance bending moment at a given rotor speed. Figure 18 gives two sample oscillograph records showing the resonance phenomenon and the above terms defined. It should be noted that the vibratory motion of the blade was not of constant magnitude but consisted of an irregular increase and decrease of the double amplitude at a constant rotor speed. In each case the maximum double amplitude has been considered and plots of the ratio of the maximum double amplitude of resonance bending moment to steady-state bending moment against rotational speed for different blades are shown in figure 19 for the hinged-at-root condition and figure 20 for the fixed-at-root condition ($\beta = 0^{\circ}$). Superimposed on each plot is the appropriate natural-frequency spectrum for convenience in comparing theory and experiment. Each peak of the resonance curve is labeled with the cycles per revolution obtained as a result of the oscillograph record analysis. This quantity refers not only to the peak but also to the neighborhood of the peak. For example figure 19(b) indicates an experimentally determined peak resonance condition of 6 cycles per revolution at 580 rpm, of 5 cycles per revolution at 735 rpm, of 4 cycles per revolution at 1000 rpm, and of 3 cycles per revolution at 1350 rpm. The intersections of the "per rev" lines and the theoretically determined first-natural-bending-frequency curve occur at rotational speeds very close to the above except in the case of the resonance condition of 3 cycles per revolution. This agreement carries through for the hinged-at-root-condition tests (fig. 19).

The calculations of the first natural bending frequencies for the fixed-at-root rotor-blade condition were based on a blade length of 2 feet instead of 2.5 feet since the root fitting had a stiffness of approximately 600,000 pound-inches^2 and the actual blade root was located at a radius of 6 inches. The agreement between theory and experiment is good for the low-stiffness blade but becomes worse as blade stiffness is increased. This root condition introduced contributions to the effective stiffness of the rotor system from the root fitting and flexibility of supporting structure which were not considered in the theory. It seems reasonable to assume that these effects would be of greater importance as blade stiffness is increased and this appears to be borne out by experimental results presented in figures 20(b) and 20(c).

A point of interest to be noted from figures 17 to 20 is the variation of the ratio of resonance bending moment to steady-state bending moment with blade stiffness. For the hinged-at-root condition, the blades having stiffnesses of 3000, 16,000, and 60,000 pound-inches^2 indicate maximum resonance-peak ratios of 1.0, 0.38, and 0.60, respectively.

Also for the same blades fixed at the root, the maximum resonance-peak ratios are 0.37, 0.20, and 0.47, respectively. In each condition note that the blade of relative medium stiffness experiences the lowest resonance level. It appears from this brief study that there is an optimum stiffness which will minimize blade resonance; however, it is felt that a general statement of this nature cannot be made at this time without a more thorough investigation of the resonance phenomenon in helicopter rotor blades.

CONCLUSIONS

Bending-moment distributions were measured on a model rotor blade under hovering and simulated forward-flight conditions in both the hinged- and fixed-at-root configurations and a comparison was made with theoretical calculations. It was found that:

1. For the hovering, hinged-at-root condition, the best agreement between theoretical and experimental bending-moment distributions was obtained when the inflow ratio variation according to NACA TN 626 was considered. No measurable amount of negative bending moment at the tip was found which indicates less tip loss than is usually assumed.

2. In the hovering, fixed-at-root condition, the experimental bending-moment distribution fell within the region determined by theoretical calculations obtained as a result of inserting different types of aerodynamic loading into the bending-moment calculations.

3. The fifth-harmonic bending moment due to resonance in the forward-flight, hinged-at-root condition is relatively large and accounted for much of the discrepancy between the theoretical and experimental total maximum bending moments. An appreciable difference between the general shape of the distributions predicted by theory and measured experimentally exists and is probably due to the distribution of aerodynamic loading assumed in the currently available theory.

4. In the case of the fixed-at-root, forward-flight condition, it was found that the second-harmonic bending moment was the largest component contributing to the total moment. The agreement between theory and experiment in regard to the steady-state and first-harmonic bending moments for an advance ratio of 0.47 was reasonable in view of experimental errors and the assumptions made in the theory.

5. A brief study of rotor-blade resonance phenomenon was made in the hovering condition. Good agreement between theory and experiment was obtained for the hinged-at-root condition since it was found that the experimental resonance peaks occurred at rotational speeds very close

to those where the natural-bending-frequency curves crossed the lines of cycles per revolution. Agreement in the case of the fixed-at-root condition was reasonable in view of the contributions to effective stiffness of the rotor system from the supporting structure.

6. Information regarding the actual aerodynamic loading or induced flow and blade resonance phenomenon is needed if the results of bending-moment calculations are to represent the actual situation existing on a rotor blade under operating conditions.

Massachusetts Institute of Technology
Cambridge, Mass., April 3, 1951

APPENDIX A

BASIS FOR COMPARISON OF STIFFNESSES OF VARIOUS ROTOR BLADES

Consider a blade under the loading $W = f(r)$. The deflection δ at the tip of a cantilever beam is:

$$\delta = \frac{WR^3}{3EI}$$

where R is the blade radius. Now

$$W(r) = \frac{1}{2}\rho a\alpha_r c\Omega^2 r^2\ dr - m'\ dr\ \Omega^2 r\ \frac{dz}{dr}$$

Let $x = \frac{r}{R}$ so $r = xR$ and $dr = R\ dx$. Then

$$W = \frac{\rho}{2}\ a\alpha_r c\Omega^2 R^3 x^2\ dx - m'\Omega^2 R^2 x\ dx\ \frac{dz}{dr}$$

Now m' is mass per unit length and $m' \propto L^2$ where L is the dimension of length. Also c and R have dimensions of length L. So

$$W \propto \Omega^2 R^2 L^2$$

From the deflection expression there is obtained:

$$\frac{\delta}{R} \propto \frac{WR^2}{EI} \propto \frac{(\Omega R)^2 L^4}{EI}$$

Equating the expressions for δ/R of the model and the full-scale blade, there is obtained:

$$\frac{(\Omega R)_M{}^2 L_M{}^4}{(EI)_M} = \frac{(\Omega R)_F{}^2 L_F{}^4}{(EI)_F}$$

where the subscripts M and F denote model and full scale, respectively. Hence,

$$(EI)_M = (EI)_F \frac{(\Omega R)_M^2 L_M^4}{(\Omega R)_F^2 L_F^4}$$

Comparing the R-6 blade and the model blade under test there is obtained:

$$\frac{L_M}{L_F} = \frac{2.5}{19.0} = 0.1315$$

$$\frac{L_M^4}{L_F} = 2.98 \times 10^{-4}$$

$$\frac{(\Omega R)_M^2}{(\Omega R)_F^2} = \frac{(210)^2}{(500)^2} = 0.176$$

From reference 1,

$$(EI)_F = 3.24 \times 10^6 \text{ lb-in.}^2$$

at $x = 0.50$; hence,

$$(EI)_M = 3.24 \times 10^6 \times 0.176 \times 2.98 \times 10^{-4} = 170 \text{ lb-in.}^2$$

This result means that a model of the R-6 rotor blade having a diameter of 5 feet and rotating at 800 rpm should have a stiffness EI of 170 pound-inches^2. The EI of the model blade investigated in this report was 16,000 pound-inches^2 and is therefore 94 times as stiff as a model of the R-6 when rotating at the above rotational speed.

APPENDIX B

GRAPHICAL METHOD FOR HARMONIC ANALYSIS OF A PERIODIC FUNCTION

Method.- Let the curve such as the one shown in the accompanying figure be represented by the following series:

$$y = b_0 + a_1 \sin x + b_1 \cos x + a_2 \sin 2x + b_2 \cos 2x + \ldots + a_n \sin nx + b_n \cos nx + \ldots$$

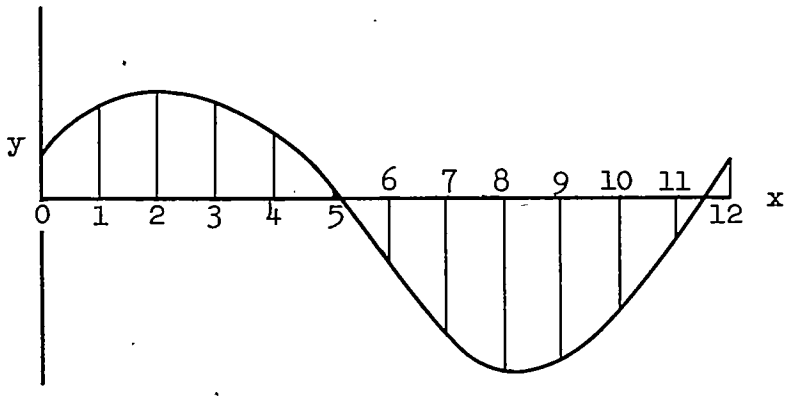

The curve is divided into 12 equal parts such that the distance between ordinates h is $\pi/6$, and the same ordinates are used in finding all harmonics.

In order to find the first-harmonic coefficients a_1 and b_1, the following construction is made: Starting from a point 0, $\frac{1}{2} y_0$ is laid out in the appropriate direction on the horizontal; y_1 is added to $\frac{1}{2} y_0$ at an angle of 30° to the horizontal; y_2 is added at an angle of 60°; and so forth. Note that when the ordinate is negative, it must be laid off in the opposite direction as shown in the figure on the following page.

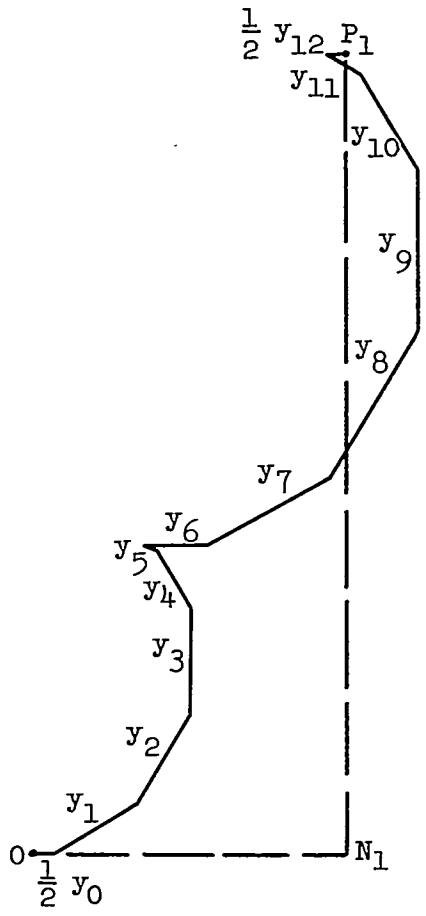

The coefficients a_1 and b_1 are found from the relations:

$$a_1 = \frac{1}{6} P_1N_1$$

$$b_1 = \frac{1}{6} ON_1$$

To find the coefficients of the second harmonic a similar construction is made, but the ordinates are laid out at intervals of 60° instead of 30°. The expressions for a_2 and b_2 are:

$$a_2 = \frac{1}{6} P_2N_2$$

$$b_2 = \frac{1}{6} ON_2$$

In general, the nth harmonic may be found by construction where the ordinates of the curve are laid out at intervals of $n(2\pi/M)$ where M is the number of parts into which the period of the curve is divided. The expressions for the coefficients are:

$$a_n = \frac{2}{M} P_n N_n$$

$$b_n = \frac{2}{M} ON_n$$

Proof of above construction.- The trapezoidal rule states that the total area under a curve is:

$$A = h\left(\frac{y_0}{2} + y_1 + y_2 + \ldots + \frac{y_n}{2}\right)$$

where h is the distance between ordinates, or $h = 2\pi/M$.

Now the Fourier series coefficients can be written:

$$a_1 = \frac{1}{\pi}\int_0^{2\pi} y \sin x \, dx$$

For the integral substitute the expression for the area given above:

$$a_1 = \frac{1}{\pi} h\left(\frac{1}{2} y_0 \sin 0^\circ + y_1 \sin 30^\circ + y_2 \sin 60^\circ + \ldots + \frac{1}{2} y_{12} \sin 360^\circ\right)$$

or

$$a_1 = \frac{2}{M}\left(\frac{1}{2} y_0 \sin 0^\circ + y_1 \sin 30^\circ + y_2 \sin 60^\circ + \ldots + \frac{1}{2} y_{12} \sin 360^\circ\right)$$

Also

$$b_1 = \frac{1}{\pi}\int_0^{2\pi} y \cos x \, dx$$

So

$$b_1 = \frac{2}{M}\left(\frac{1}{2} y_0 \cos 0^\circ + y_1 \cos 30^\circ + y_2 \cos 60^\circ + \ldots + \frac{1}{2} y_{12} \cos 360^\circ\right)$$

Now the graphical process described above is that indicated in the parentheses, thus:

$$a_1 = \frac{2}{M} P_1N_1$$

$$b_1 = \frac{2}{M} ON_1$$

Also

$$b_0 = \frac{1}{2\pi}\int_0^{2\pi} y\, dx = \frac{1}{2\pi} \times \frac{2\pi}{M}\left(\frac{1}{2} y_0 + y_1 + y_2 + \ldots \frac{1}{2} y_{12}\right)$$

Hence

$$b_0 = \frac{1}{M}\left(\frac{1}{2} y_0 + y_1 + y_2 + \ldots + \frac{1}{2} y_{12}\right)$$

APPENDIX C

DISCUSSION OF DE GUILLENCHMIDT METHOD FOR CALCULATION OF BENDING STRESSES IN HELICOPTER ROTOR BLADES

The development of this method for calculating bending stresses in rotor blades is given in reference 3. The procedure for the general method, the method as applied to the model rotor tested in this investigation, and sample calculations are discussed in this appendix.

Procedure for Calculation of Elastic Bending Moment

The procedure for calculating the elastic bending moment is as follows:

1. Calculate the natural frequencies and corresponding mode shapes of the nonrotating blade. Reference 3 states that the rotational and nonrotational natural modes are the same within a few percent. A calculation has been carried out on the R-6 rotor blade and the results are presented in figure 21 where it can be seen that the first natural mode does not vary greatly with rotational speed. The frequencies and mode for the model rotor blade were obtained by the use of the Myklestad method (reference 5, pp. 184-203). The rotating natural bending frequencies were calculated from the results of reference 4.

2. Calculate the aerodynamic loading (reference 1), the centrifugal loading, and the total external loading on the rigid blade at different azimuth positions. For the example illustrated here, eight positions spaced 45° apart were used as shown in tables I, II, and III. Curves of total external loading F_d' are shown in figure 22. No tip loss was included in the aerodynamic loading.

3. Then evaluate the integral $\int_0^R F_d'\eta_1 \, dx$ at the corresponding azimuth positions as illustrated in table IV. The mode functions η_1 and η_2 for this example are shown in figure 23.

4. The integral $\int_0^R m'\eta_1^2 \, dx$ is then evaluated as shown in table V.

5. Thus it is possible to calculate g_1 (table VI) for the eight azimuth positions. The plots of g_1 and g_2 are shown in figure 24. A harmonic analysis is performed on the g function using the graphical method described in appendix B of this report. This determines the values $g_{i,n}\begin{cases}a.\\b\end{cases}$

6. The calculation of $\int\int_x^R m'\eta_1 \, dx \, d\xi$ is one of the byproducts of the Myklestad computation since this integral is the ratio of the rigid-blade bending moment to the square of the natural frequency. This distribution and the elastic-blade bending-moment distribution broken down into harmonics are shown in table VII.

7. The elastic bending moment obtained from a consideration of the second natural mode of the blade is shown in table VIII. The bending moment resulting from both modes is shown in table IX. It was found that the maximum moment occurred at an azimuth position of approximately 225°.

Comments on De Guillenchmidt Method

The De Guillenchmidt method is particularly useful for the investigation of the effect of a series of loading conditions on a given blade. This is true because, once the natural frequencies and modes are determined, relatively little calculation is necessary to obtain both the harmonic- and total-bending-moment distributions for a given loading condition.

For the blade tested in this investigation, the calculations showed that the effect of including the second natural mode was negligible in the case of the steady-state component, whereas the effect on the sine and cosine components was appreciable. However, for full scale the contribution of the various modes to the bending moment must be investigated for each blade design.

APPENDIX D

CALCULATION OF EXPRESSIONS FOR AERODYNAMIC LOADING ON A FIXED-AT-ROOT ROTOR BLADE

The rotor blade discussed in this appendix is one which is fixed at the root but is allowed to bend under applied loads because of its elastic properties.

The lift on a blade element is:

$$\Delta L = \frac{1}{2}\rho ac\left(\theta U_T^2 + U_P U_T\right)\Delta r \tag{D1}$$

where

$$U_T = \Omega(r + \mu R \sin \Omega t) \tag{D2}$$

and

$$U_P = \lambda\Omega R - \dot{z} - \mu\Omega R \frac{dz}{dr} \cos \Omega t \tag{D3}$$

where z is the deflection of a blade element from the plane perpendicular to the axis of rotation and passing through the blade root. Now z can be written as:

$$z = r\beta + y_I + y_{II} \sin \Omega t + y_{III} \cos \Omega t + \ldots \tag{D4}$$

Only the first harmonic will be considered in this development; therefore:

$$\dot{z} = y_{II}\Omega \cos \Omega t - y_{III}\Omega \sin \Omega t \tag{D5}$$

and

$$\frac{dz}{dr} = \beta + \frac{dy_I}{dr} + \frac{dy_{II}}{dr} \sin \Omega t + \frac{dy_{III}}{dr} \cos \Omega t \tag{D6}$$

Hence

$$U_P = \lambda\Omega R - y_{II}\Omega \cos \Omega t + y_{III}\Omega \sin \Omega t -$$

$$\mu\Omega R \cos \Omega t\left(\beta + \frac{dy_I}{dr} + \frac{dy_{II}}{dr} \sin \Omega t + \frac{dy_{III}}{dr} \cos \Omega t\right) \tag{D7}$$

Substituting these quantities into the lift expression, equation (D1)

$$\tau = \frac{\Delta L}{\Delta r}$$

$$= \frac{1}{2}\rho ac\left\{\theta\Omega^2(r + \mu R \sin \Omega t)^2 + \left[\lambda\Omega R - y_{II}\Omega \cos \Omega t + y_{III}\Omega \sin \Omega t - \right.\right.$$

$$\left.\left.\mu\Omega R \cos \Omega t\left(\beta + \frac{dy_I}{dr} + \frac{dy_{II}}{dr} \sin \Omega t + \frac{dy_{III}}{dr} \cos \Omega t\right)\right] (\Omega r + \mu\Omega R \sin \Omega t)\right\}$$

Upon expanding and factoring out Ω^2 there is obtained:

$$\tau = \frac{1}{2}\rho ac\Omega^2\left(\theta r^2 + 2\theta\mu rR \sin \Omega t + \theta\mu^2R^2\sin^2\Omega t + \lambda rR + \right.$$

$$\lambda\mu R^2\sin \Omega t - y_{II}r \cos \Omega t - y_{II}\mu R \sin \Omega t \cos \Omega t +$$

$$y_{III}r \sin \Omega t + y_{III}\mu R \sin^2\Omega t - \mu rR\beta \cos \Omega t - \mu^2R^2\beta \cos \Omega t \sin \Omega t -$$

$$\mu rR \frac{dy_I}{dr} \cos \Omega t - \mu^2R^2 \frac{dy_I}{dr} \sin \Omega t \cos \Omega t - \mu rR \frac{dy_{II}}{dr} \sin \Omega t \cos \Omega t -$$

$$\mu^2R^2 \frac{dy_{II}}{dr} \cos \Omega t \sin^2\Omega t - \mu rR \frac{dy_{III}}{dr} \cos^2\Omega t -$$

$$\left.\mu^2R^2 \frac{dy_{III}}{dr} \sin \Omega t \cos^2\Omega t\right) \tag{D8}$$

This can be written as follows:

$$\tau = \frac{1}{2}\rho ac\Omega^2\Bigg(\theta r^2 + 2\theta\mu rR \sin \Omega t + \frac{\theta}{2}\mu^2R^2 - \frac{\theta}{2}\mu R^2 \cos 2\Omega t +$$

$$\lambda rR + \lambda\mu R^2 \sin \Omega t - y_{II}r \cos \Omega t - \frac{y_{II}}{2}\mu R \sin 2\Omega t + y_{III}r \sin \Omega t +$$

$$\frac{y_{III}}{2}\mu R - \frac{y_{III}}{2}\mu R \cos 2\Omega t - \mu\beta rR \cos \Omega t - \frac{1}{2}\mu^2\beta R^2 \sin 2\Omega t -$$

$$\mu rR \frac{dy_I}{dr} \cos \Omega t - \frac{\mu^2}{2}R^2 \frac{dy_I}{dr} \sin 2\Omega t - \frac{\mu}{2} rR \frac{dy_{II}}{dr} \sin 2\Omega t -$$

$$\frac{\mu^2}{4}R^2 \frac{dy_{II}}{dr} \cos \Omega t + \frac{\mu^2}{4}R^2 \frac{dy_{II}}{dr} \cos 3\Omega t - \frac{\mu}{2} rR \frac{dy_{III}}{dr} -$$

$$\frac{\mu}{2} rR \frac{dy_{III}}{dr} \cos 2\Omega t - \frac{\mu^2}{4}R^2 \frac{dy_{III}}{dr} \sin \Omega t - \frac{\mu^2}{4}R^2 \frac{dy_{III}}{dr} \sin 3\Omega t\Bigg) \qquad \text{(D9)}$$

Comparing equation (D9) with:

$$\tau = \tau_I + \tau_{II} \sin \Omega t + \tau_{III} \cos \Omega t + \ldots \qquad \text{(D10)}$$

the following expressions are obtained:

The steady-state loading:

$$\tau_I = \frac{1}{2}\rho ac\Omega^2\left[\theta r^2 + \frac{\theta}{2}\mu^2R^2 + \lambda rR + \frac{\mu R}{2}\left(y_{III} - r\frac{dy_{III}}{dr}\right)\right] \qquad \text{(D11)}$$

The first-harmonic sine component:

$$\tau_{II} = \frac{1}{2}\rho ac\Omega^2\left(2\theta r\mu R + \lambda\mu R^2 + y_{III}r - \frac{\mu^2R^2}{4}\frac{dy_{III}}{dr}\right) \qquad \text{(D12)}$$

The first-harmonic cosine component:

$$\tau_{III} = \frac{1}{2}\rho ab\Omega^2\left[-y_{II}r - \mu rR\left(\beta + \frac{dy_I}{dr}\right) - \frac{\mu^2R^2}{4}\frac{dy_{II}}{dr}\right] \tag{D13}$$

The above expressions are used in the application of the method of calculating rigid-blade bending moments developed in appendix E.

APPENDIX E

MODIFICATION OF GOODYEAR METHOD FOR CALCULATING FIXED-AT-ROOT ROTOR-BLADE BENDING MOMENTS

Discussion of Modification

In this appendix the Goodyear method (reference 1) for calculating hinged-rotor-blade bending moments will be modified so that rigid-blade moments may be determined.

First consider the steady-state analysis for a rigid blade (i.e., fixed at root but allowed to bend). The total shear at any point on the blade is:

$$S_t = F\left(\frac{dz}{dr}\right) + S = \frac{dM}{dr} \tag{E1}$$

where

S aerodynamic shear at a given point

F centrifugal shear at same point

M bending moment at given point

z deflection from plane perpendicular to axis of rotation and passing through blade root

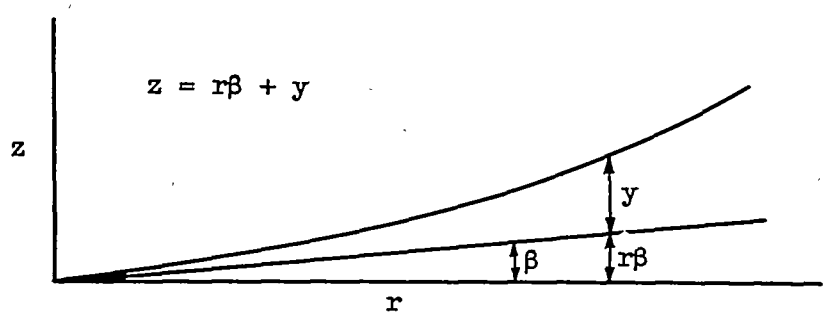

Now

$$z = r\beta + y_I + y_{II} \sin \Omega t + y_{III} \cos \Omega t + \ldots$$

So

$$\frac{dz}{dr} = \beta + \frac{dy_I}{dr} + \frac{dy_{II}}{dr} \sin \Omega t + \frac{dy_{III}}{dr} \cos \Omega t + \ldots$$

where y is the deflection measured from the undeflected position.

The steady-state component of dz/dr is $\beta + \frac{dy_I}{dr}$. Hence equation (E1) becomes:

$$\frac{dM}{dr} = F\left(\beta + \frac{dy_I}{dr}\right) + S \tag{E2}$$

This equation can be approximated by dividing the blade into an integral number of parts each of length X. Then dM/dr at the midpoint of an interval is:

$$\left(\frac{dM}{dr}\right)_{i+\frac{1}{2}} = \frac{M_{i+1} - M_i}{X}$$

Hence the above equation becomes:

$$M_{i+1} = M_i + F_{i+\frac{1}{2}} X\left(\beta + \frac{dy_I}{dr}\right)_{i+\frac{1}{2}} + XS_{i+\frac{1}{2}} \tag{E3}$$

Let

$$M_i = a_i + b_i Z \tag{E4}$$

where $Z = M_0$ = Bending moment at blade root.

At the blade tip:

$$M_n = a_n + b_n Z = 0$$

or

$$Z = -\frac{a_n}{b_n} \tag{E5}$$

Hence the bending moment at the root will be known once the values a_n and b_n are determined. To find the expressions for the a's and b's proceed as follows:

At the blade root:

$$M_0 = a_0 + b_0 Z$$

and

$$M_0 = Z \tag{E6}$$

Comparing these two equations there is obtained:

$$\left.\begin{aligned} a_0 &= 0 \\ b_0 &= 1 \end{aligned}\right\} \tag{E7}$$

Now

$$\left(\frac{dy}{dr}\right)_i = \sum_{j=0}^{i} \frac{M_j X}{EI_j} = \sum_{j=0}^{i} \left(a_j + b_j Z\right)\frac{X}{EI_j} \tag{E8}$$

Then equation (E3) can be written:

$$M_{i+1} = a_i + b_i Z + F_{i+\frac{1}{2}}\left(\beta X + \sum_{j=1}^{i} \frac{a_j X^2}{EI_j} + \sum_{j=0}^{i} \frac{b_j X^2 Z}{EI_j}\right) + XS_{i+\frac{1}{2}} \tag{E9}$$

Also equation (E4) can be written:

$$M_{i+1} = a_{i+1} + b_{i+1} Z \tag{E10}$$

Equating coefficients of equations (E9) and (E10):

$$a_{i+1} = a_i + XS_{i+\frac{1}{2}} + F_{i+\frac{1}{2}}\left(\beta X + \sum_{j=0}^{i} \frac{a_j X^2}{EI_j}\right) \tag{E11}$$

$$b_{i+1} = b_i + F_{i+\frac{1}{2}} \sum_{j=0}^{i} \frac{b_j X^2}{EI_j} \tag{E12}$$

Now consider the first-harmonic bending-moment analysis. The shear equation now reads:

$$\frac{dM}{dr} = F\left(\frac{dz}{dr}\right) + S + J_0 + \Omega^2 \int_0^r my\ dr \tag{E13}$$

where J_0 is the inertia shear at the root and the quantity $J_0 + \Omega^2 \int_0^r my\ dr$ is the inertia shear at r. The subscripts denoting the harmonic have been dropped since the solution takes the same form for the sine as for the cosine component.

Now $\Omega^2 \int_0^r my\ dr$ can be written as:

$$\sum_{j=1}^{i} m_j y_j \Omega^2 X \tag{E14}$$

and

$$\left(\frac{dz}{dr}\right)_{II} = \frac{dy}{dr} \tag{E15}$$

So

$$M_{i+1} = M_i + F_{i+\frac{1}{2}} X \left(\frac{dy}{dr}\right)_{i+\frac{1}{2}} + XS_{i+\frac{1}{2}} + XJ_0 + \sum_{j=1}^{i} X^2 \Omega^2 m_j y_j \tag{E16}$$

Let

$$M_i = a_i + b_i M_0 + c_i \phi \tag{E17}$$

and

$$y_i = U_i + V_i M_0 + W_i \phi \tag{E18}$$

where $\phi = XJ_0$. Now

$$y_i = \frac{X^2 M_0}{EI_0} + \left(\frac{X^2 M_0}{EI_0} + \frac{X^2 M_1}{EI_1}\right) + \ldots + \sum_{j=1}^{i-1} \frac{X^2 M_j}{EI_j} \tag{E19}$$

So

$$y_1 = \frac{X^2 M_0}{EI} = \frac{X^2}{EI}\left(a_0 + b_0 M_0 + c_0 \phi\right)$$

and equation (E18) gives:

$$y_1 = U_1 + V_1 M_0 + W_1 \phi$$

By comparison

$$U_1 = \frac{X^2}{EI} a_0$$

$$V_1 = \frac{X^2}{EI} b_0$$

$$W_1 = \frac{X^2}{EI} c_0$$

Proceeding further, equation (E19) gives:

$$y_2 = \frac{X^2 M_0}{EI} + \frac{X^2 M_0}{EI} + \frac{X^2 M_1}{EI}$$

or

$$y_2 = \frac{X^2}{EI}\left(a_0 + b_0 M_0 + c_0 \phi\right) + \frac{X^2}{EI}\left[a_0 + a_1 + \left(b_0 + b_1\right) M_0 + \left(c_0 + c_1\right) \phi\right]$$

Now

$$y_2 = U_2 + V_2M_0 + W_2\phi$$

By comparison

$$U_2 = U_1 + \frac{X^2}{EI}\left(a_0 + a_1\right)$$

$$V_2 = V_1 + \frac{X^2}{EI}\left(b_0 + b_1\right)$$

$$W_2 = W_1 + \frac{X^2}{EI}\left(c_0 + c_1\right)$$

It can be concluded that in general:

$$\left.\begin{aligned} U_{i+1} &= U_i + \sum_{j=1}^{i} \frac{X^2 a_j}{EI_j} \\ V_{i+1} &= V_i + \sum_{j=1}^{i} \frac{X^2 b_j}{EI_j} \\ W_{i+1} &= W_i + \sum_{j=1}^{i} \frac{X^2 c_j}{EI_j} \end{aligned}\right\} \qquad \text{(E20)}$$

Expressions for the a's, b's, and c's are found in the following manner:

Consider the bending moment at the blade root:

$$M_0 = M_0$$

Equation (E17) becomes

$$M_0 = a_0 + b_0M_0 + c_0\phi$$

So by comparison

$$a_0 = 0$$

$$b_0 = 1$$

$$c_0 = 0$$

Now consider equation (E16) with $i = 0$:

$$M_1 = M_0 + F_{1/2}X\left(\frac{dy}{dr}\right)_{1/2} + XS_{1/2} + \phi$$

Since

$$X\left(\frac{dy}{dr}\right)_{1/2} = \frac{X^2M_0}{EI}$$

then

$$M_1 = M_0 + F_{1/2}\frac{X^2M_0}{EI} + XS_{1/2} + \phi$$

Comparing this equation with

$$M_1 = a_1 + b_1M_0 + c_1\phi$$

there is obtained:

$$a_1 = XS_{1/2}$$

$$b_1 = 1 + F_{1/2}\frac{X^2}{EI}$$

$$c_1 = 1$$

Repeating this process for $i = 1$:

$$M_2 = M_1 + F_{1\frac{1}{2}} \frac{X^2}{EI}\left(M_0 + M_1\right) + XS_{1\frac{1}{2}} + \phi + X^2\Omega^2 m_1\left(U_1 + V_1 M_0 + W_1\phi\right)$$

or

$$M_2 = a_1 + b_1 M_0 + c_1\phi + F_{1\frac{1}{2}} \frac{X^2}{EI}\left(M_0 + a_1 + b_1 M_0 + c_1\phi\right) + XS_{1\frac{1}{2}} + \phi +$$

$$X^2\Omega^2 m_1\left(U_1 + V_1 M_0 + W_1\phi\right)$$

Since

$$M_2 = a_2 + b_2 M_0 + c_2\phi$$

then

$$a_2 = a_1 + XS_{1\frac{1}{2}} + F_{1\frac{1}{2}} \frac{X^2 a_1}{EI} + X^2\Omega^2 m_1 U_1$$

$$b_2 = b_1 + F_{1\frac{1}{2}} \frac{X^2}{EI}\left(1 + b_1\right) + X^2\Omega^2 m_1 V_1$$

$$c_2 = c_1 + F_{1\frac{1}{2}} \frac{X^2}{EI}\left(c_1\right) + 1 + X^2\Omega^2 m_1 W_1$$

It can be concluded that in general:

$$\left.\begin{aligned}
a_{i+1} &= a_i + F_{i+\frac{1}{2}} \sum_{j=1}^{i} \frac{X^2 a_j}{EI_j} + XS_{i+\frac{1}{2}} + X^2\Omega^2 \sum_{j=1}^{i} m_j U_j \\
b_{i+1} &= b_i + F_{i+\frac{1}{2}} \sum_{j=1}^{i} \frac{X^2 b_j}{EI_j} + X^2\Omega^2 \sum_{j=1}^{i} m_j V_j \\
c_{i+1} &= c_i + F_{i+\frac{1}{2}} \sum_{j=1}^{i} \frac{X^2 c_j}{EI_j} + 1 + X^2\Omega^2 \sum_{j=1}^{i} m_j W_j
\end{aligned}\right\} \qquad \text{(E21)}$$

It is known that

$$XJ_0 = -\sum_{j=1}^{j=n} X^2\Omega^2 m_j y_j = \phi$$

as defined earlier where n is the tip station. Substituting equation (E18) for y_i in the above:

$$\phi = -\sum_{j=1}^{n} X^2\Omega^2 m_j U_j + M_0 \sum_{j=1}^{n} X^2\Omega^2 m_j V_j + \phi \sum_{j=1}^{n} X^2\Omega^2 m_j W_j \tag{E22}$$

The summations are determined from the calculation. Let them be:

$$\left.\begin{aligned} N_1 &= \Sigma X^2\Omega^2 m_j U_j \\ N_2 &= \Sigma X^2\Omega^2 m_j V_j \\ N_3 &= \Sigma X^2\Omega^2 m_j W_j \end{aligned}\right\} \tag{E23}$$

Then equation (E22) becomes:

$$\phi = -N_1 - N_2 M_0 - N_3\phi$$

or

$$\phi\left(1 + N_3\right) + N_2 M_0 = -N_1 \tag{E24}$$

Also, at the tip,

$$M_n = a_n + b_n M_0 + c_n\phi = 0$$

Hence

$$\phi = -\frac{a_n}{c_n} - \frac{b_n}{c_n} M_0 \tag{E25}$$

Substituting this expression for ϕ into equation (E24):

$$(1 + N_3)\left(-\frac{a_n}{c_n} - \frac{b_n}{c_n} M_0\right) + N_2 M_0 = -N_1$$

Therefore

$$M_0 = \frac{\frac{a_n}{c_n}\left(1 + N_3\right) - N_1}{N_2 - \frac{b_n}{c_n}\left(1 + N_3\right)} \tag{E26}$$

Knowing M_0, ϕ may be obtained and hence M_1 from the expression $M_1 = a_1 + b_1 M_0 + c_1 \phi$.

Discussion of Sample Calculations

Steady-state component.- Table X, which shows the calculation for this condition, is very similar to that given in reference 1. Column (5) is calculated in the same manner as in reference 1. The equation for finding the aerodynamic loading for the rigid blade is given in appendix D of this report. Likewise, column (7) is computed as in reference 1.

Notice that y_{III} must be neglected in the calculation of τ_I since y_{III} is not known at this stage of the computation. It was found that after completing a cycle (i.e., sine and cosine components), the effect of y_{III} on τ_I was small. Therefore the result obtained from table X was taken as the steady-state bending-moment distribution.

The computation check (table XI) for this calculation is identical to that given in reference 1, and is the same for the first-harmonic components.

First-harmonic components.- Table XII shows the calculation of a, b, and c. It should be noted that only a changes with the aerodynamic shear, b and c remaining the same for given blade constants and rotational speed.

The first-harmonic sine component was first calculated by using the expression for τ_{II} given in appendix D neglecting y_{III} since it was not known at this stage of the calculation. The computation check yields in addition the deflection y_{II}.

Having y_I and y_{II}, it is then possible to calculate τ_{III} and the corresponding aerodynamic shear. A calculation of the a's according to table XII(a) permits the computation of the cosine component of bending moment and consequently y_{III} in the computation check.

The sine component of the aerodynamic loading τ_{III} is then recalculated using y_{III} just obtained. For this example it was found that y_{III} had a considerable effect upon τ_{II} and consequently on the bending moment. The iteration process is continued to find a new y_{II}: To decrease the number of cycles in the iteration process the mean value of y_{II} resulting from the first and second cycles is found. This value of y_{II} is then used in the second-cycle calculation of τ_{III}. The resulting cosine bending moment and consequently the distribution of y_{III} are then found. This makes it possible to recalculate the sine component and find y_{II} which is compared with the mean value assumed above. In this example the two values of y_{II} were within 10 percent so that iteration was not continued.

A plot of the bending-moment distributions during the above process for the blade under test is shown in figure 25. It should be stressed that only the a's need be recalculated in carrying out the iteration since b and c do not change with aerodynamic loading.

It has recently come to the attention of the author that the Cornell Aeronautical Laboratory has extended the Goodyear tabular-dynamic method to take into account the additional aerodynamic loading introduced by the elastic deformation of a hinged rotor blade. This additional effect is considered immediately in the moment equation and the sine and cosine components are carried along simultaneously so that no iteration is necessary. The application of this method, with the appropriate modifications, to the fixed-at-root blade has not been studied in detail, but it appears that such an application is possible. For the present case, where no possibility of resonance with the assumed loadings existed, the iteration process appears to be a reasonably rapid and accurate method of estimating the bending-moment distribution on a semirigid nonflapping blade.

REFERENCES

1. Johnson, W. C., and Mayne, R.: Stress Analysis of Rotor Blades by a Tabular-Dynamic Method. Rep. No. R-107-4, pt. II A, GER-264, Goodyear Aircraft Corp., April 24, 1946.

2. Knight, Montgomery, and Hefner, Ralph A.: Static Thrust Analysis of the Lifting Airscrew. NACA TN 626, 1937.

3. De Guillenchmidt, P.: Calculation of the Bending Stresses in Helicopter Rotor Blades. NACA TM 1312, 1951.

4. Morduchow, Morris: A Theoretical Analysis of Elastic Vibrations of Fixed-Ended and Hinged Helicopter Blades in Hovering and Vertical Flight. NACA TN 1999, 1950.

5. Myklestad, N. O.: Vibration Analysis. First ed., McGraw-Hill Book Co., Inc., 1944.

TABLE I

VALUES OF AERODYNAMIC LOADING F_A' (LB/FT)

AT EIGHT AZIMUTH POSITIONS

[Calculation of F_A' may be set up the same way as that given in reference 1.]

Station	$\psi = 0^\circ$	$\psi = 45^\circ$	$\psi = 90^\circ$	$\psi = 135^\circ$	$\psi = 180^\circ$	$\psi = 225^\circ$	$\psi = 270^\circ$	$\psi = 315^\circ$
0	0.098	-0.136	0.182	-0.014	0.270	0.504	0.550	0.382
1	.138	.313	.496	.581	.516	.341	.160	.073
2	.850	1.27	1.57	1.58	1.29	.870	.571	.560
3	2.25	2.66	2.93	2.91	2.61	2.20	1.93	1.95
4	4.34	4.52	4.63	4.60	4.46	4.28	4.17	4.20
5	7.11	6.85	6.66	6.66	6.85	7.11	7.29	7.30
6								

TABLE II

CALCULATION OF CENTRIFUGAL LOADING F_c' (LB/FT)

AT EIGHT AZIMUTH POSITIONS

$[F_c' = F_c\beta]$

Station	F_c (lb/ft)	$\psi = 0^\circ$ $\beta = 0.0007$	$\psi = 45^\circ$ $\beta = 0.0056$	$\psi = 90^\circ$ $\beta = 0.0444$	$\psi = 135^\circ$ $\beta = 0.0930$	$\psi = 180^\circ$ $\beta = 0.123$	$\psi = 225^\circ$ $\beta = 0.117$	$\psi = 270^\circ$ $\beta = 0.0778$	$\psi = 315^\circ$ $\beta = 0.0293$
0	8.87	-0.0062	0.0497	0.394	0.825	1.09	1.03	0.690	0.259
1	26.6	-.0186	.149	1.18	2.47	3.27	3.10	2.07	.777
2	44.2	-.0309	.248	1.96	4.11	5.43	5.15	3.44	1.29
3	62.0	-.0434	.347	2.75	5.77	7.62	7.23	4.82	1.81
4	79.7	-.0558	.446	3.54	7.41	9.80	9.29	6.20	2.33
5	97.5	-.0683	.546	4.33	9.07	11.9	11.4	7.59	2.85
6									

TABLE III

CALCULATION OF TOTAL EXTERNAL LOADING F_d' (LB/FT) AT

EIGHT AZIMUTH POSITIONS

$$\left[F_d' = F_A' - F_c'\right]$$

Station	$\psi = 0^\circ$	$\psi = 45^\circ$	$\psi = 90^\circ$	$\psi = 135^\circ$	$\psi = 180^\circ$	$\psi = 225^\circ$	$\psi = 270^\circ$	$\psi = 315^\circ$
0								
	0.104	-0.186	-0.212	-0.811	-0.820	-0.530	-0.140	0.123
1								
	.157	.163	-.685	-1.89	-2.75	-2.76	-1.91	-.704
2								
	.881	1.02	-.392	-2.53	-4.14	-4.28	-2.87	-.731
3								
	2.29	2.31	.177	-2.86	-5.01	-5.03	-2.89	.140
4								
	4.40	4.07	1.09	-2.81	-5.35	-5.01	-2.03	1.87
5								
	7.18	6.30	2.33	-2.41	-5.13	-4.26	-.296	4.45
6								

NACA

TABLE IV

CALCULATION OF $\int_0^R F_d'\eta_1\,dx$ AT EIGHT AZIMUTH POSITIONS

Station	η_1	$\psi = 0^\circ$		$\psi = 45^\circ$		$\psi = 90^\circ$		$\psi = 135^\circ$	
		$F_d'\eta_1$	$F_d'\eta_1 \times 5''$	$F_d'\eta_1$	$F_d'\eta_1 \times 5''$	$F_d'\eta_1$	$F_d'\eta_1 \times 5''$	$F_d'\eta_1$	$F_d'\eta_1 \times 5''$
0									
1	-0.210	-0.022	-0.110	0.0391	0.196	0.0445	0.223	0.170	0.85
2	-.560	-.088	-.440	-.0913	-.457	.384	1.920	1.06	5.30
3	-.680	-.599	-2.99	-.694	-3.47	.266	1.33	1.72	8.60
4	-.462	-1.058	-5.29	-1.067	-5.34	-.082	-.41	1.32	6.60
5	.010	.044	.220	.041	.205	.011	.055	-.028	-.140
6	.610	4.379	21.91	3.84	19.20	1.42	7.10	-1.47	-7.35
		$\int_0^R F_d'\eta_1\,dx = \Sigma = 13.30$		$\Sigma = 10.35$		$\Sigma = 10.24$		$\Sigma = 13.87$	

Station	η_1	$\psi = 180^\circ$		$\psi = 225^\circ$		$\psi = 270^\circ$		$\psi = 315^\circ$	
		$F_d'\eta_1$	$F_d'\eta_1 \times 5''$	$F_d'\eta_1$	$F_d'\eta_1 \times 5''$	$F_d'\eta_1$	$F_d'\eta_1 \times 5''$	$F_d'\eta_1$	$F_d'\eta_1 \times 5''$
0									
1	-0.210	0.172	0.860	0.111	0.555	0.029	0.145	-0.026	-0.130
2	-.560	1.54	7.70	1.55	7.75	1.07	5.35	.394	1.970
3	-.680	2.82	14.10	2.91	14.55	1.95	9.75	.497	2.49
4	-.462	2.32	11.60	2.32	11.60	1.33	6.65	-.065	-.325
5	.010	-.054	-.270	-.051	-.255	-.020	-.100	.018	.090
6	.610	-3.13	-15.65	-2.59	-12.95	-.181	-.905	2.72	13.60
			$\Sigma = 18.26$		$\Sigma = 21.25$		$\Sigma = 20.93$		$\Sigma = 17.68$

NACA

TABLE V

CALCULATION OF $\int_0^R m'\eta_1^2\,dx$

Station	η_1	η_1^2	m' (slugs/ft)	$m'\eta_1^2 \times 5/12$
0				
	-0.210	0.0441	0.00602	0.111×10^{-3}
1				
	-.560	.3136	.00602	.787
2				
	-.680	.4624	.00602	1.16
3				
	-.462	.2134	.00602	.536
4				
	.010	.0001	.00602	.00025
5				
	.610	.3721	.00602	.934
6				
			$\int_0^R m'\eta_1^2\,dx = 3.528 \times 10^{-3}$	

TABLE VI

CALCULATIONS OF g_1 AT EIGHT AZIMUTH POSITIONS

ψ (deg)	$\int F_d'\eta_1 \, dx$	$g_1 = \dfrac{\int_0^R F_d'\eta_1 \, dx}{\int_0^R m'\eta_1^2 \, dx}$
0	13.30	3769
45	10.35	2935
90	10.24	2901
135	13.87	3932
180	18.26	5177
225	21.25	6024
270	20.93	5929
315	17.68	5014

NACA

TABLE VII

CALCULATION OF $g_{1,n}\begin{Bmatrix}a\\b\end{Bmatrix} \times A_{i,n}$ AND M_1

$\left[\nu_{1,0} = 55 \text{ cps};\ \nu_{1,\omega} = 62.5 \text{ cps};\ \omega = 800 \text{ rpm};\ \omega^2 = 7029.1(\text{radians/sec})^2\right]$

(1)	(2)	(3)	(4)	(5)	(6)	(7)	(8)
n	$g_{1,na}$	$g_{1,nb}$	$n^2\omega^2$	$(\nu_{1,\omega})^2 - (4)$	$\frac{(\nu_{1,0})^2}{(5)}$	$g_{1,na} \times (6)$	$g_{1,nb} \times (6)$
0	4500	-----	0	154,056	0.775	3490	-----
1	-720	-1560	7029.1	147,027	.812	-586.0	-1265
2	0	0	------	-------	-----	0	0
3	0	0	------	-------	-----	0	0

(1)	(2)	(3)	(4)	(5)
i	$\iint m'\eta_1\, dx\, d\xi$	Steady state $M_{1,0} = (7)_{n=0} \times (2)$	First cosine $M_{1,a} = (7)_{n=1} \times (2)$	First sine $M_{1,b} = (8)_{n=1} \times (2)$
0	0	0	0	0
1	$.6666 \times 10^{-3}$	2.33	-.391	-.843
2	1.27516	4.45	-.75	-1.61
3	1.70116	5.94	-.998	-2.15
4	1.89016	6.60	-1.107	-2.39
5	1.82659	6.37	-1.07	-2.31
6	1.53819	5.37	-.90	-1.94
7	1.0946	3.82	-.64	-1.38
8	.60099	2.10	-.35	-.76
9	.1878	.66	-.11	-.24
10	0	0	0	0

TABLE VIII

CALCULATION OF $g_{2,n} \begin{Bmatrix} a \\ b \end{Bmatrix} \times A_{2,n}$ AND M_2

$\left[\nu_{2,0} = 169 \text{ cps};\ \nu_{2,\omega} = 178.5 \text{ cps};\ \omega = 800 \text{ rpm};\ \omega^2 = 7029.1\right]$

(1)	(2)	(3)	(4)	(5)	(6)	(7)	(8)
n	$g_{2,na}$	$g_{2,nb}$	$n^2\omega^2$	$(\nu_{2,\omega})^2 - (4)$	$\frac{(\nu_{2,0})^2}{(5)}$	$g_{2,na} \times (6)$	$g_{2,nb} \times (6)$
0	90	----	0	1,257,396.7	0.8967	80.7	------
1	-947	-747	7029.1	1,250,367.6	.90177	-853.9	-673.6
2	0	0	------	----------	-------	0	0
3	0	0	------	----------	-------	0	0

(1)	(2)	(3)	(4)	(5)
i	$\iint m'\eta_2\, dx\, d\xi$	Steady state $M_{2,0} = (7)_{n=0} \times (2)$	First cosine $M_{2,a} = (7)_{n=1} \times (2)$	First sine $M_{2,b} = (8)_{n=1} \times (2)$
0	0	0	0	0
1	$-.3818 \times 10^{-3}$	-.0308	.326	.257
2	-.4832	-.0389	.413	.325
3	-.5107	-.0412	.436	.344
4	-.1957	-.0158	.167	.132
5	.2166	.0175	-.185	-.146
6	.5384	.0435	-.459	-.363
7	.6315	.0509	-.539	-.425
8	.4743	.0383	-.405	-.319
9	.1878	.0152	-.160	-.126
10	0	0	0	0

TABLE IX

SUMMARY OF BENDING-MOMENT DISTRIBUTIONS

(INCLUDES FIRST AND SECOND NATURAL MODES)

i	M_0 (steady state)	M_a (cosine) (in.-lb)	M_b (sine) (in.-lb)	M_{max} $\psi = 225^\circ$ (in.-lb)
0	0	0	0	0
1	2.30	-.06	-.58	2.75
2	4.41	-.34	-1.28	5.55
3	5.90	-.56	-1.81	7.58
4	6.58	-.94	-2.26	8.84
5	6.39	-1.26	-2.45	9.01
6	5.41	-1.36	-2.30	8.00
7	3.87	-1.18	-1.81	5.98
8	2.14	-.76	-1.08	3.44
9	.68	-.27	-.37	1.13
10	0	0	0	0

NACA

TABLE X

CALCULATION OF STEADY-STATE COMPONENT OF BENDING MOMENT

FOR A ROTOR BLADE FIXED AT ROOT

[μ = 0.47; Ω = 600 rpm; m_i = 0.00602 slug/ft; $\beta = 0^\circ$; $\theta_0 = 8^\circ$; $\alpha = -5^\circ$; X = 5 in.; EI = 16,000 lb-in.^{2}; z_{III} terms neglected, ( )* indicates value from the preceding station (i)]

i	(1) a_i (1)* + (6)* + (7)*	(2) $\frac{X^2}{EI_i}$	(3) $\frac{X^2 a_i}{EI}$	(4) $\sum_{j=1}^{i} \frac{X^2 a_j}{EI_j}$	(5) $F_{i+\frac{1}{2}}$	(6) $F_{i+\frac{1}{2}} \sum_{j=1}^{i} \frac{X^2 a_j}{EI_j}$	(7) $XS_{i+\frac{1}{2}}$
0	0	1.563×10^{-3}	0	0	73.80	0	-15.22
1	-15.22000	1.563	-.0237886	-.0237886	69.67	-1.65736988	-15.10
2	-31.97736	1.563	-.0499806	-.0737692	61.41	-4.53016836	-14.56
3	-51.06753	1.563	-.0798185	-.1535877	49.02	-7.5288735	-13.00
4	-71.59641	1.563	-.1119052	-.2654929	32.50	-8.628522	-9.60
5	-89.92493	1.563	-.1405526	-.4060456	11.85	-4.81164094	-3.70
6	-98.43657	1.563	---------	---------	-----	----------	------

i	(8) b_i (8)* + (11)*	(9) $\frac{X^2 b_i}{EI_i}$	(10) $\sum_{j=0}^{i} \frac{X^2 b_j}{EI_j}$	(11) $F_{i+\frac{1}{2}}(10)$	(12) $b_i Z$	(13) M_i $a_i + b_i Z$
0	1	0.0015630	0.0015630	0.1153494	37.61965	37.61965
1	1.1153494	.0017432	.0033062	.2303493	41.95906	26.73906
2	1.3456987	.0021033	.0054096	.3322045	50.62472	18.64735
3	1.6779033	.0026225	.0080321	.3937376	63.12214	12.05467
4	2.0716409	.0032379	.0112701	.3662801	77.93441	6.33800
5	2.4379210	.0038104	.0150806	.1787054	91.71374	1.78881
6	2.6166264	---------	---------	---------	98.43657	0

$$Z = -\frac{a_6}{b_6} = -\frac{-98.436573}{2.616626} = 37.619651$$

TABLE XI

COMPUTATION CHECK FOR STEADY-STATE COMPONENT OF BENDING MOMENT

FOR A ROTOR BLADE FIXED AT ROOT

[μ = 0.47; Ω = 600 rpm; m_i = 0.00602 slug/ft; $\beta = 0^\circ$; $\theta_0 = 8^\circ$; $\alpha = -5^\circ$; X = 5 in.; EI = 16,000 lb-in.^{2}; z_{III} terms neglected]

i	(13) M_i $a_i + b_iZ$	(14) ΔM	(15) $\frac{X^2}{EI_i}$	(16) $\frac{X^2}{EI_i} M_i$	(17) $X\left(\frac{dy}{dr}\right)_{i+\frac{1}{2}} = \sum(16)$
0	37.61965		1.563×10^{-3}	0.0587995	0.0587995
		-10.88059			
1	26.73906		1.563	.0417932	.1005927
		-8.09171			
2	18.64735		1.563	.0291458	.129739
		-6.59275			
3	12.05467		1.563	.0188413	.148580
		-5.71667			
4	6.33800		1.563	.0099063	.158486
		-4.54919			
5	1.78881		1.563	.0027959	.161282
		-1.78881			
6	0		1.563	0	---------

i	(18) $F_{i+\frac{1}{2}}$	(19) $F_{i+\frac{1}{2}} X\left(\frac{dy}{dr}\right)_{i+\frac{1}{2}}$	(20) $XS_{i+\frac{1}{2}}$	(21) ΔM (19) + (20)	(22) $y_I = \sum_{j=0}^{i-1} (17)_j$
0	73.80	4.339991	-15.22	-10.88097	0
1	69.67	7.008293	-15.10	-8.09171	.0587995
2	61.41	7.967272	-14.56	-6.59273	.1593922
3	49.02	7.283391	-13.00	-5.71661	.2891312
4	32.50	5.150795	-9.60	-4.4492	.4377112
5	11.85	1.911192	-3.70	-1.78881	.5961972
6	-----		------		.7574792

TABLE XII

GOODYEAR METHOD (MODIFIED) FOR CALCULATING FIRST-HARMONIC SINE COMPONENT

OF BENDING MOMENT FOR A ROTOR BLADE FIXED AT ROOT

[μ = 0.47; Ω = 600 rpm; m_1 = 0.00602 slug/ft; β = 0°; θ_0 = 8°; α = -5°; X = 5 in.; EI = 16,000 lb-in.^{2}; ( )* indicates value from preceding station (i)]

(a) Calculation of a.

i	(1) a_i (1)* + (6)* + (7)* + (11)*	(2) $\frac{X^2}{EI}$	(3) $\frac{X^2 a_i}{EI}$	(4) $\Sigma_a = \sum_{j=1}^{i} \frac{X^2 a_j}{EI}$	(5) $F_{i+\frac{1}{2}}$	(6) $F_{i+\frac{1}{2}} \Sigma_a$	(7) $XB_{i+\frac{1}{2}}$	(8) U_i (4)* + (8)*	(9) $X^2\Omega^2 m_i$	(10) $X^2\Omega^2 m_i U_i$	(11) $\sum_{j=1}^{i} (10)_j$ (10) + (11)*
0	0	1.563×10^{-3}	0	0	73.80	0	-25.01	0	4.13	0	0
1	-25.01	1.563	-.0390906	-.0390906	69.67	-2.7234421	-25.00	0	4.13	0	0
2	-52.7334421	1.563	-.0824224	-.1215129	61.41	-7.4621115	-22.97	-.0390906	4.13	-.1614442	-.1614442
3	-83.3269978	1.563	-.1302401	-.2517530	49.02	-12.3409355	-18.85	-.1606036	4.13	-.6632929	-.8247371
4	-115.3426704	1.563	-.1802806	-.4320336	32.50	-14.0410940	-12.75	-.4123567	4.13	-1.7030332	-2.5277703
5	-144.6615347	1.563	-.2261060	-.6581396	11.85	-7.7989542	-4.55	-.8443904	4.13	-3.4873324	-6.0151027
6	-163.0253917	1.563	-.2548090	-.9129486	0	0	------	-1.5025530	4.13	-6.2054489	-12.2205516

(b) Calculation of b.

i	(12) b_i (12)* + (15)* + (18)*	(13) $\frac{X^2 b_i}{EI}$	(14) $\Sigma_b = \sum \frac{X^2 b_j}{EI}$	(15) $F_{i+\frac{1}{2}} \Sigma_b$	(16) V_i (14) + (16)	(17) $X^2\Omega^2 m_i V_i$	(18) $\sum_{j=1}^{i} (17)_j$ (17) + (18)*
0	1.0	0.001563	0.001563	0.1153494	0	0	0
1	1.1153494	.001743	.003306	.2303499	.001563	.0064552	.0064552
2	1.3521545	.002113	.005419	.3328250	.004869	.0201102	.0265654
3	1.7115449	.002675	.008094	.3968100	.010289	.0424937	.0690591
4	2.1774140	.003403	.011498	.3736902	.018383	.0759254	.1449845
5	2.6960887	.004213	.015712	.1861889	.029882	.1234128	.2683973
6	3.1506750	.004924	.020636	0	.045594	.1883040	.4567013

TABLE XII - Concluded

GOODYEAR METHOD (MODIFIED) FOR CALCULATING FIRST-HARMONIC SINE COMPONENT

OF BENDING MOMENT FOR A ROTOR BLADE FIXED AT ROOT

(c) Calculation of c.

i	(19)	(20)	(21)	(22)	(23)	(24)	(25)
	c_i 1.0 + (19)* + (22)* + (25)*	$\frac{X^2 c_i}{EI}$	$\Sigma_c = \sum_{j=1}^{i} \frac{X^2 c_i}{EI}$	$F_{i+\frac{1}{2}} \Sigma_c$	W_i (21)* + (23)*	$X^2 \Omega^2 m_i W_i$	$\sum_{i=1}^{i} (24)_j$ (24) + (25)*
0	0	0	0	0	0	0	0
1	1.0	.001563	.001563	.10889421	0	0	0
2	2.10889421	.003296	.004859	.29840347	.001563	.0064552	.0064552
3	3.41375288	.005335	.010194	.49975380	.006422	.0265236	.0329788
4	4.94648557	.007731	.017926	.58260313	.016617	.0686286	.1016075
5	6.63069620	.010363	.028290	.33523686	.034543	.1426640	.2442715
6	8.21020460	.012832	.041122	0	.062833	.2595018	.5037734

(d) Calculation of M.

i	(26)	(27)	(28)
	$b_i M_0$	$c_i \phi$	M_i (1) + (26) + (27)
0	147.5	0	147.5
1	164.514	-36.8	102.704
2	199.443	-77.6072	69.102
3	252.453	-125.6261	43.499
4	321.168	-182.0306	23.794
5	397.672	-244.0096	9.001
6	464.725	-302.1355	0

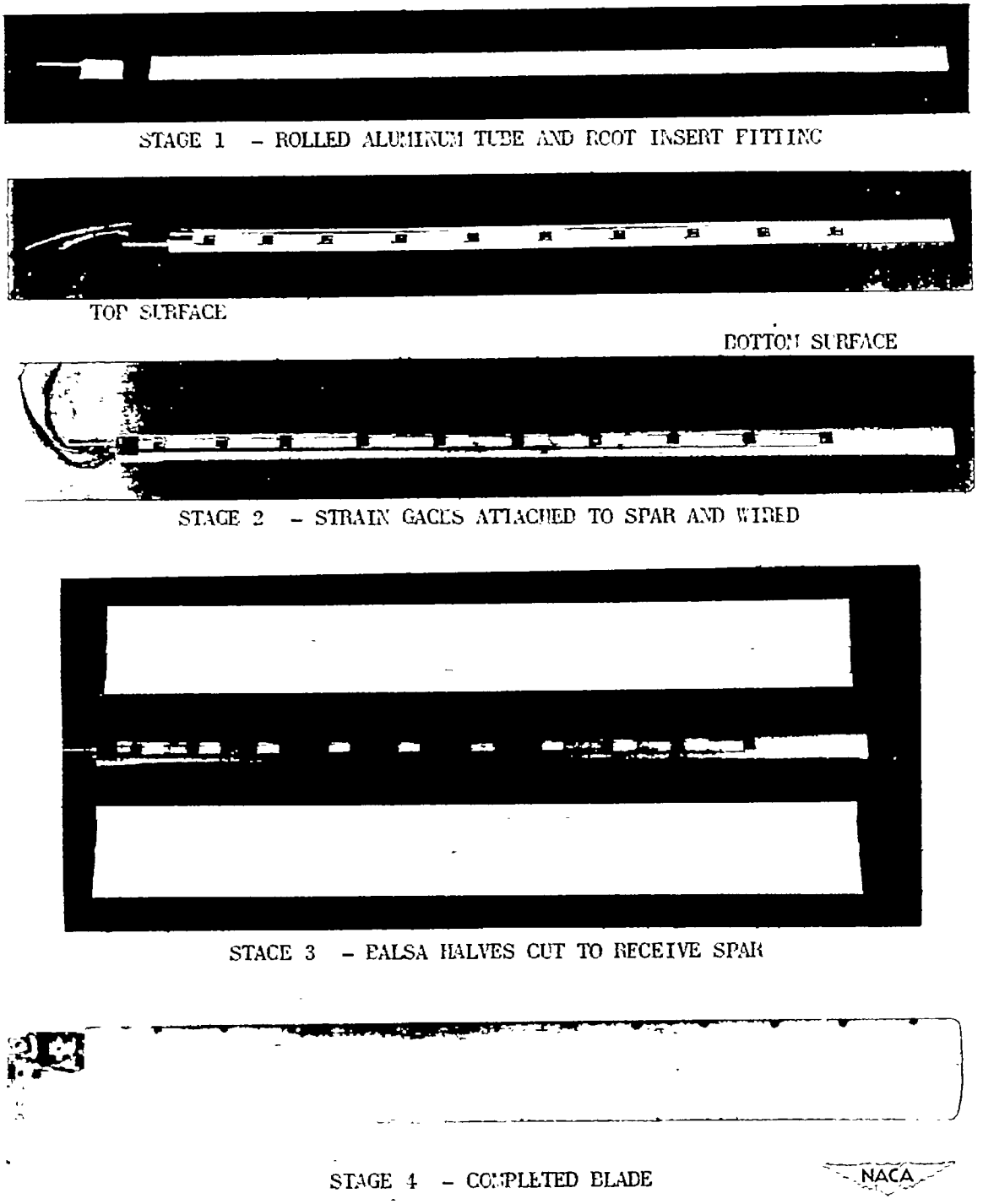

Figure 1.- Blade construction details.

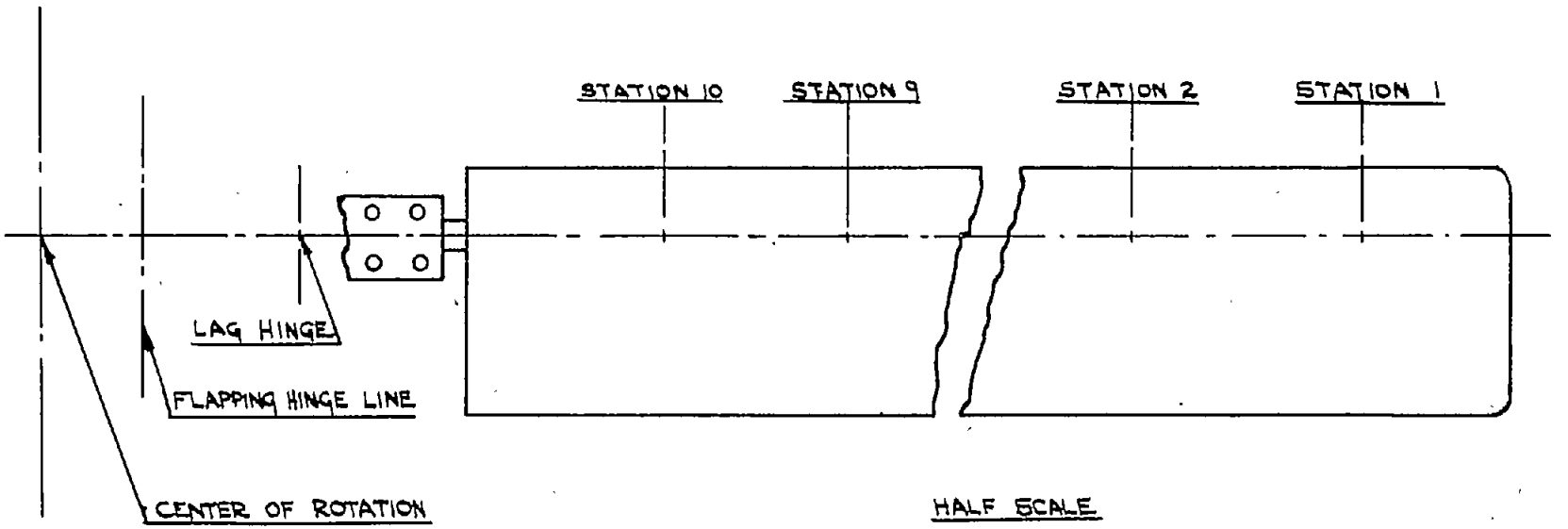

STATION	r (IN.)	$\frac{r}{R}$	STATION	r (IN.)	$\frac{r}{R}$
1	28 3/8	0.945	6	15 7/8	0.529
2	25 7/8	.863	7	13 3/8	.445
3	23 3/8	.778	8	10 7/8	.363
4	20 7/8	.695	9	8 7/8	.296
5	18 3/8	.613	10	6 7/8	.229

Figure 2.- Strain-gage locations on rotor blade.

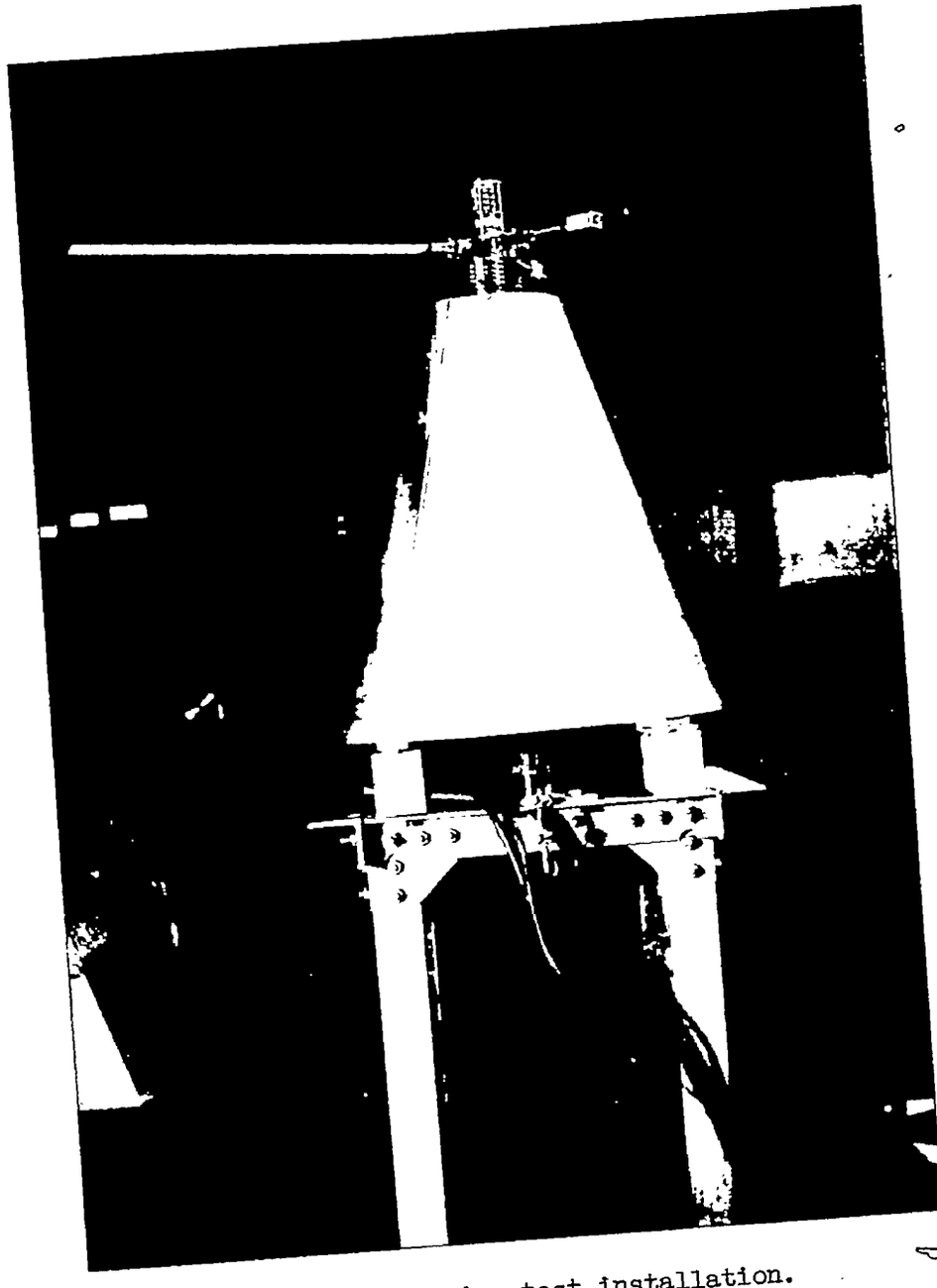

Figure 3.- Hovering test installation.

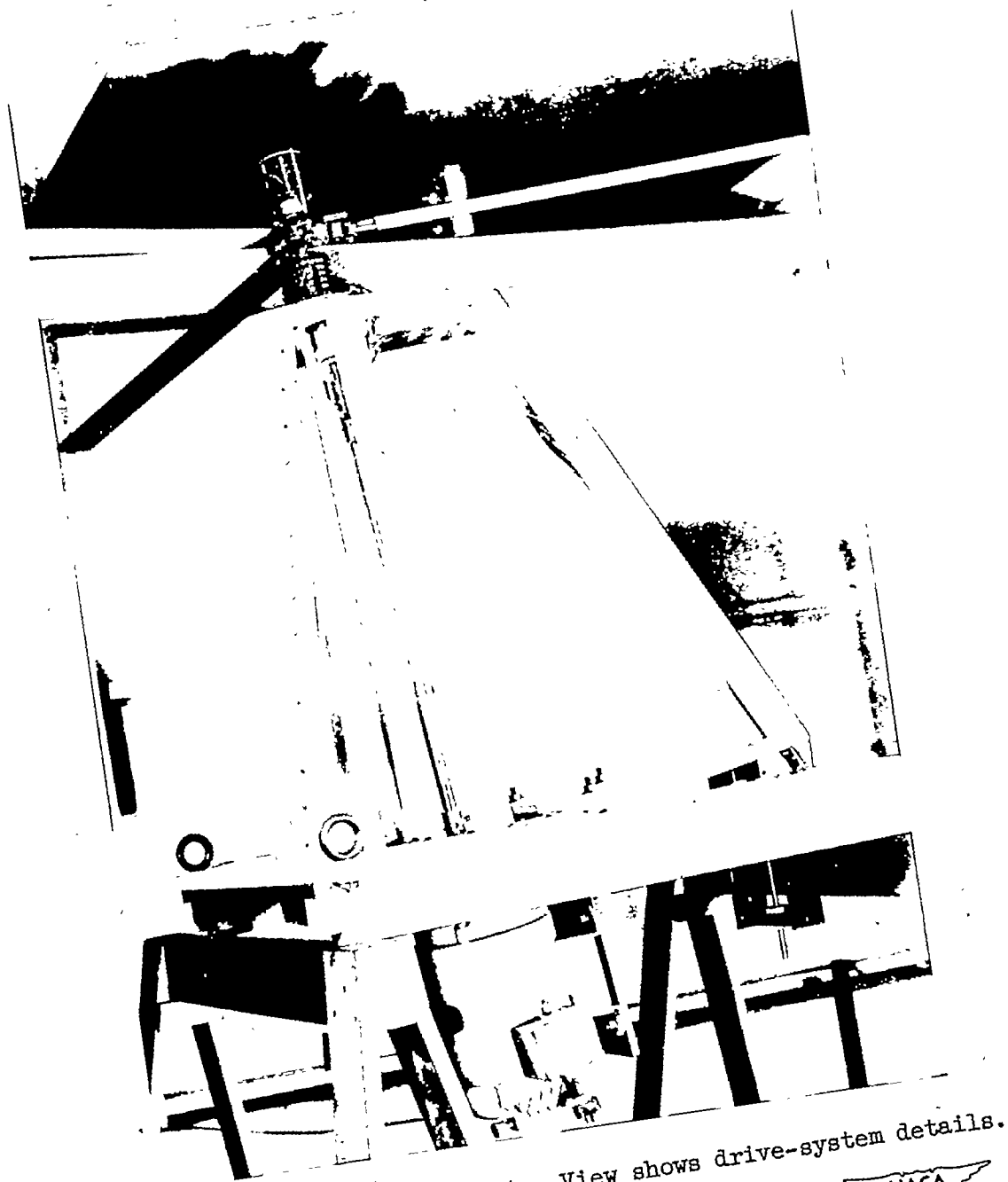

Figure 4.- Wind-tunnel mount. View shows drive-system details.

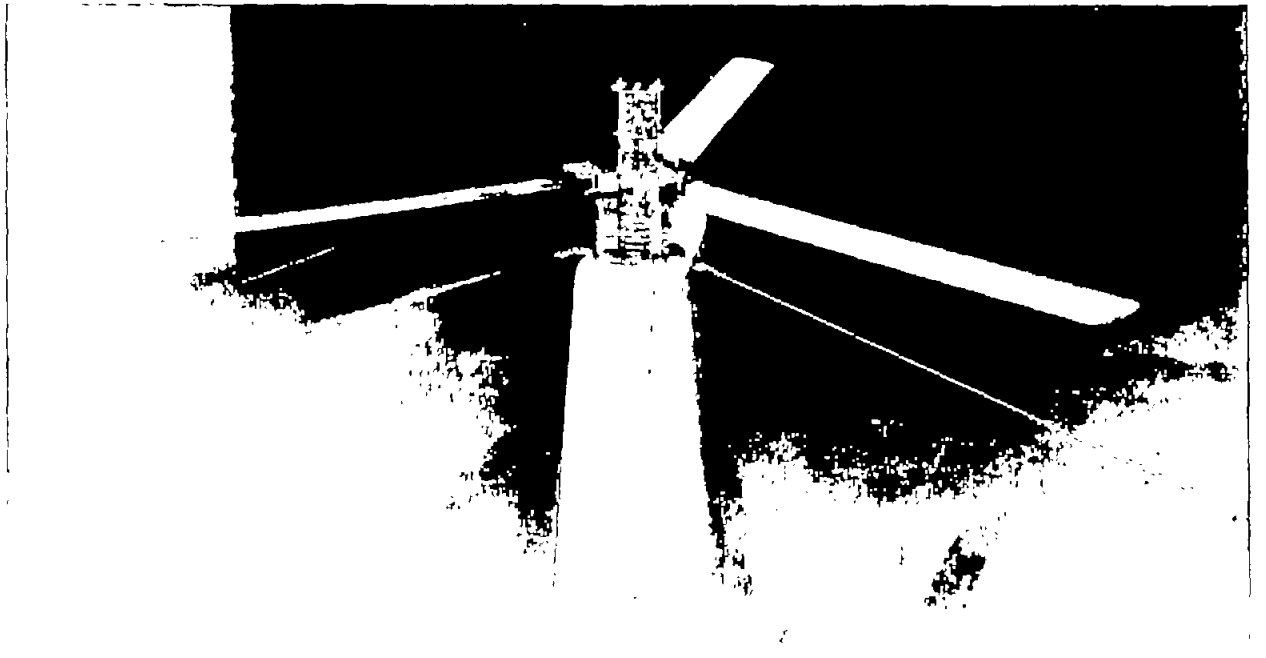

Figure 5.- Wind-tunnel installation, looking downstream.

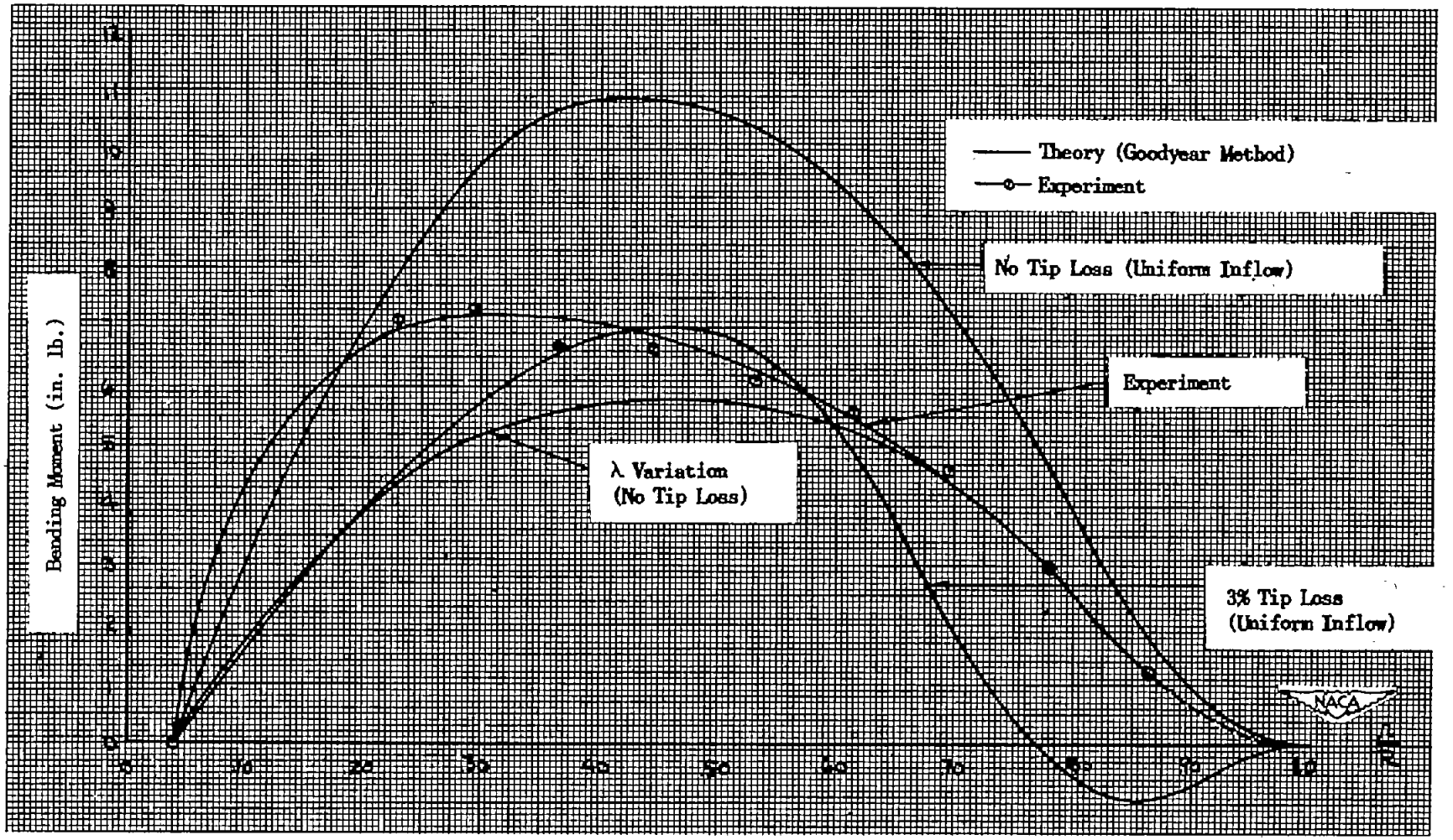

(a) Hovering, hinged-at-root condition; rotor speed, 1400 rpm.

Figure 6.- Comparison of theoretical and experimental bending-moment distributions. $\theta = 8^{\circ}$; $\lambda = -0.054$; EI = 16,000 pound-inches^2.

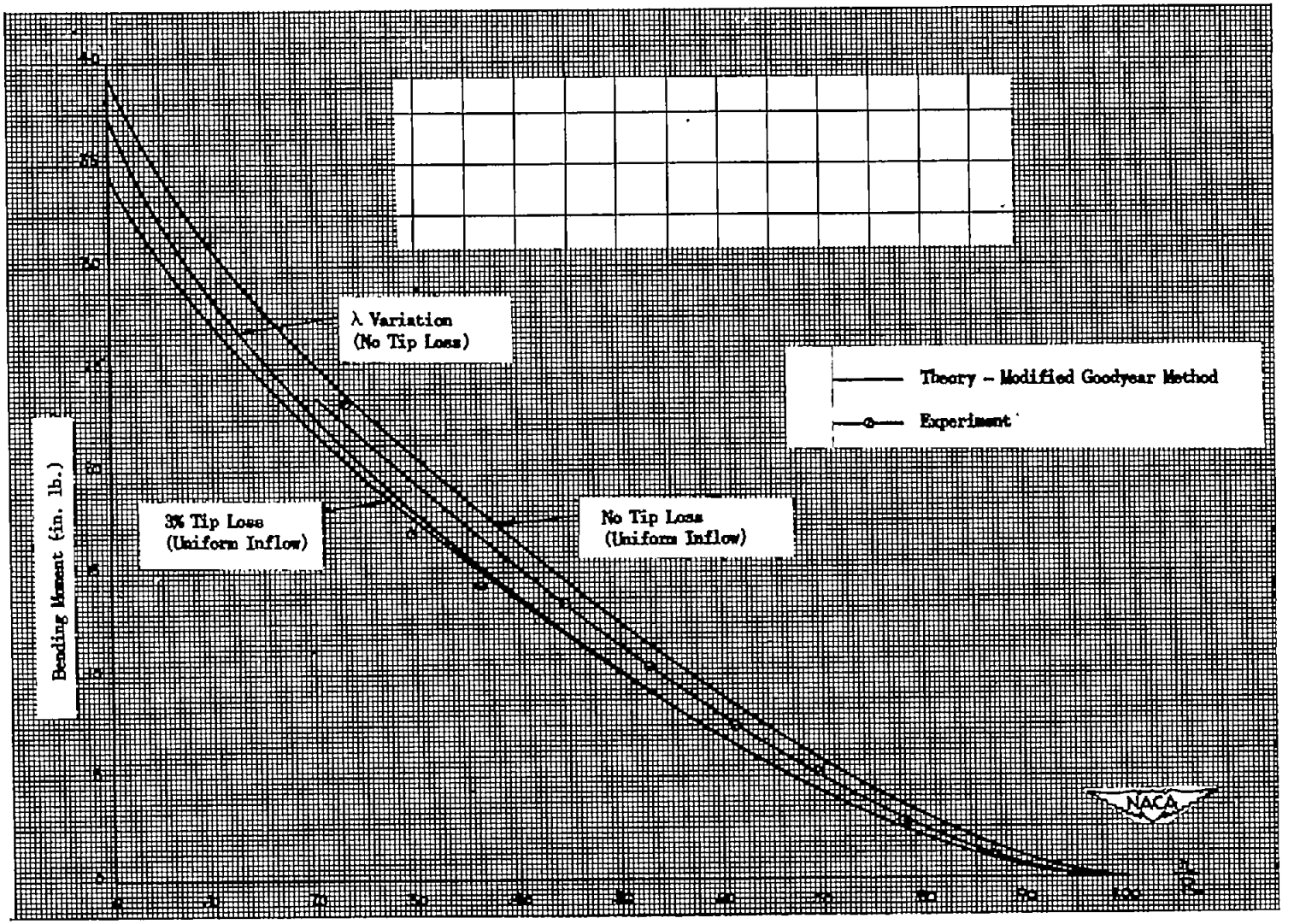

(b) Hovering, fixed-at-root condition; $\beta_0 = 0^{\circ}$; rotor speed, 800 rpm.

Figure 6.- Concluded.

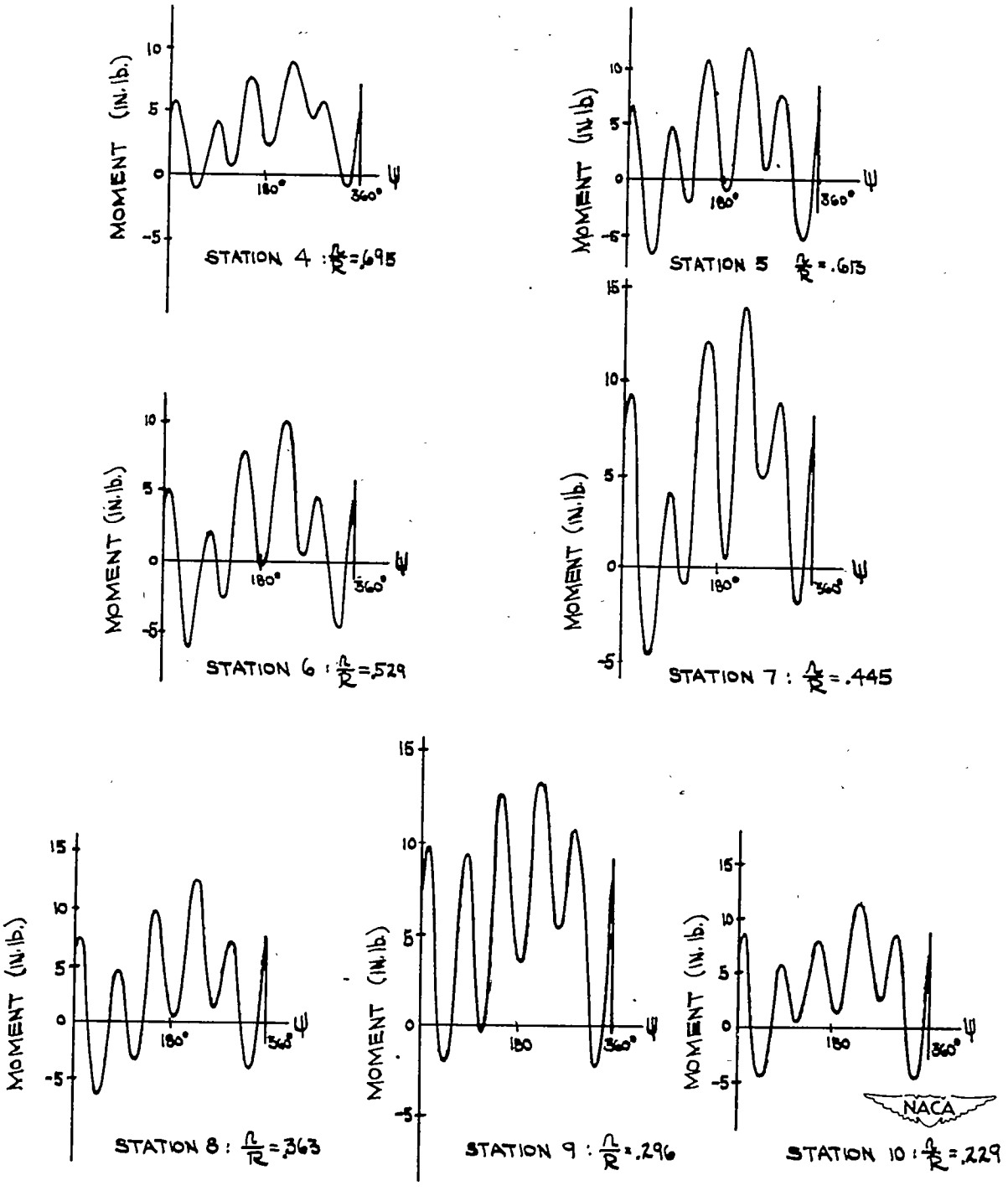

(a) $\mu = 0.10$.

Figure 7.- Bending-moment traces from oscillograph records. Hinged-at-root condition; $\theta_0 = 8^\circ$; $\alpha = -5^\circ$; rotor speed, 800 rpm.

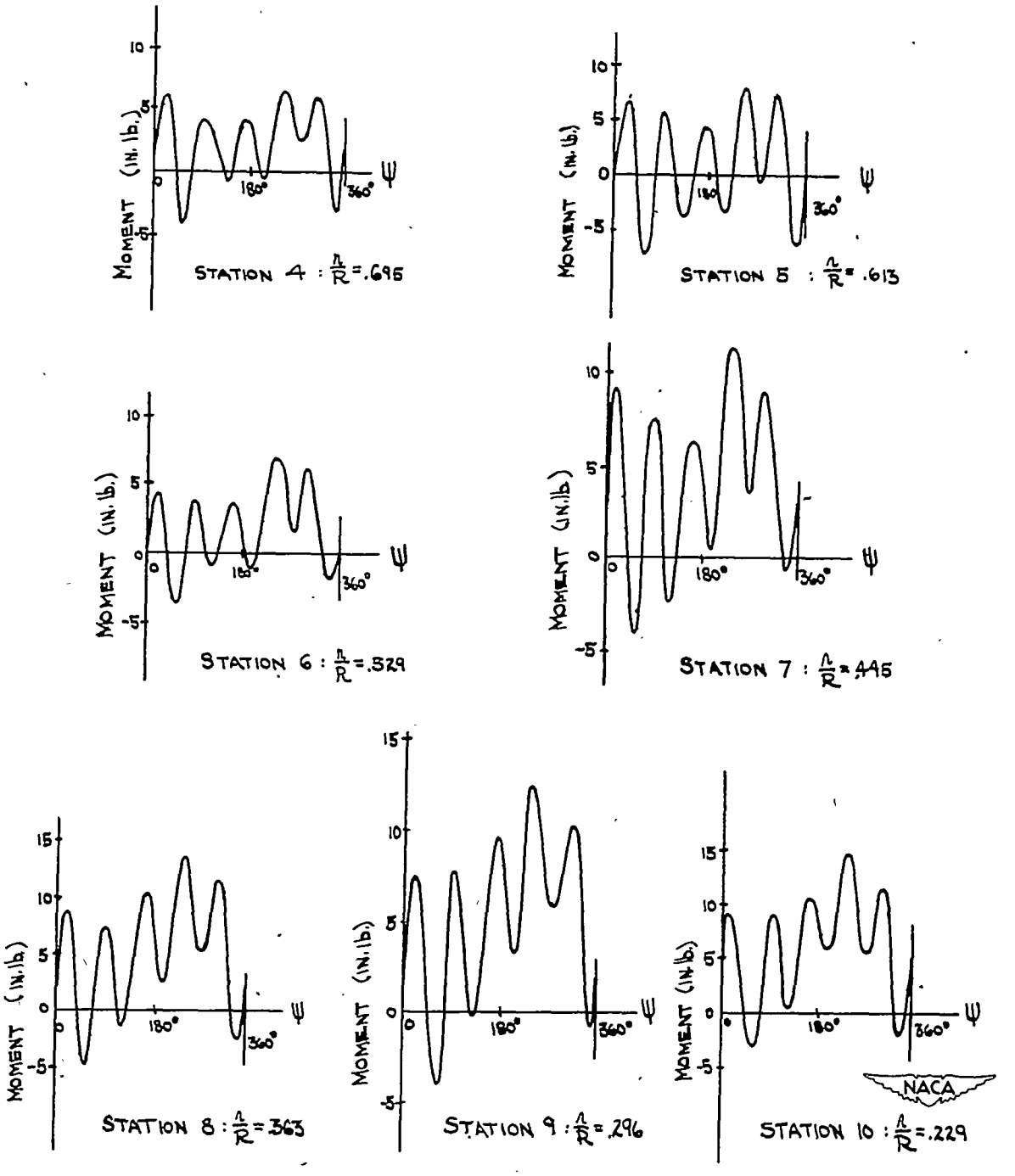

(b) $\mu = 0.22$.

Figure 7.- Continued

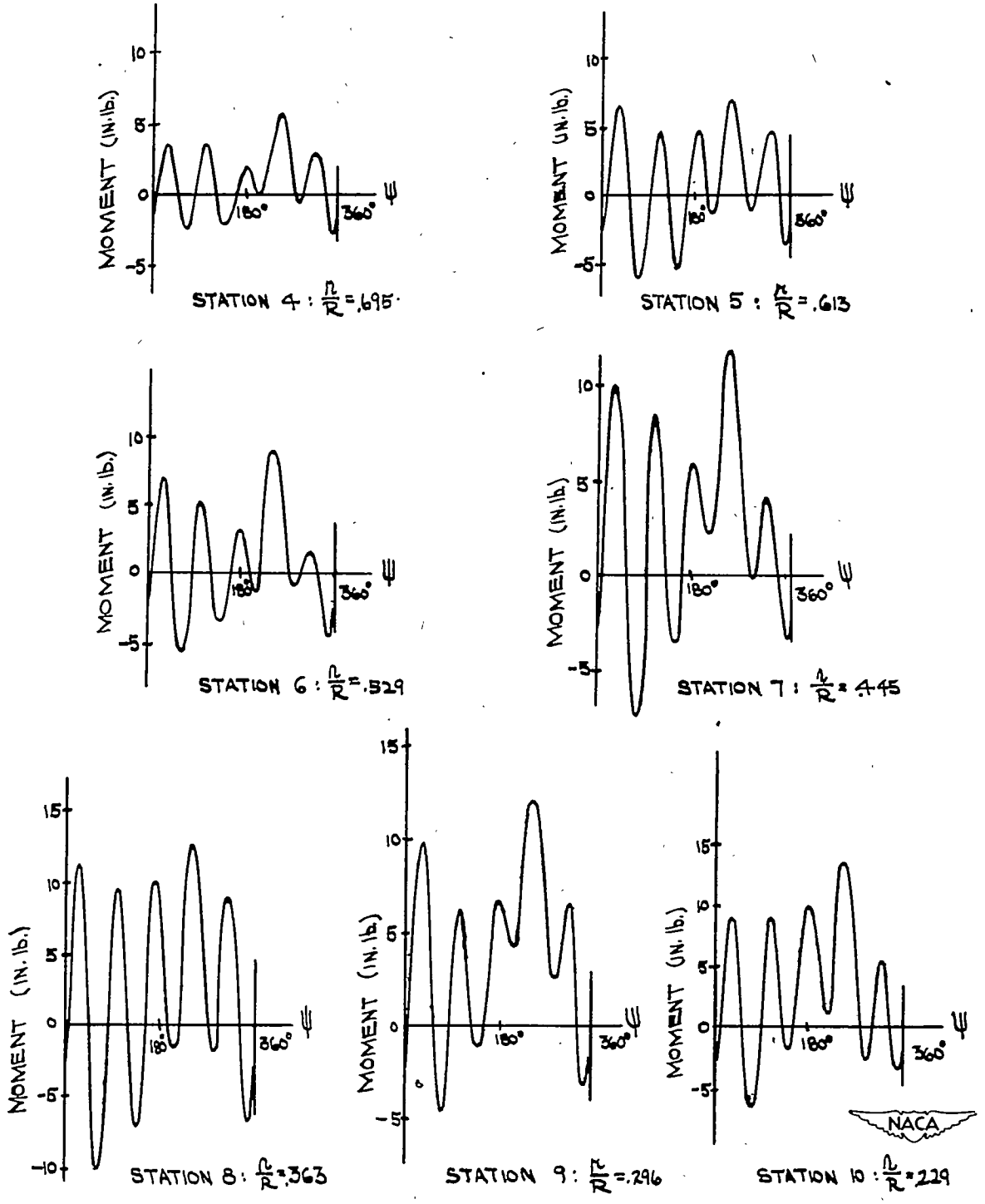

(c) $\mu = 0.30$.

Figure 7.- Continued.

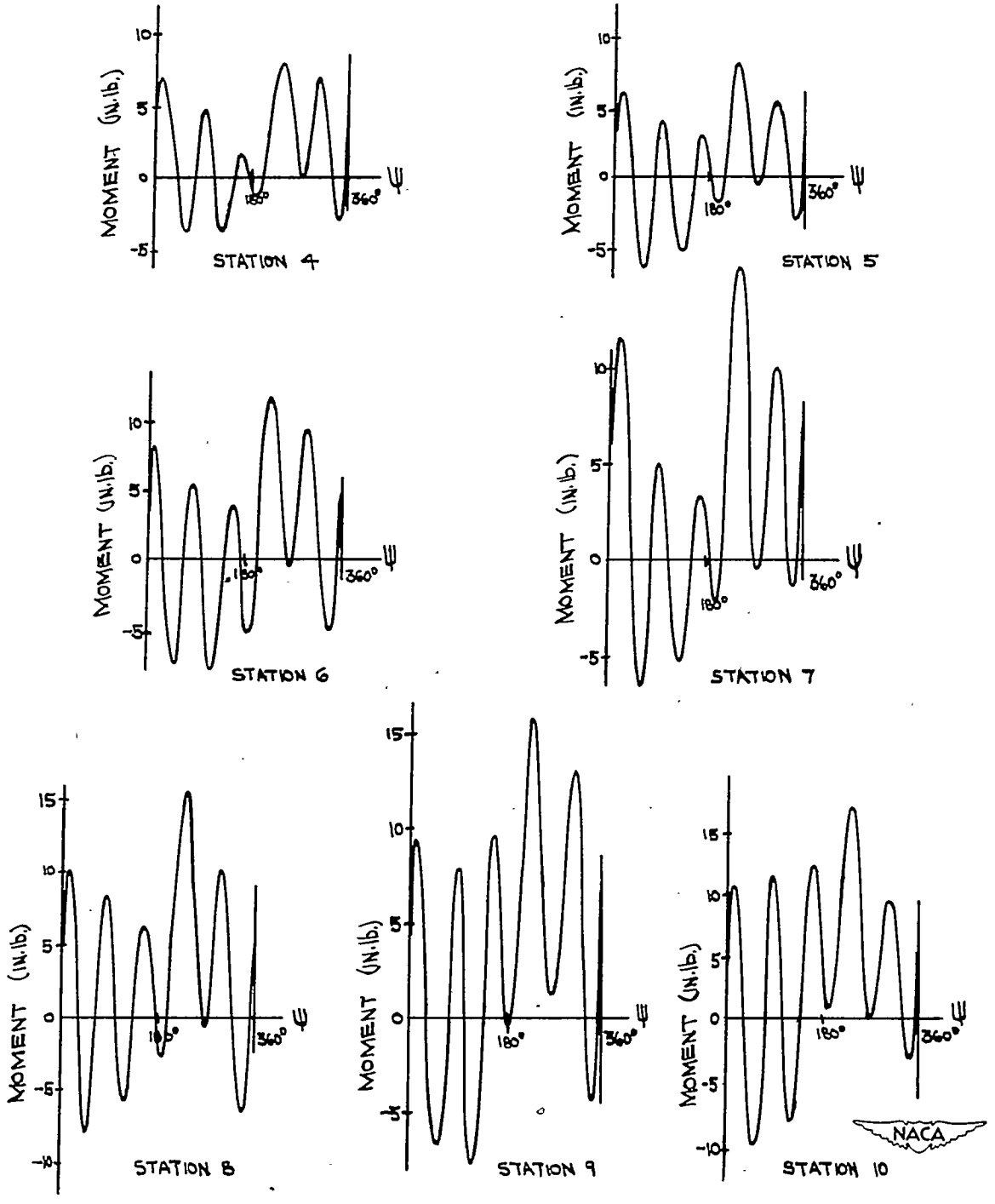

(d) $\mu = 0.40$.

Figure 7.- Continued.

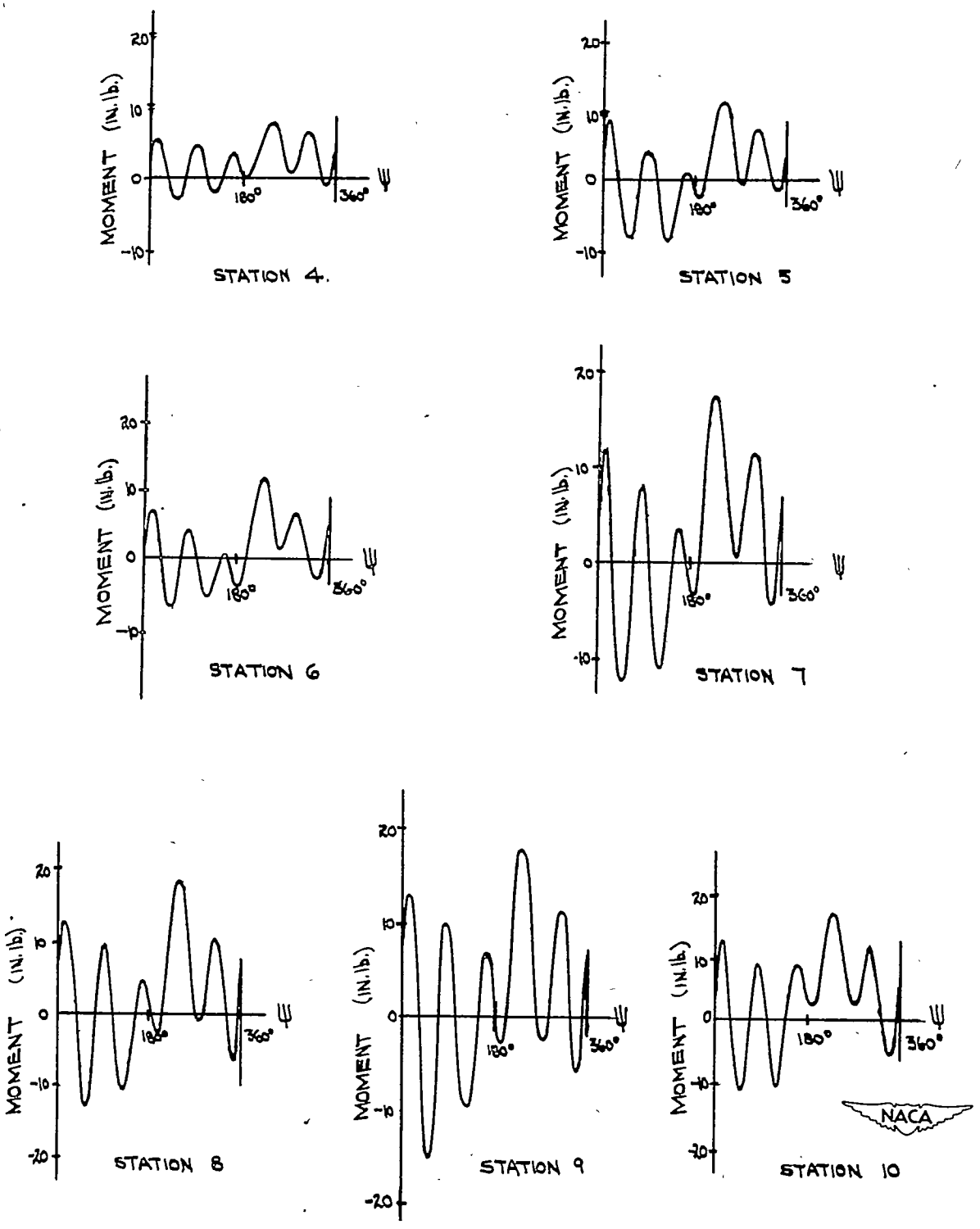

(e) $\mu = 0.50$.

Figure 7.- Concluded.

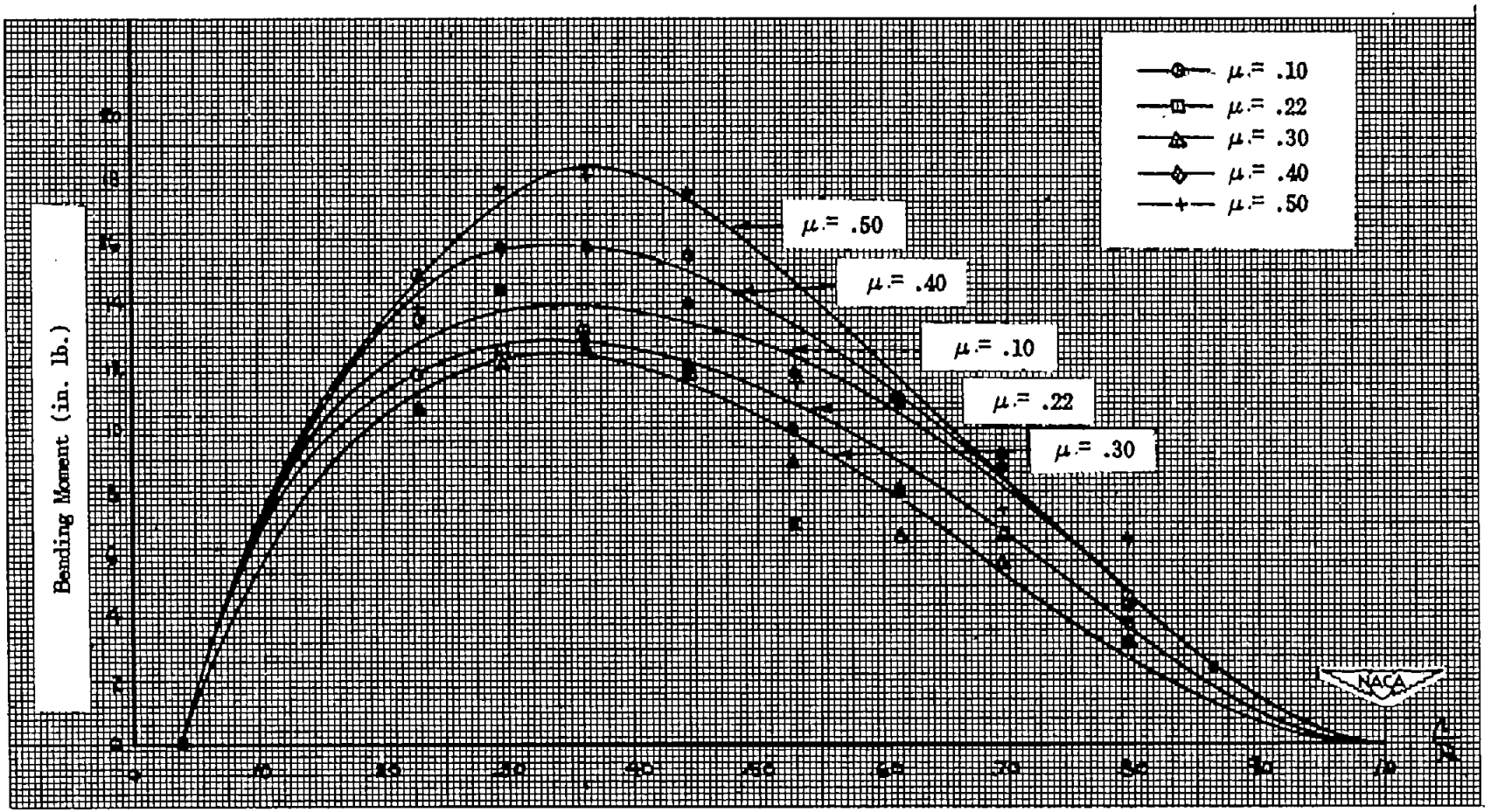

Figure 8.- Maximum-bending-moment distribution. Hinged-at-root condition; $\theta = 8^{\circ}$; $\alpha = -5^{\circ}$; $\psi = 235^{\circ}$; rotor speed, 800 rpm; EI = 16,000 pound-inches^2.

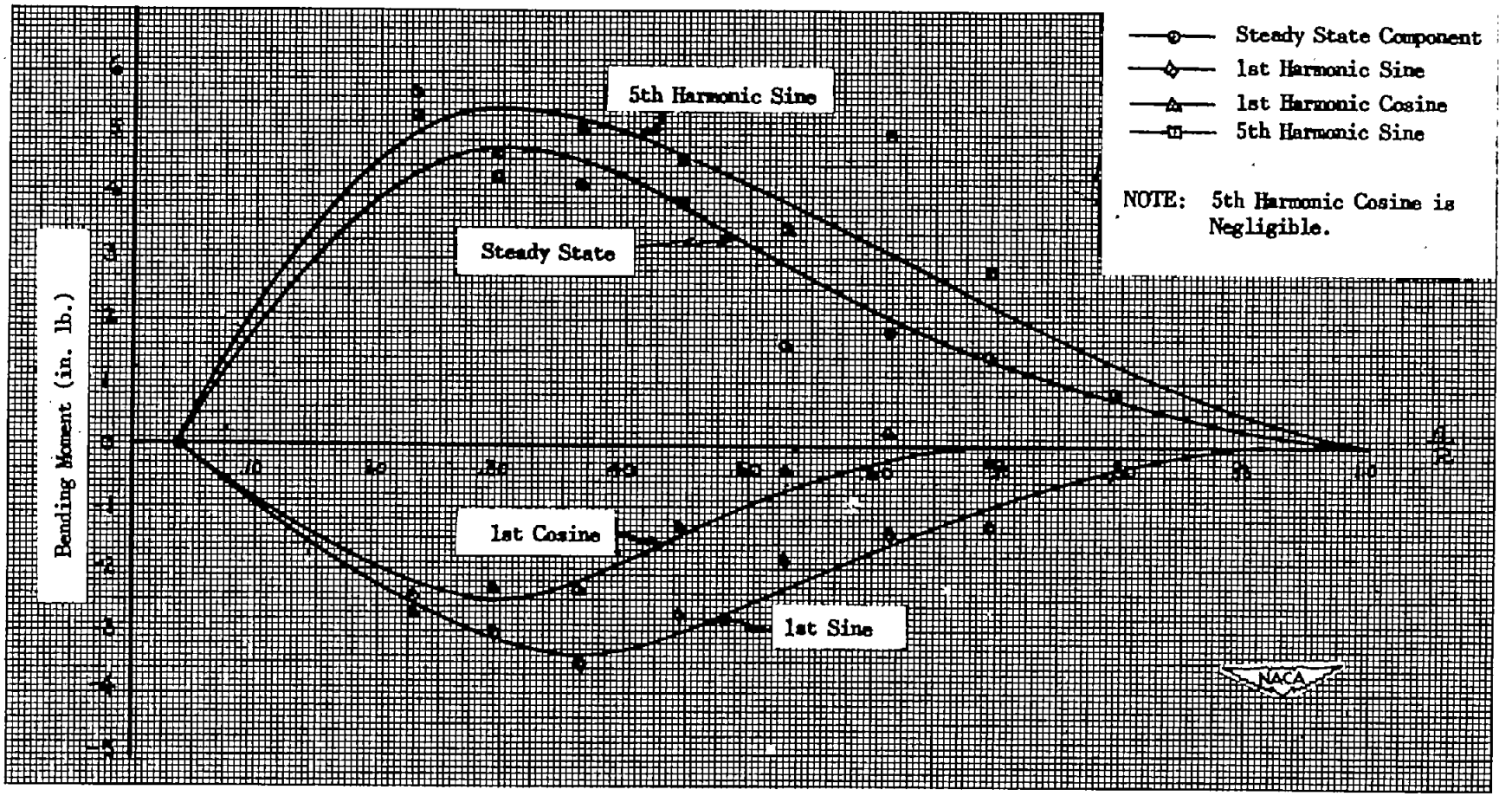

Figure 9.- Harmonic-bending-moment distribution. Hinged-at-root condition; $\mu = 0.22$; rotor speed, 800 rpm; $\theta = 8^{\circ}$; $\alpha = -5^{\circ}$; $\lambda = -0.0358$; $EI = 16{,}000$ pound-inches^2.

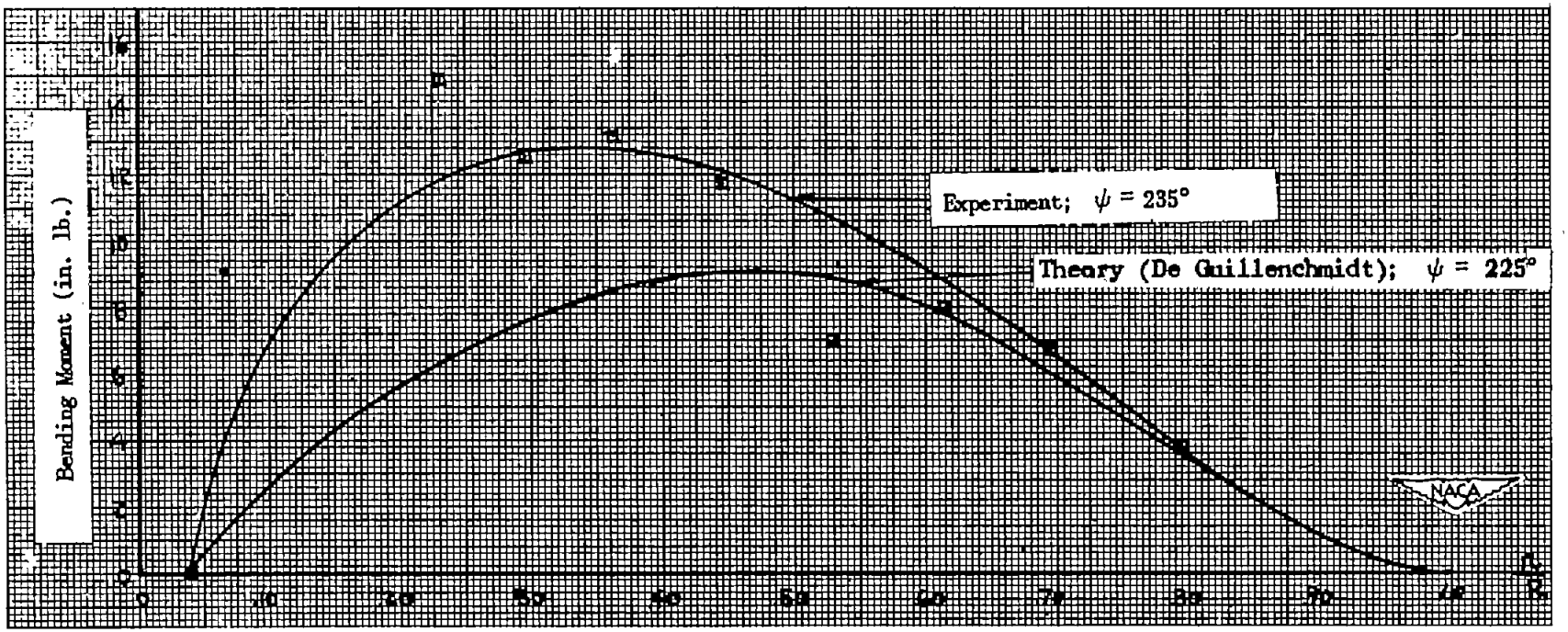

Figure 10.- Comparison of theoretical and experimental maximum-bending-moment distributions. Hinged-at-root condition; $\mu = 0.22$; rotor speed, 800 rpm; $\theta = 8^{\circ}$; $\alpha = -5^{\circ}$; $\lambda = -0.0358$; EI = 16,000 pound-inches^2.

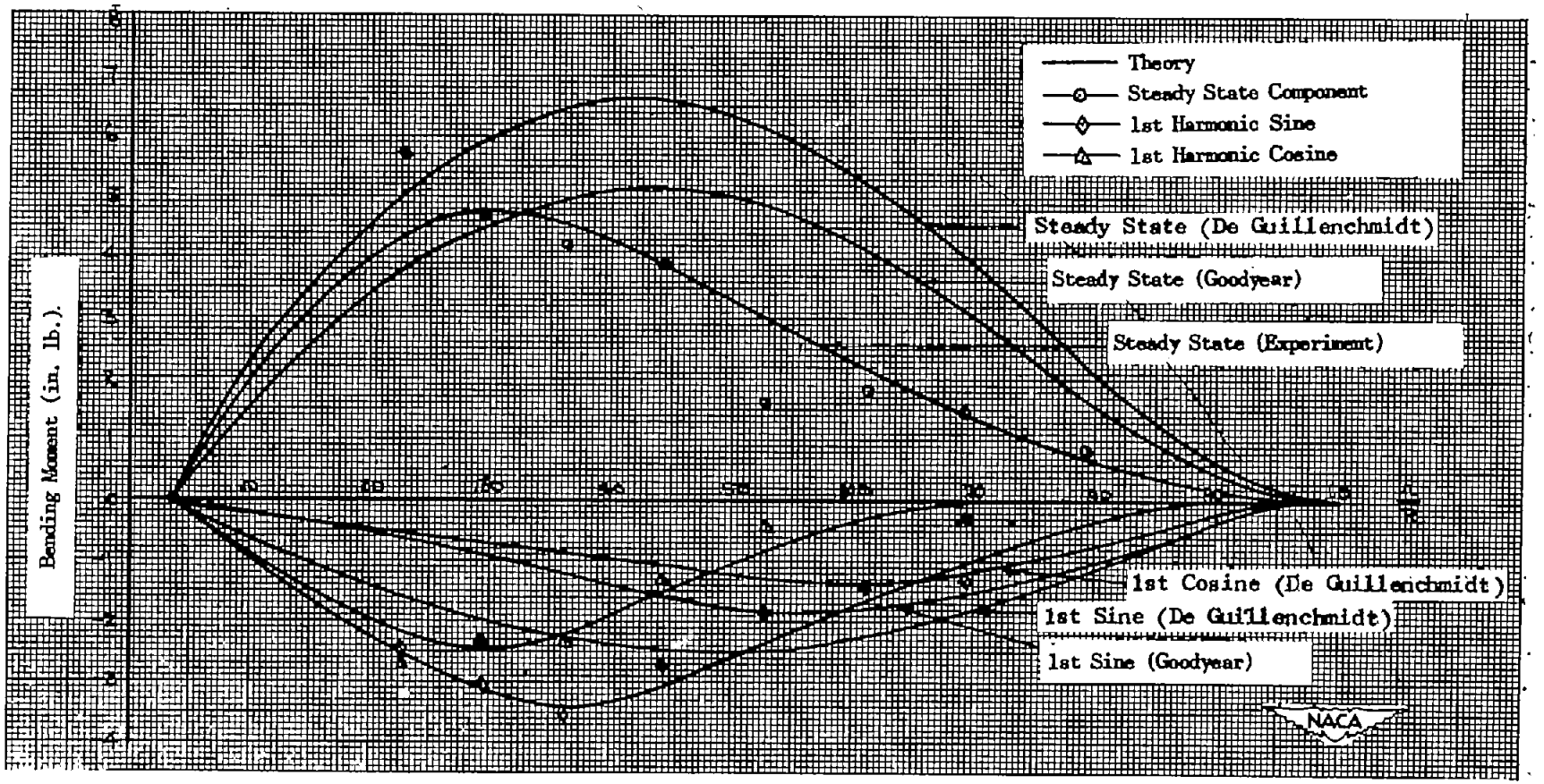

Figure 11.- Comparison of theoretical and experimental harmonic-bending-moment distributions. Hinged-at-root condition; $\mu = 0.22$; rotor speed, 800 rpm; $\theta = 8^{\circ}$; $\alpha = -5^{\circ}$; $\lambda = -0.0358$; EI = 16,000 pound-inches^2.

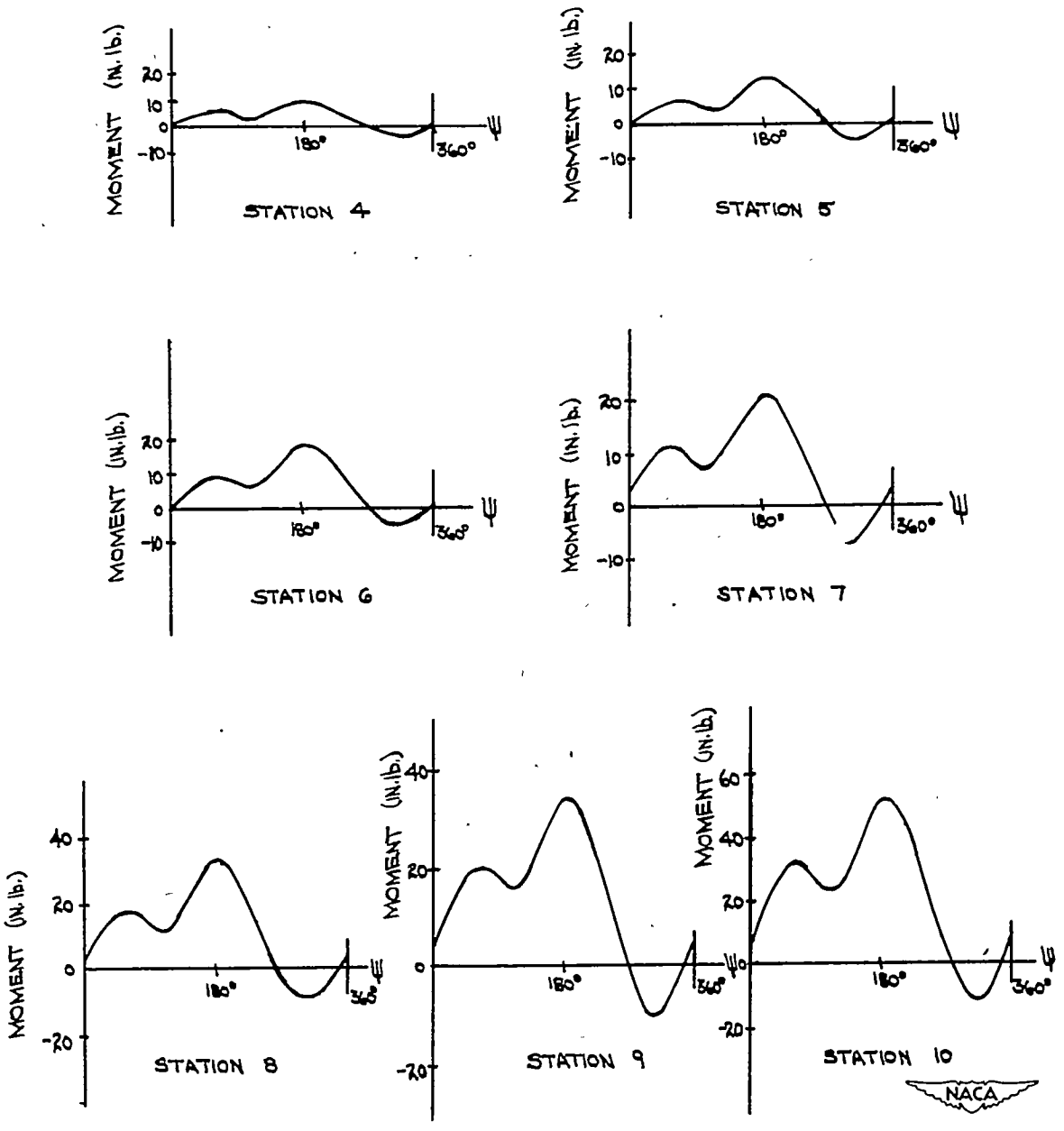

(a) $\mu = 0.15$; rotor speed, 600 rpm.

Figure 12.- Bending-moment traces from oscillograph records. Fixed-at-root condition; $\theta_0 = 8^{\circ}$; $\alpha = -5^{\circ}$.

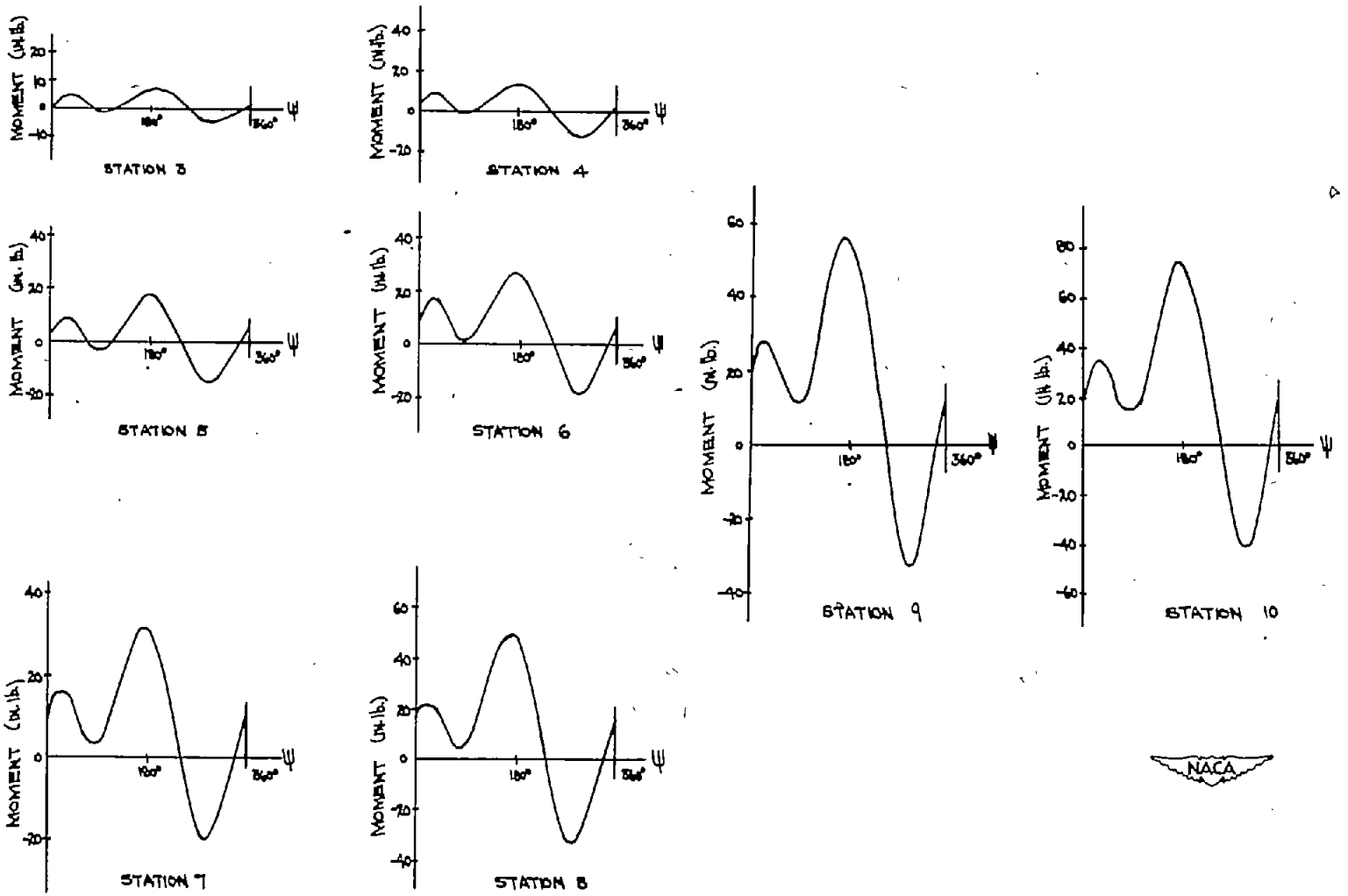

(b) $\mu = 0.30$; rotor speed, 600 rpm.

Figure 12.- Continued.

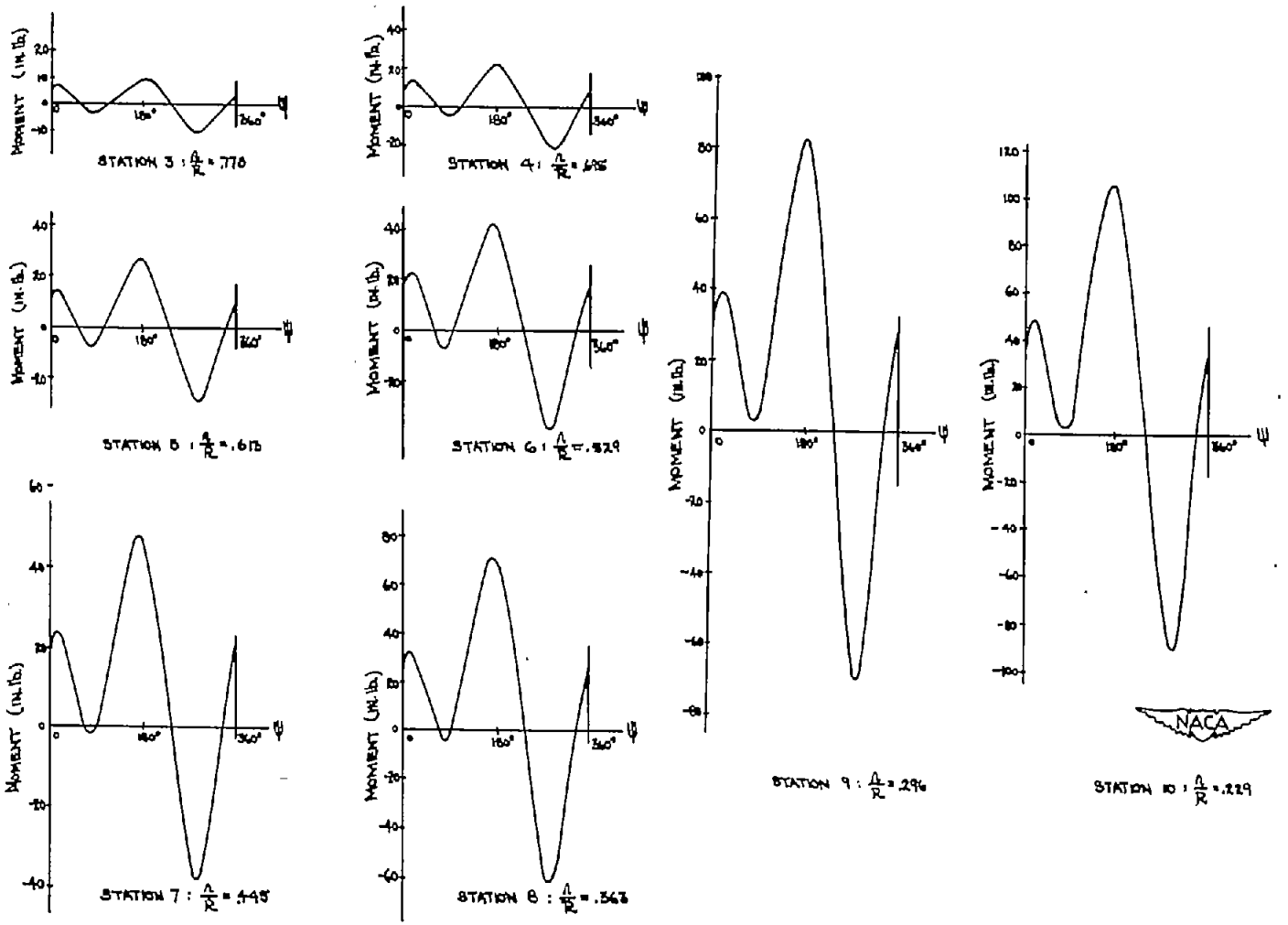

(c) μ = 0.47; rotor speed, 600 rpm.

Figure 12.- Continued.

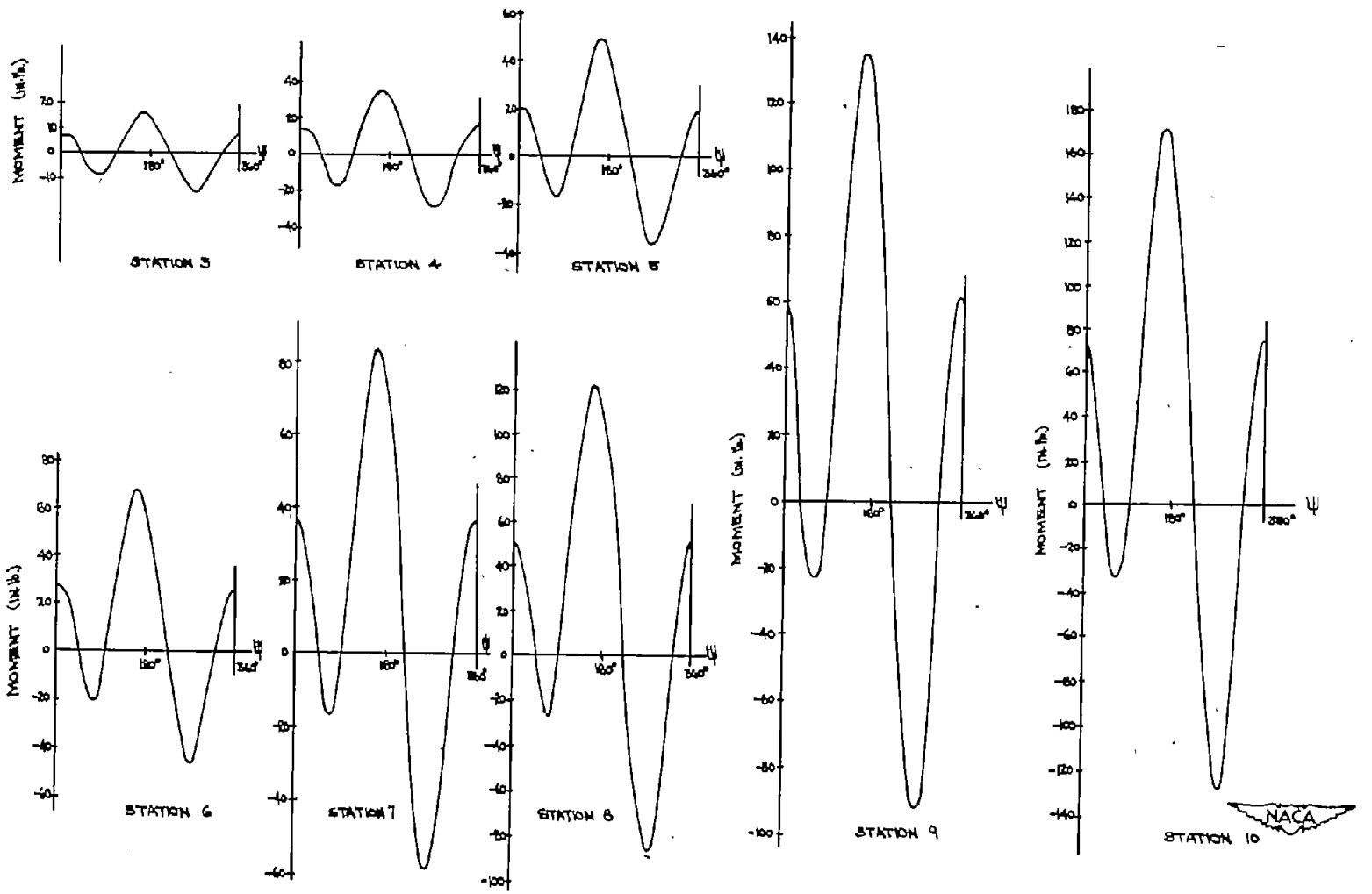

(d) $\mu = 0.60$; rotor speed, 600 rpm.

Figure 12.- Continued.

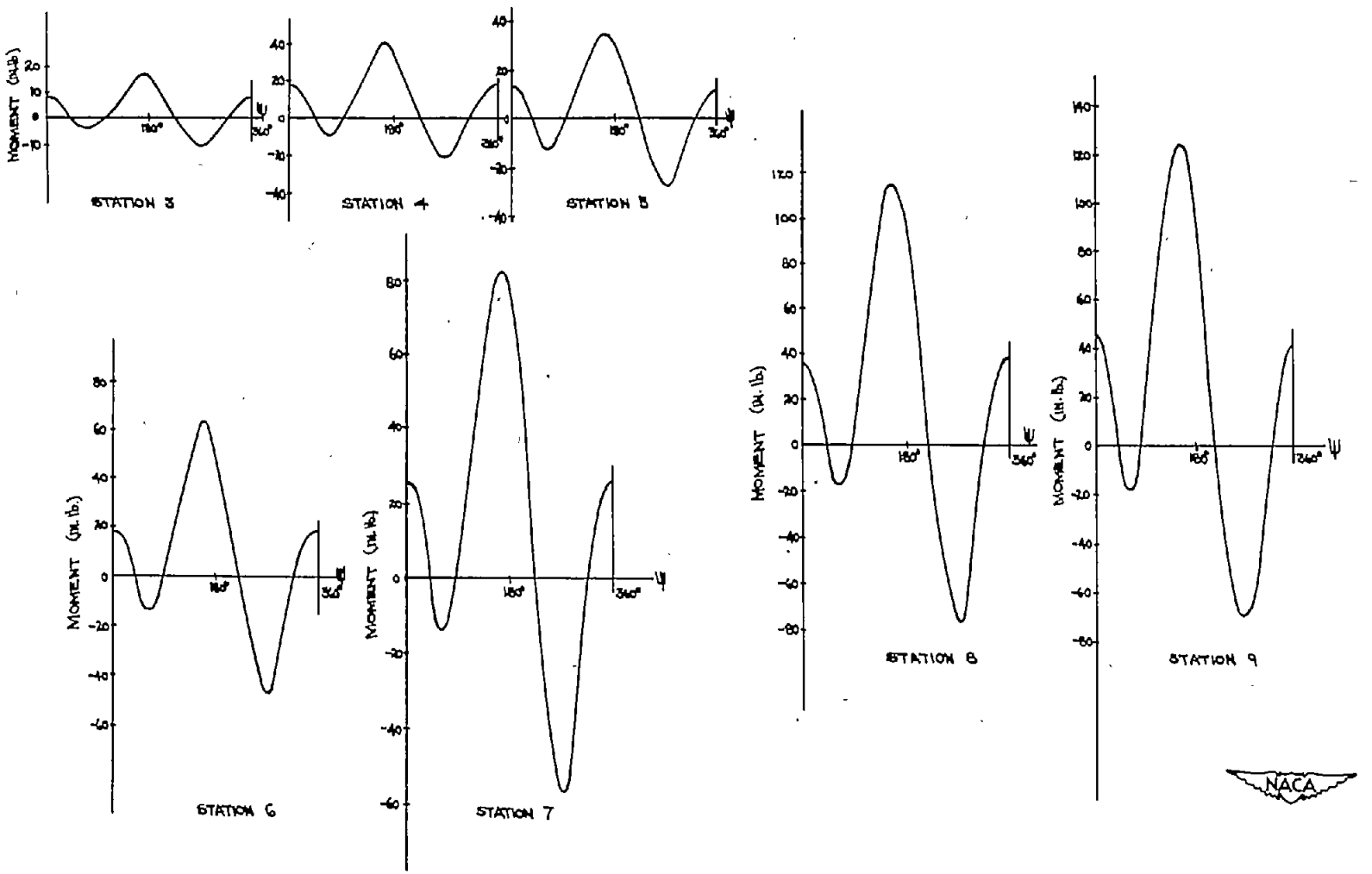

(e) $\mu = 0.80$; rotor speed, 500 rpm.

Figure 12.- Continued.

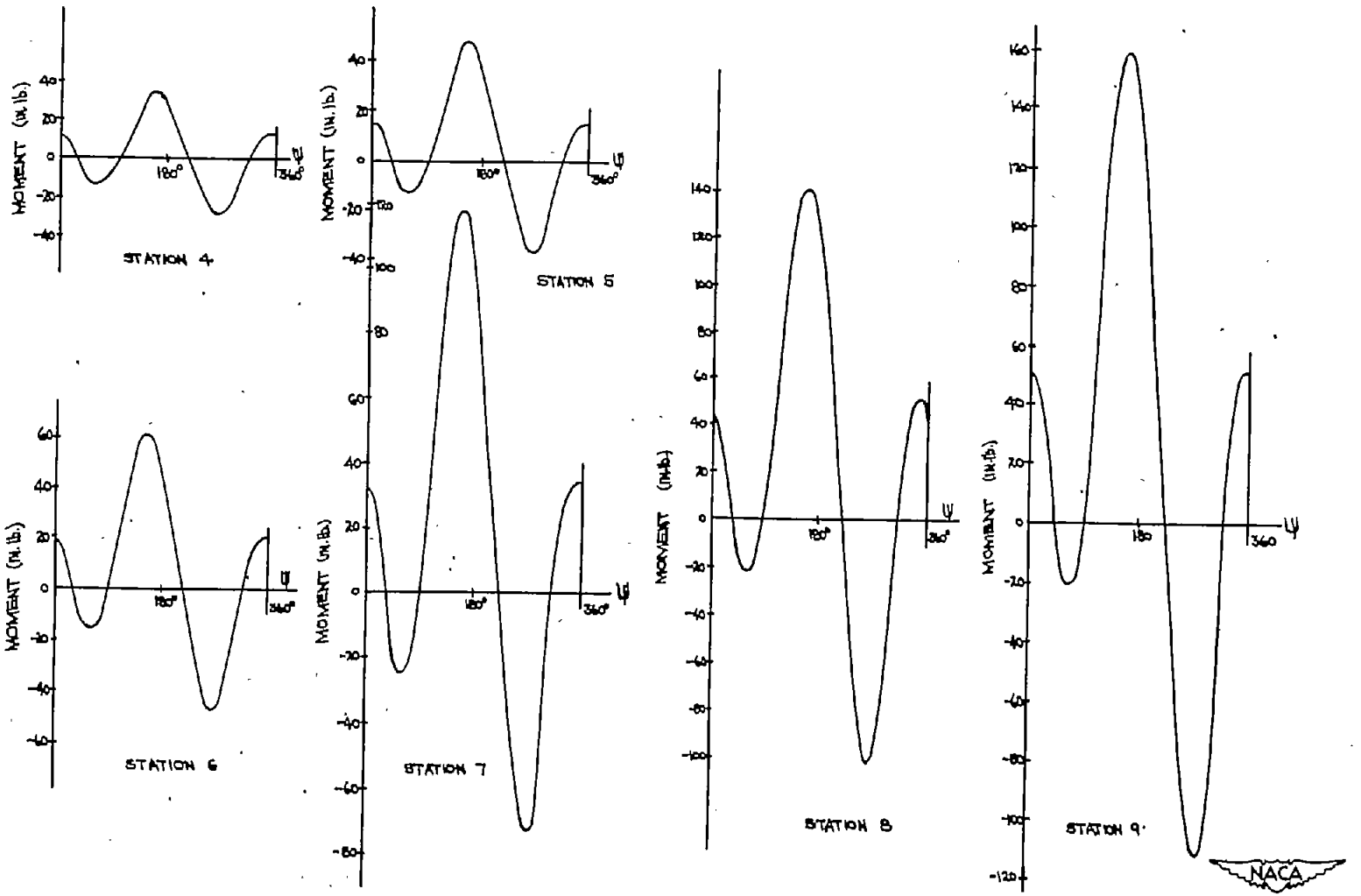

(f) $\mu = 0.90$; rotor speed, 500 rpm.

Figure 12.- Concluded.

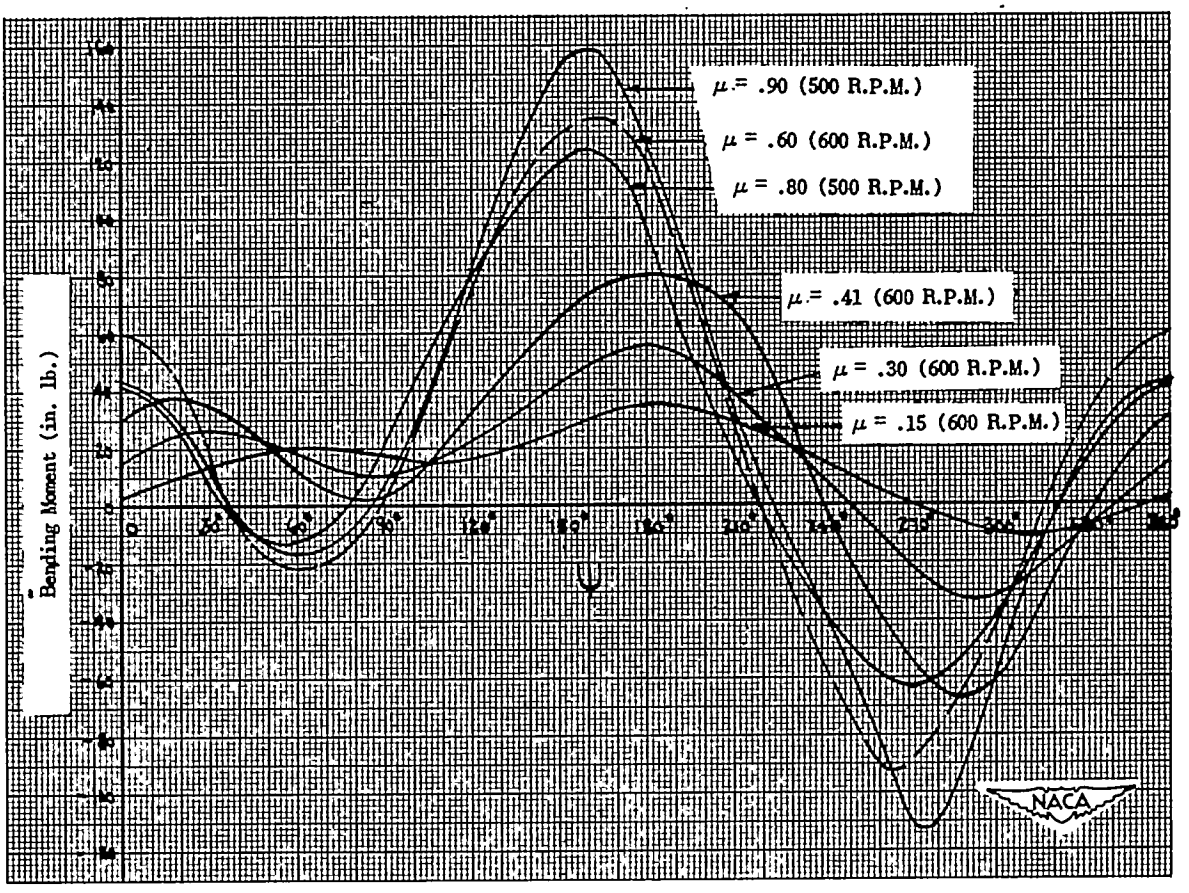

Figure 13.- Sample traces from oscillograph records. Fixed-at-root condition; $\theta = 8^{\circ}$; $\alpha = -5^{\circ}$; station 9, $r/R = 0.296$.

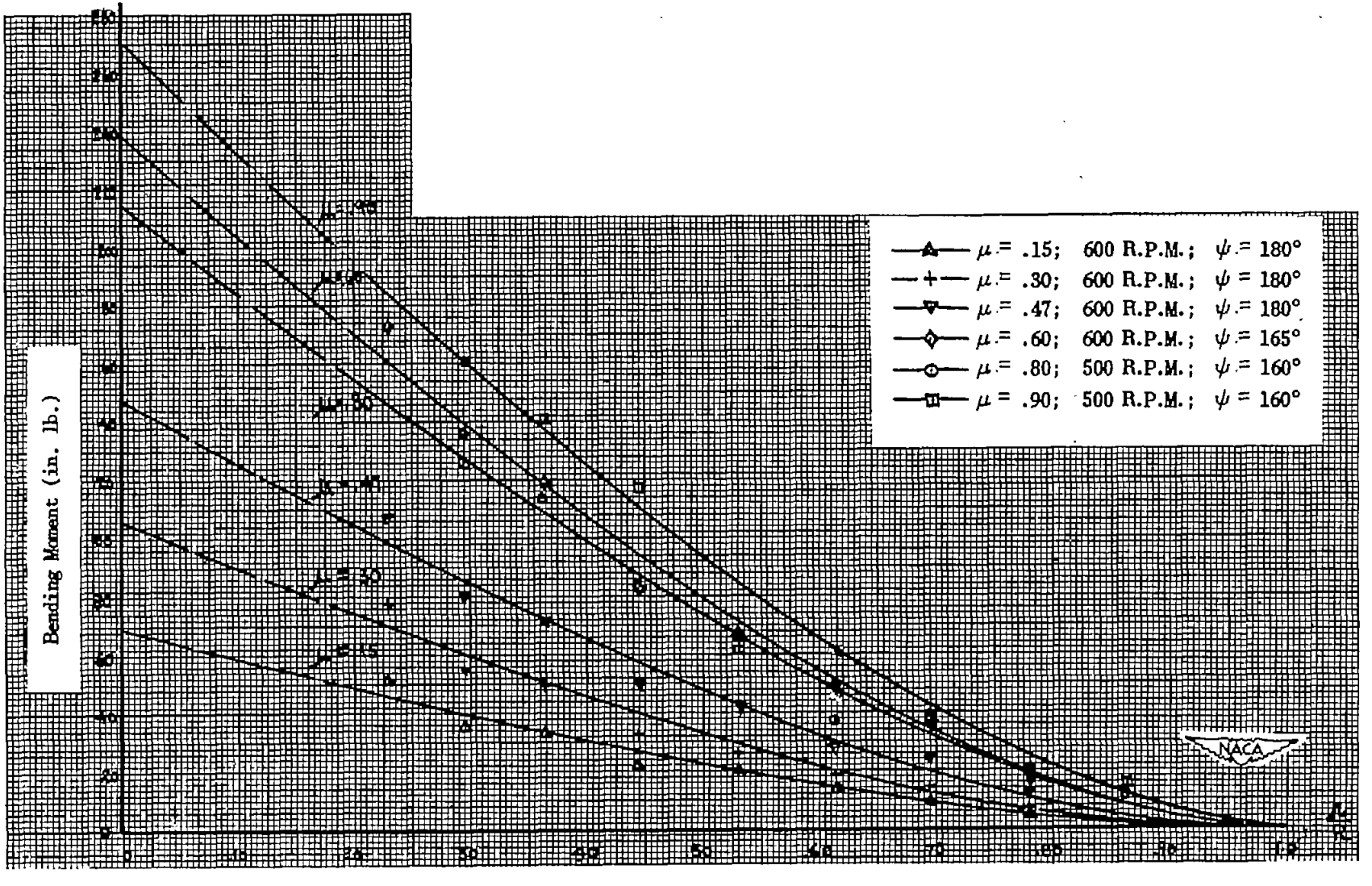

Figure 14.- Maximum-bending-moment distribution. Fixed-at-root condition; $\beta = 0^{\circ}$; $\theta = 8^{\circ}$; $\alpha = -5^{\circ}$; EI = 16,000 pound-inches^2.

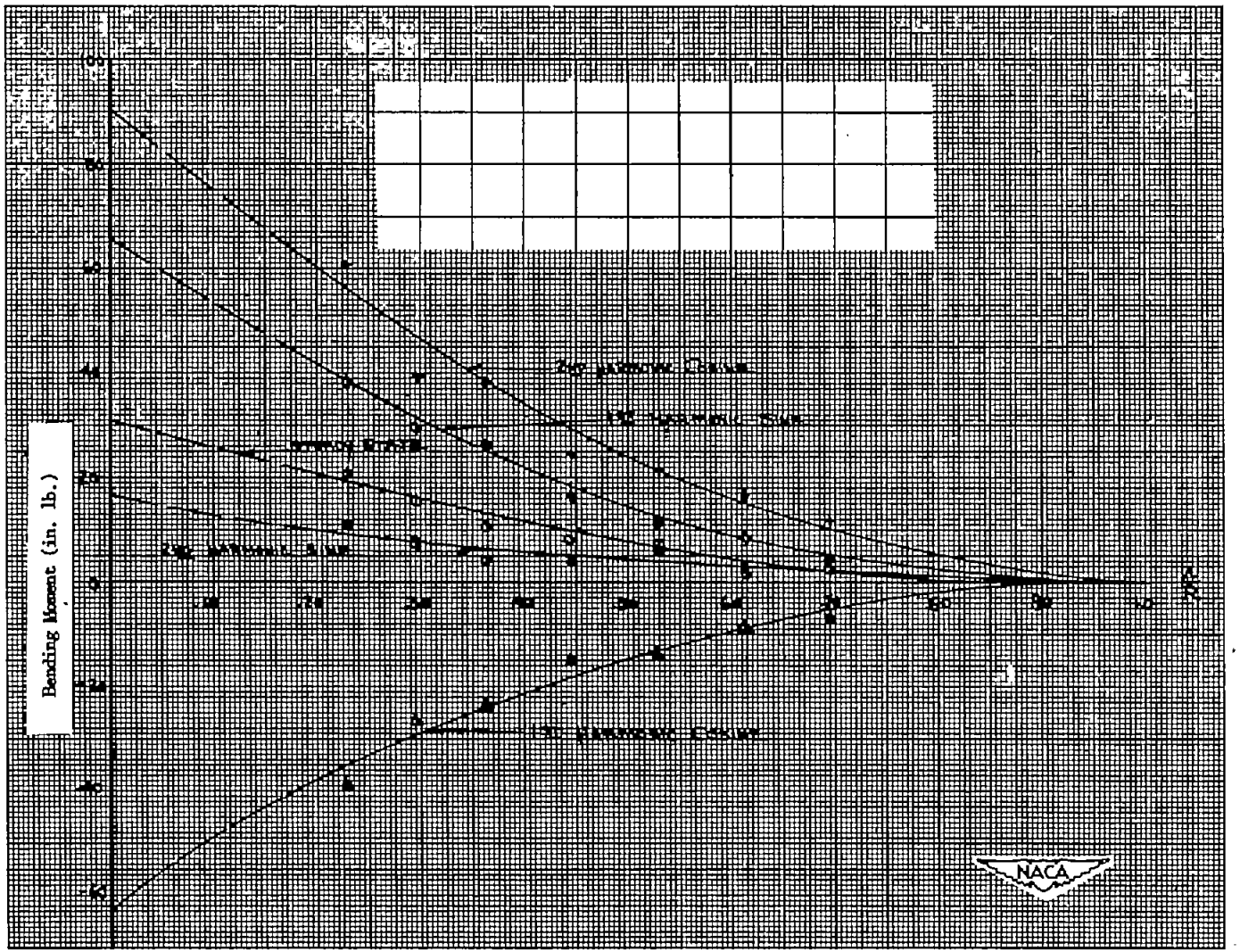

Figure 15.- Harmonic-bending-moment distribution. Fixed-at-root condition; $\mu = 0.47$; rotor speed, 600 rpm; $\beta = 0^{\circ}$; $\theta = 8^{\circ}$; $\alpha = -5^{\circ}$; $\lambda = -0.0457$; EI = 16,000 pound-inches^2.

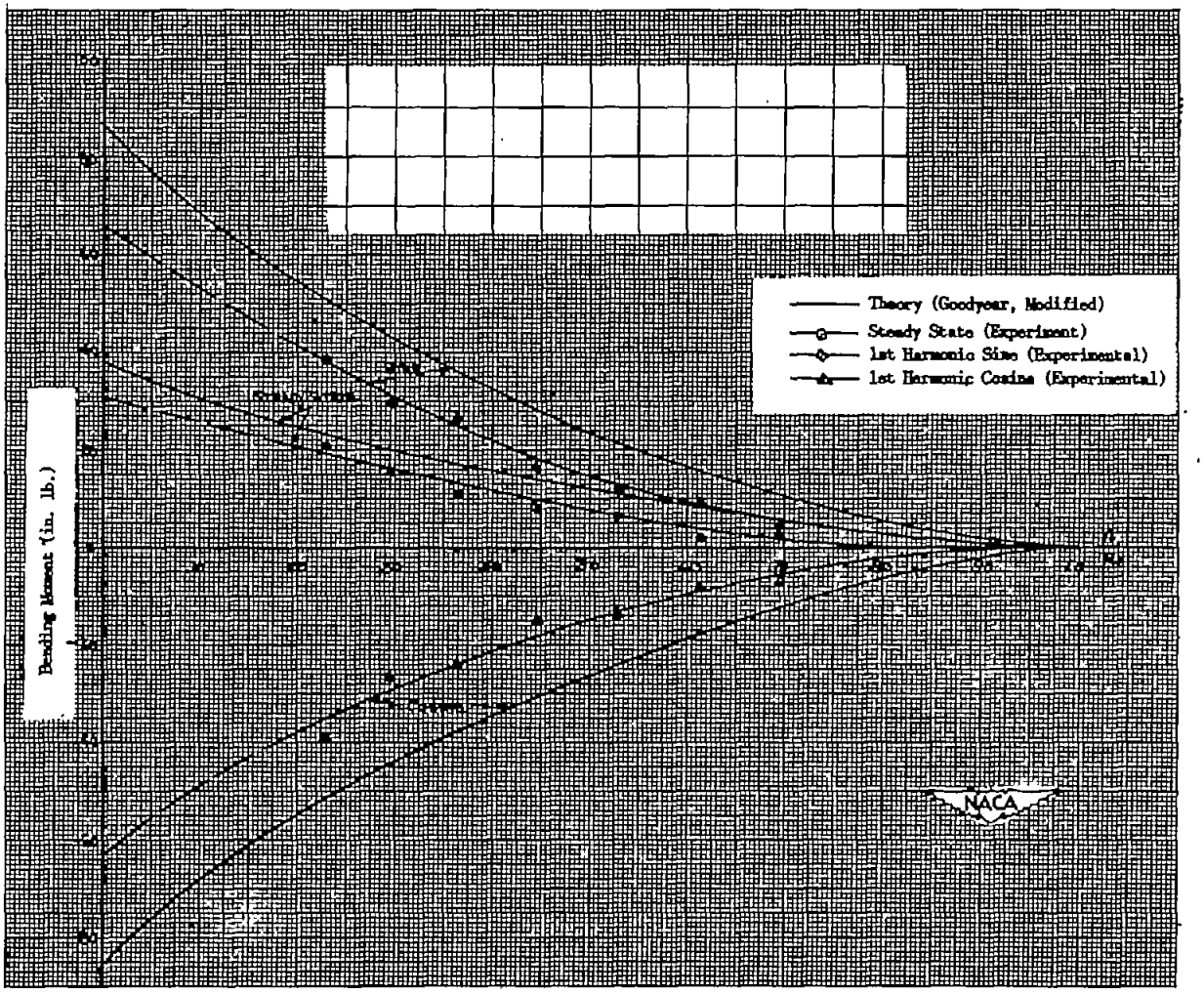

Figure 16.- Comparison of theoretical and experimental harmonic-bending-moment distributions. Fixed-at-root condition; $\mu = 0.47$; rotor speed, 600 rpm; $\beta = 0^{\circ}$; $\theta = 8^{\circ}$; $\alpha = -5^{\circ}$; $\lambda = -0.0457$; EI = 16,000 pound-inches^2.

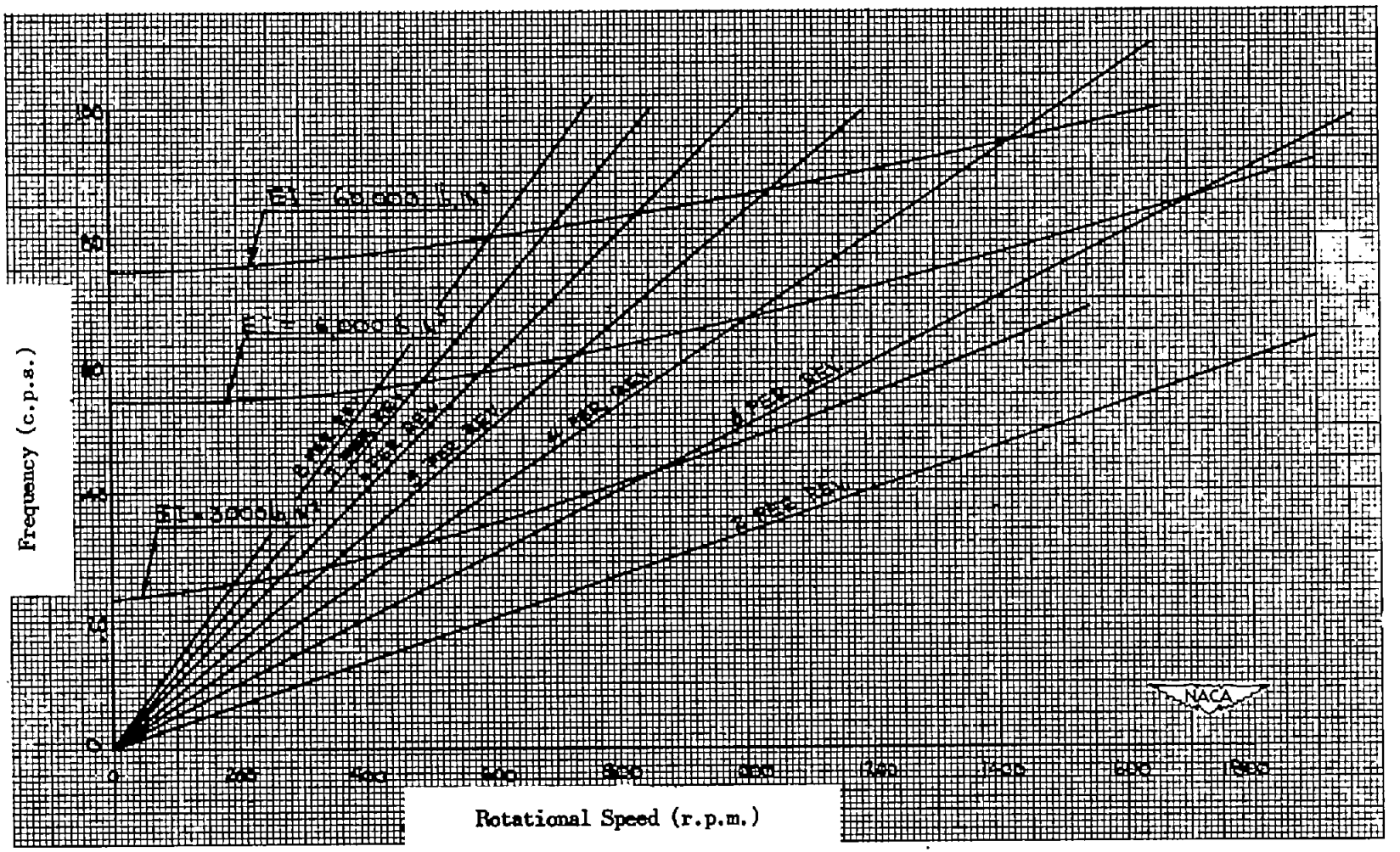

(a) Hinged-at-root condition.

Figure 17.- Variation of first natural bending frequency of rotor blades of different stiffnesses with rotational speed.

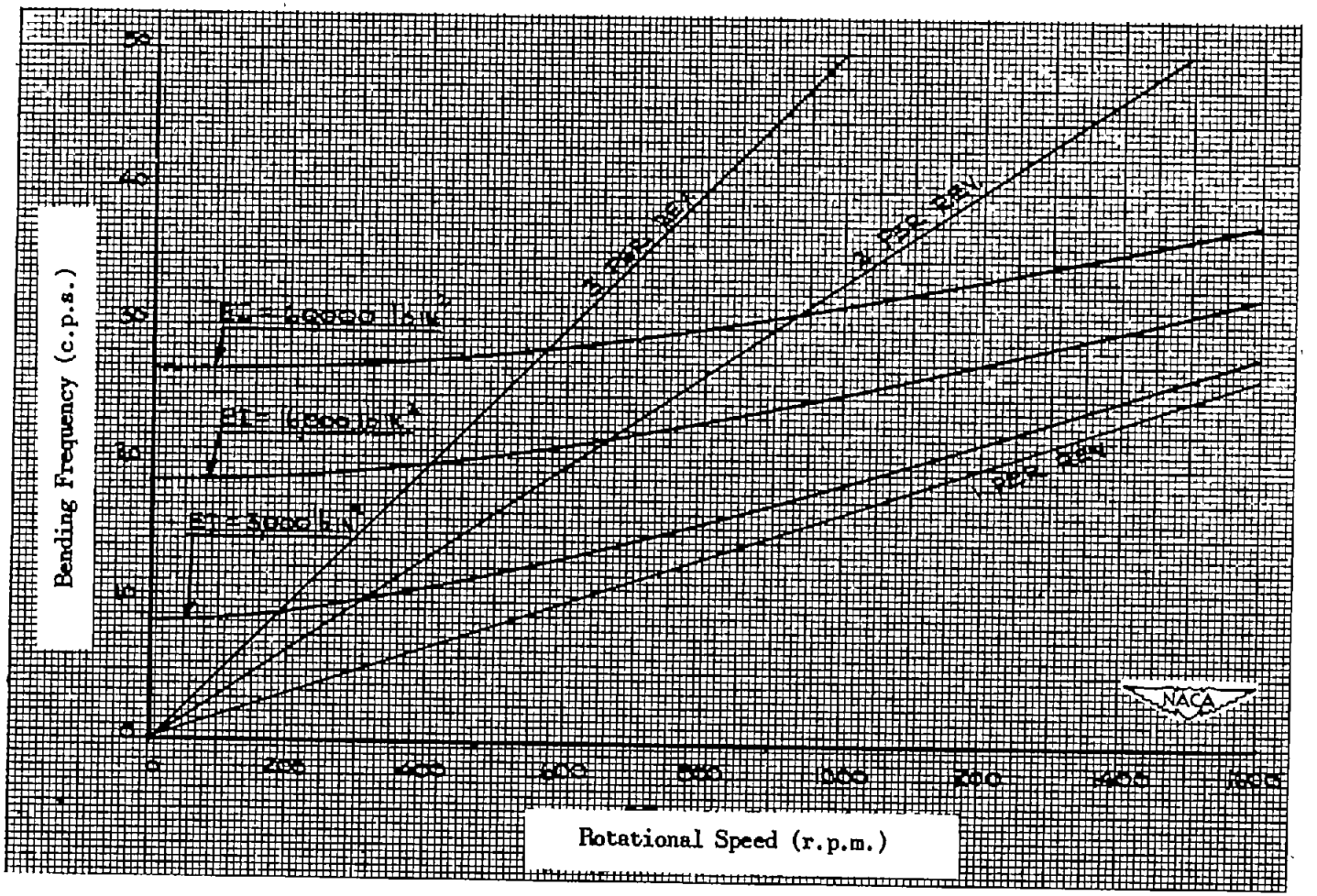

(b) Fixed-at-root condition.

Figure 17.- Concluded.

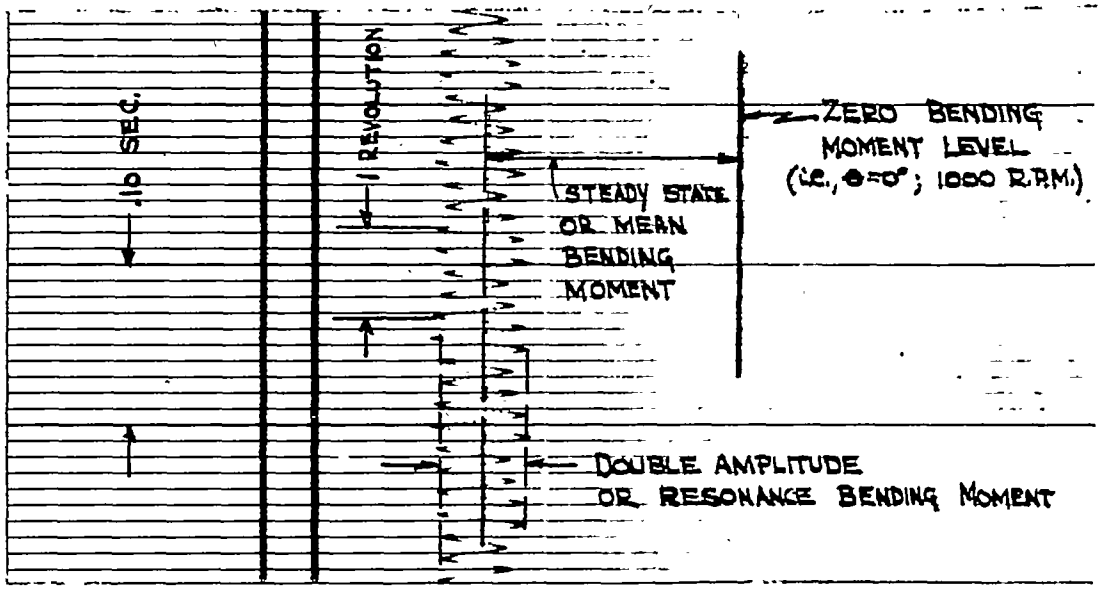

(a) Hinged-at-root condition; rotor speed, 1000 rpm.

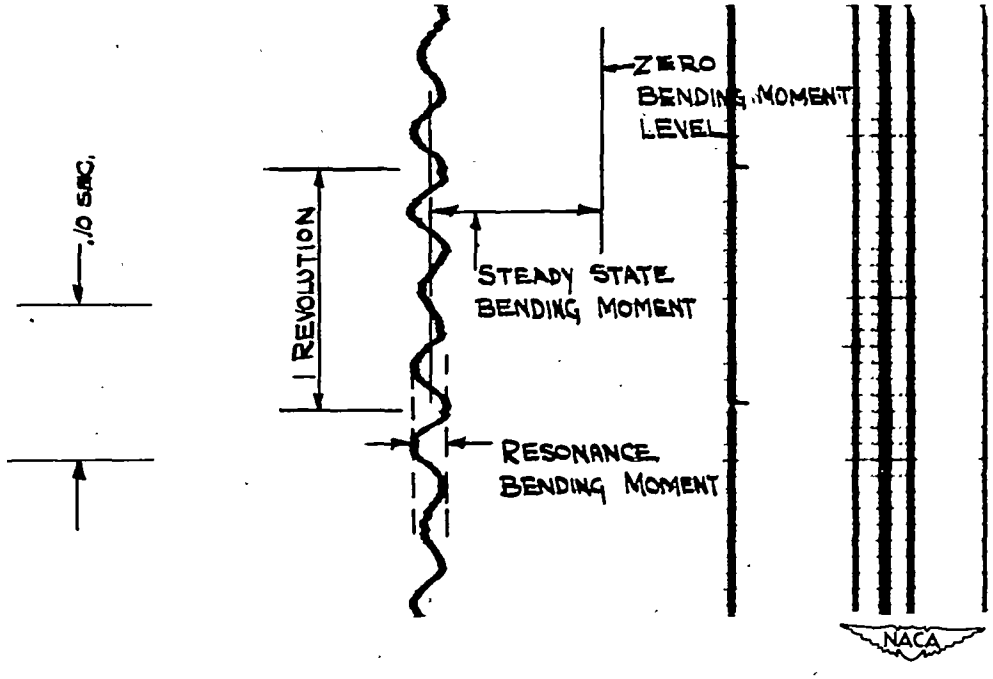

(b) Fixed-at-root condition; rotor speed, 400 rpm.

Figure 18.- Sample oscillograph records showing resonance phenomenon. $\theta = 12^{\circ}$; EI = 16,000 pound-inches^2.

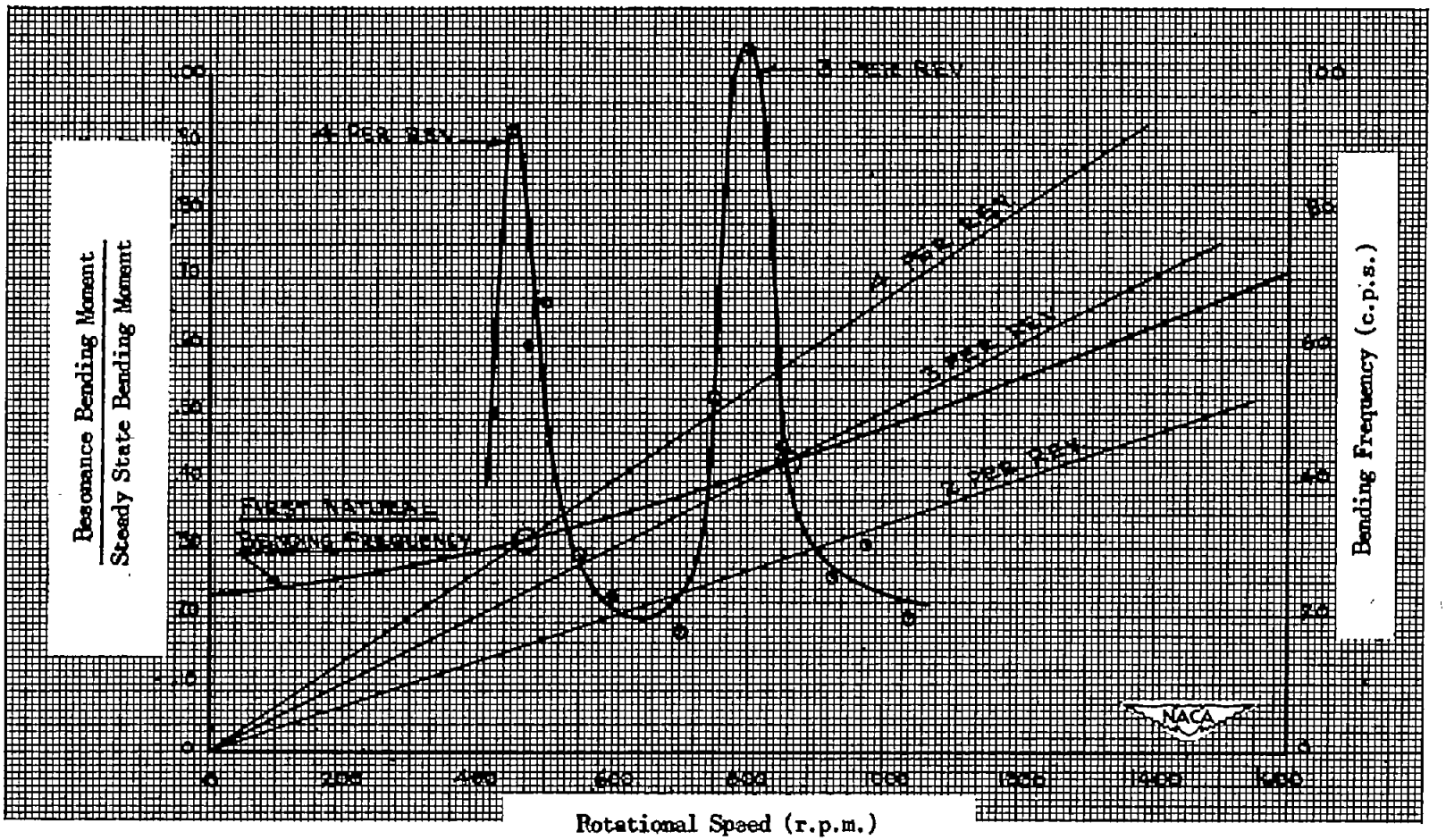

(a) EI = 3000 pound-inches^2.

Figure 19.- Rotor-blade resonance study. Hovering, hinged-at-root condition; $\theta = 12^{\circ}$.

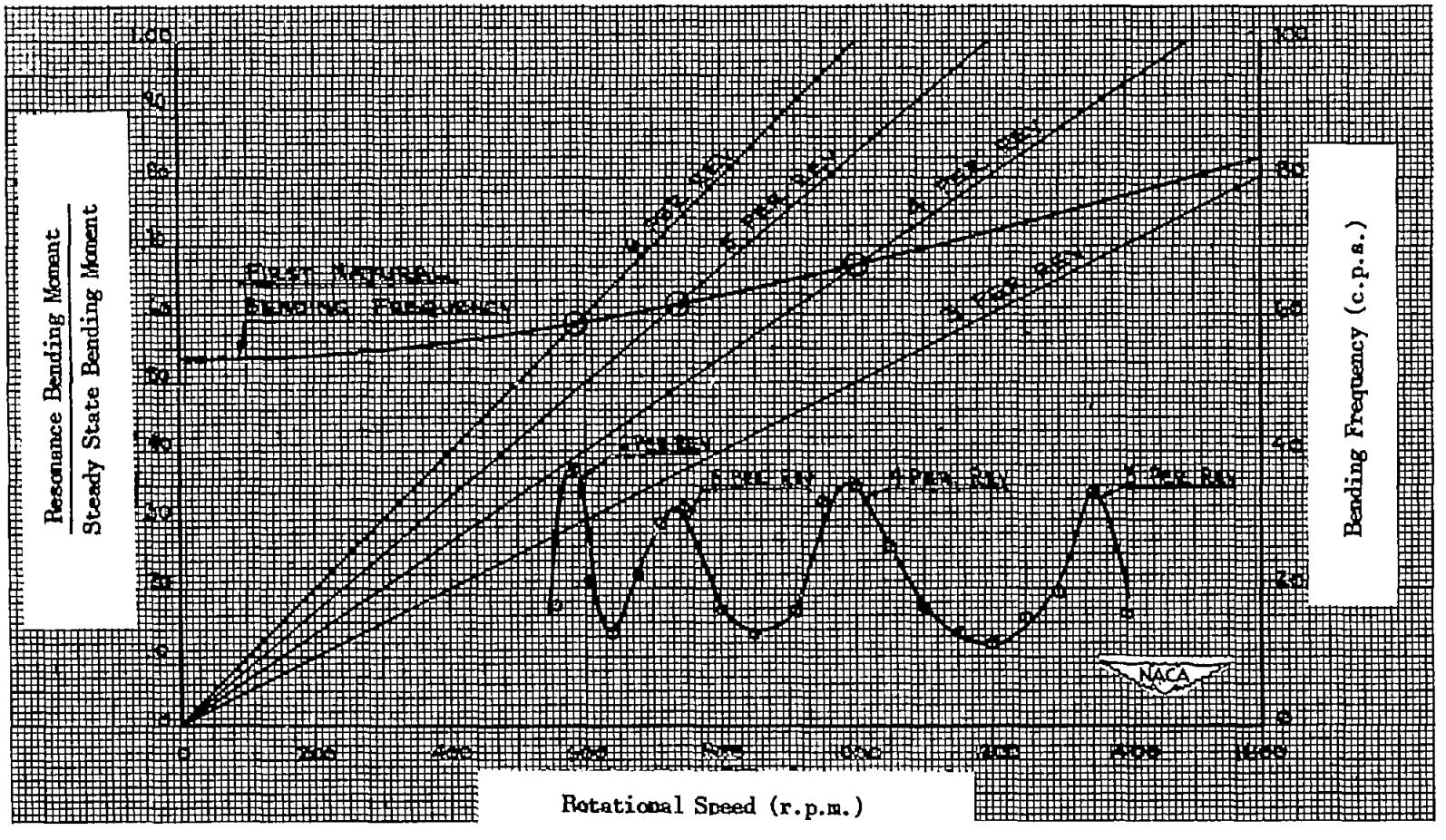

(b) EI = 16,000 pound-inches^2.

Figure 19.- Continued.

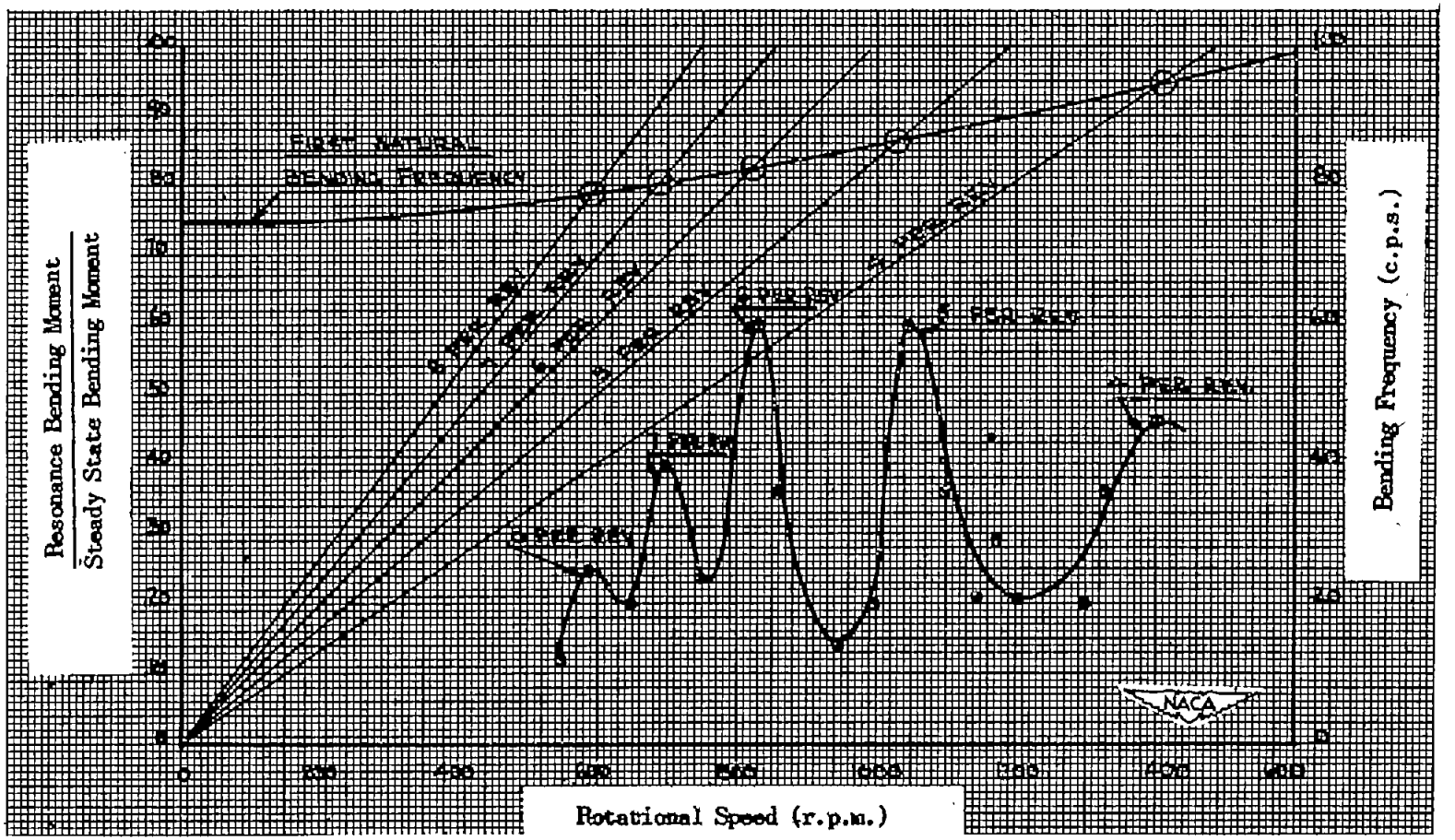

(c) EI = 60,000 pound-inches^2.

Figure 19.- Concluded.

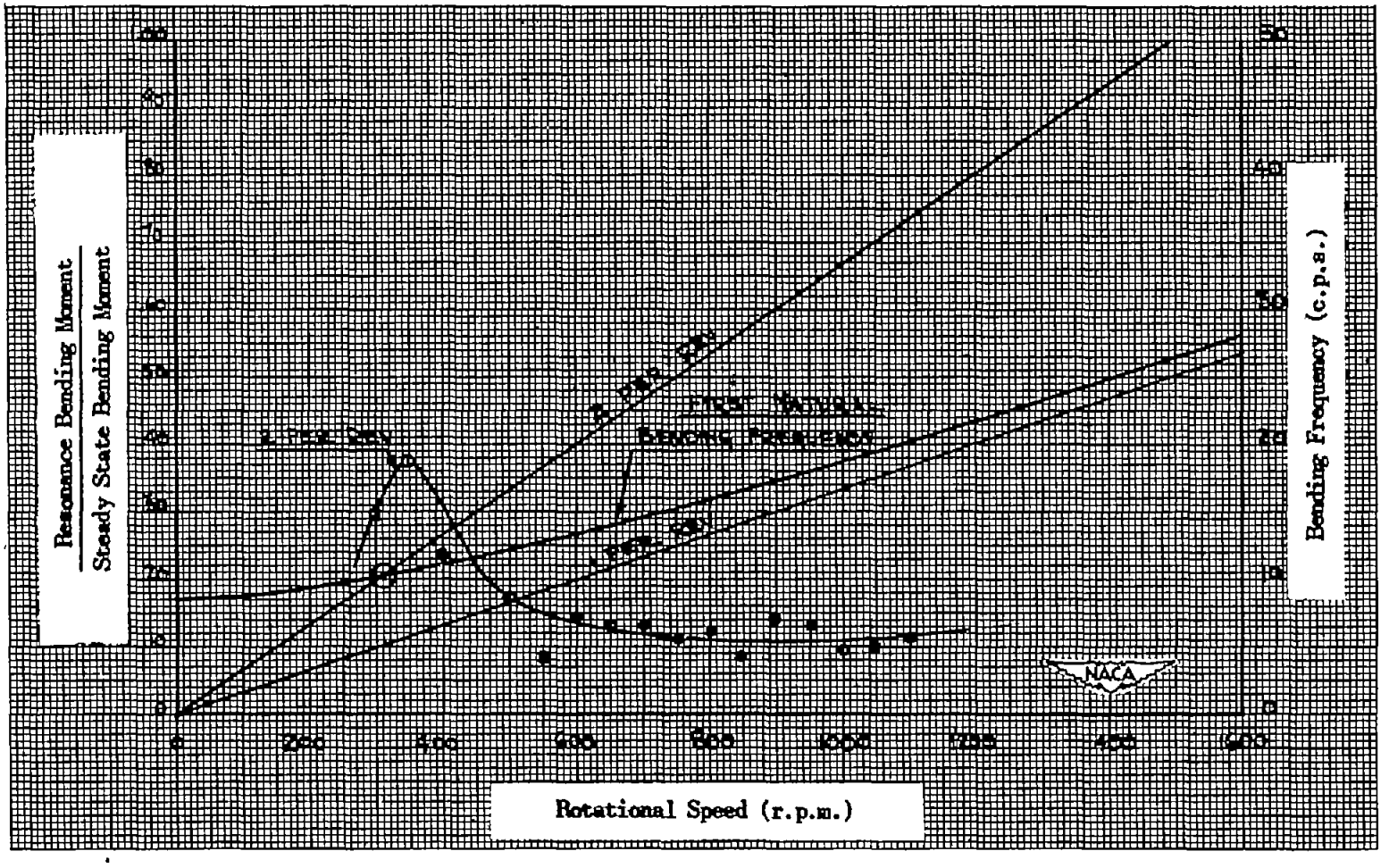

(a) EI = 3000 pound-inches^2.

Figure 20.- Rotor-blade resonance study. Hovering, fixed-at-root condition; $\theta = 12^{\circ}$.

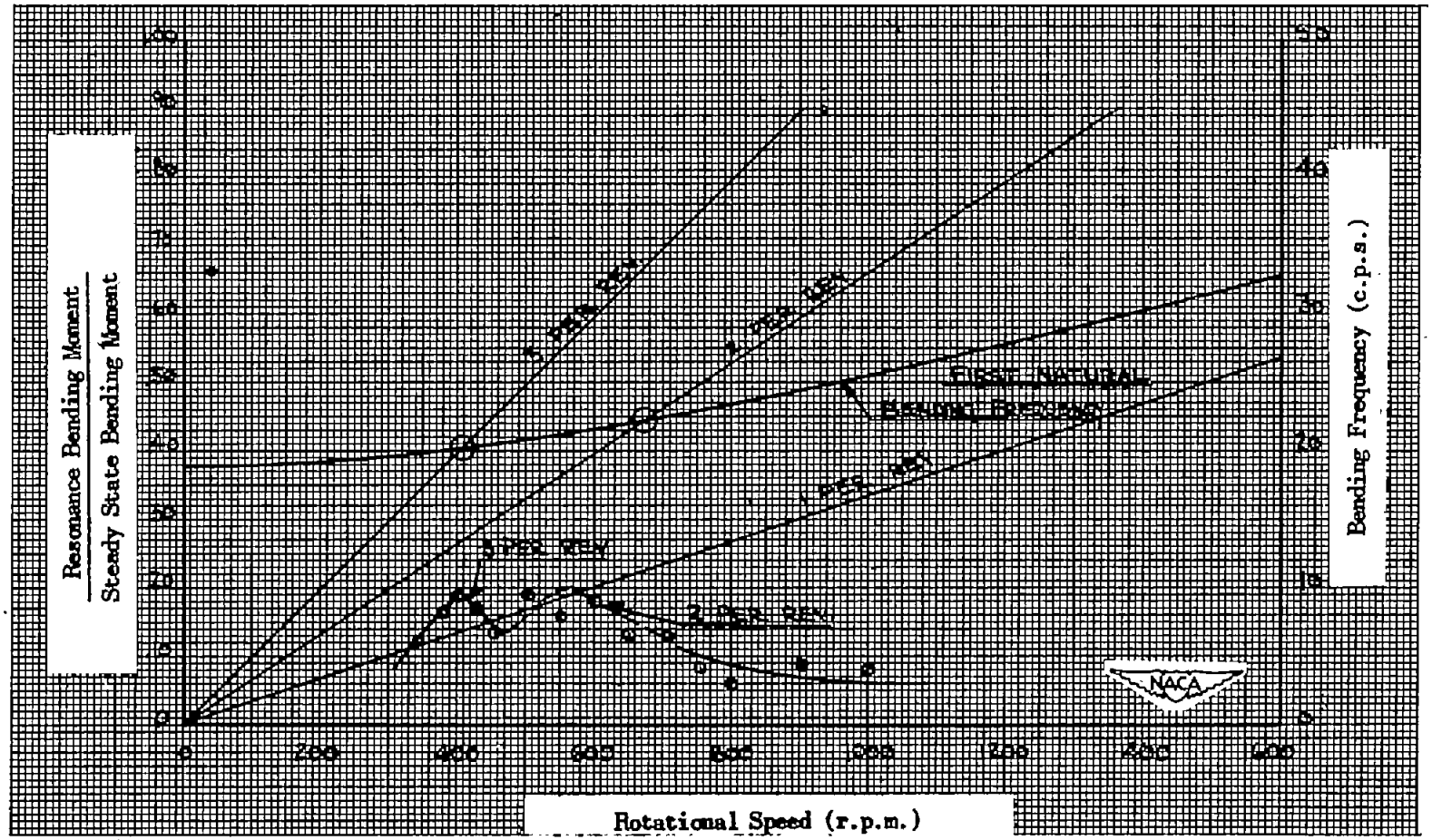

(b) EI = 16,000 pound-inches^2.

Figure 20.- Continued.

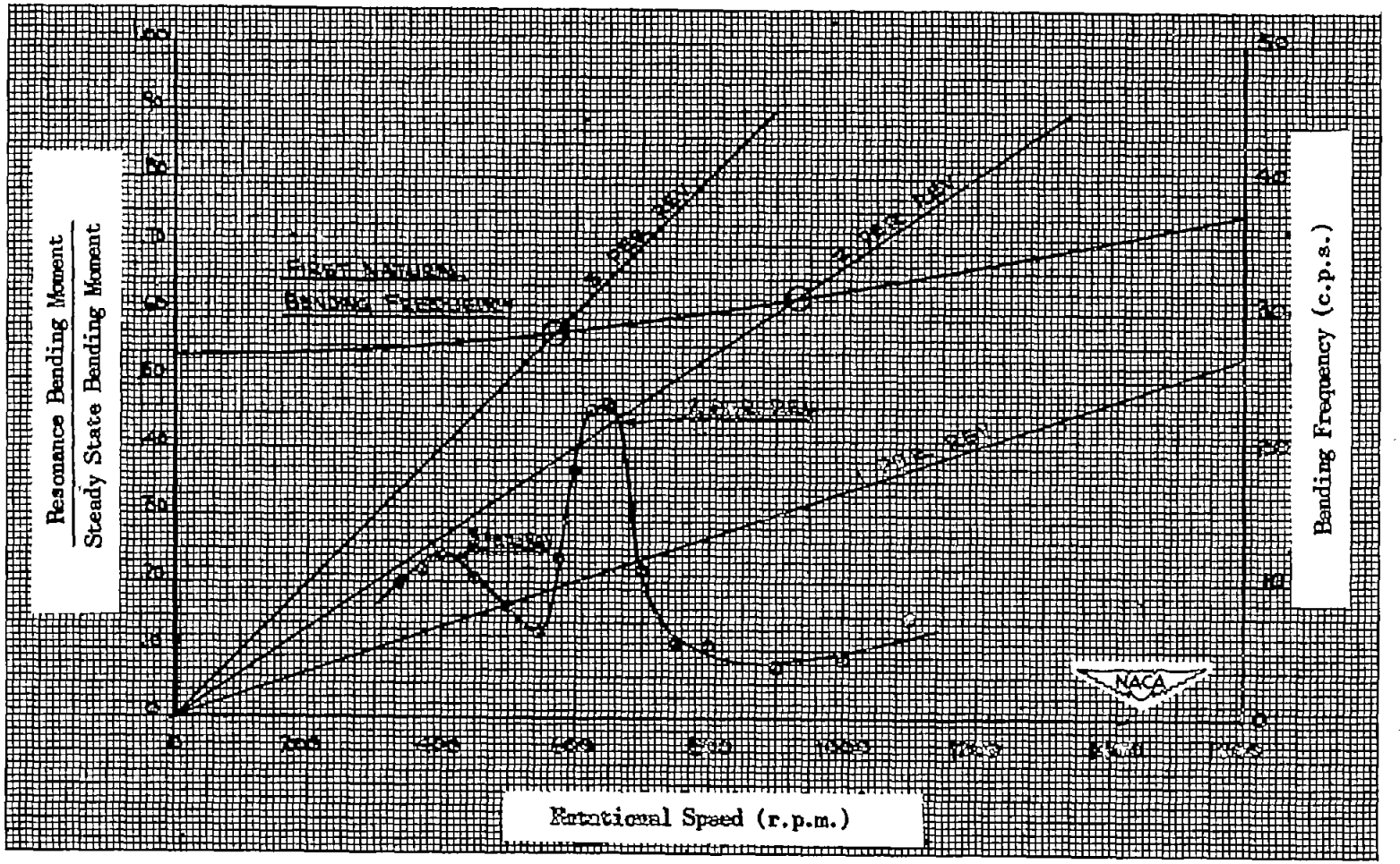

(c) EI = 60,000 pound-inches^2.

Figure 20.- Concluded.

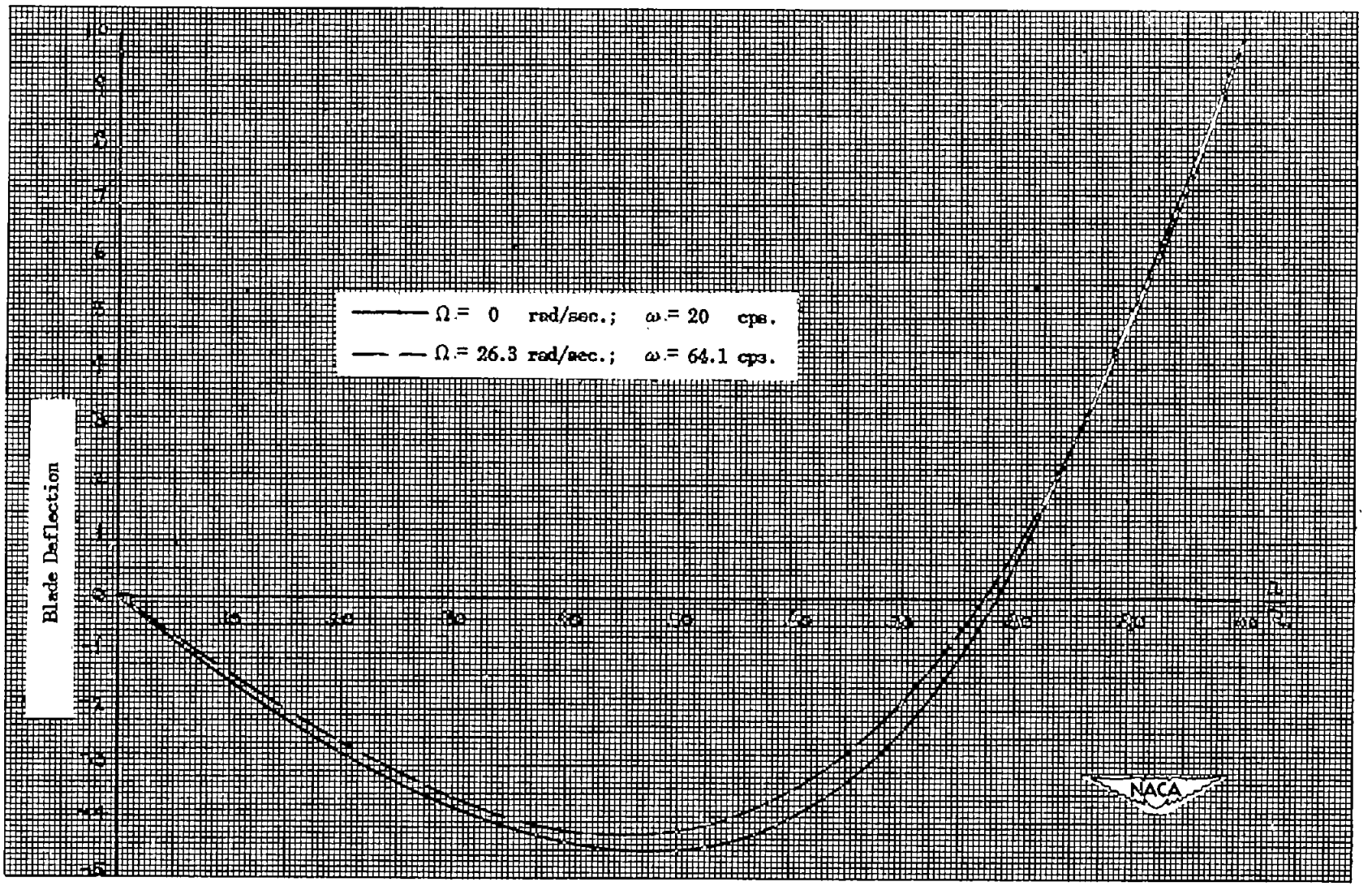

Figure 21.- Comparison between rotating and nonrotating natural bending modes of the full-scale R-6 rotor blade.

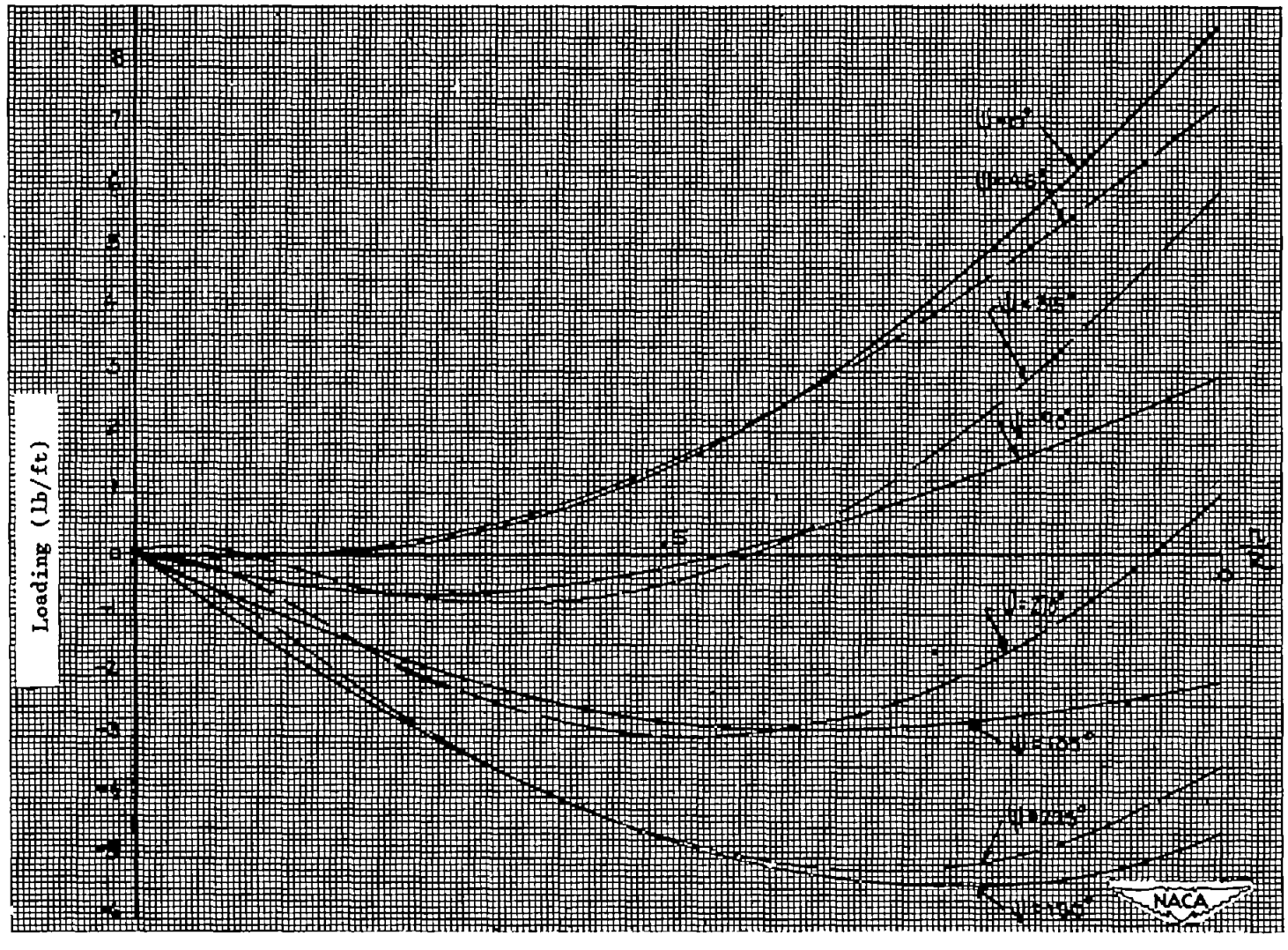

Figure 22.- Plot of total external loading on rotor blade at eight azimuth positions for the De Guillenchmidt method.

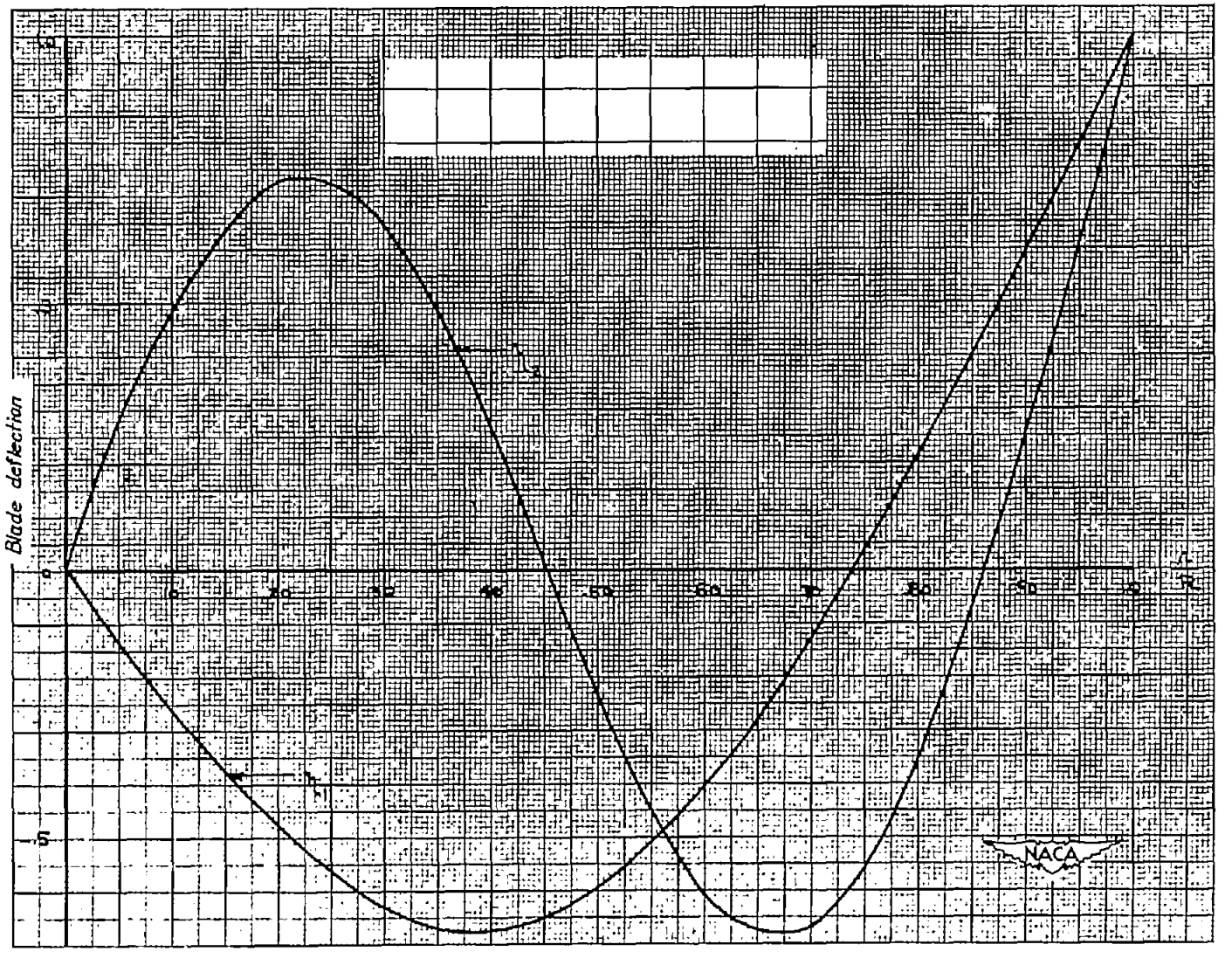

Figure 23.- Natural modes of rotor blade. Nonrotating; EI = 16,000 pound-inches^2; m' = 0.00603 slug per foot.

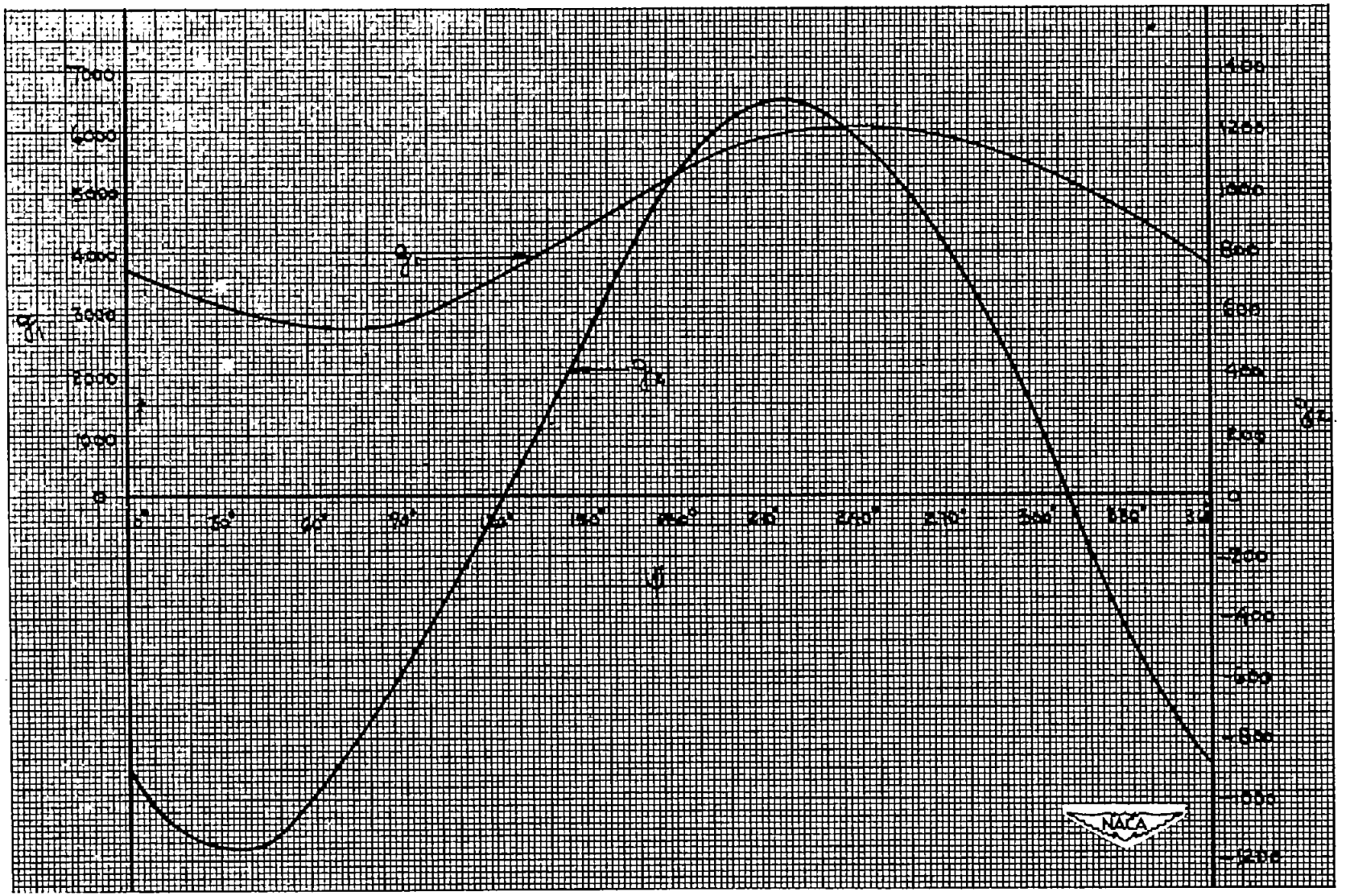

Figure 24.- Curves of g_1 and g_2 for De Guillenchmidt method.

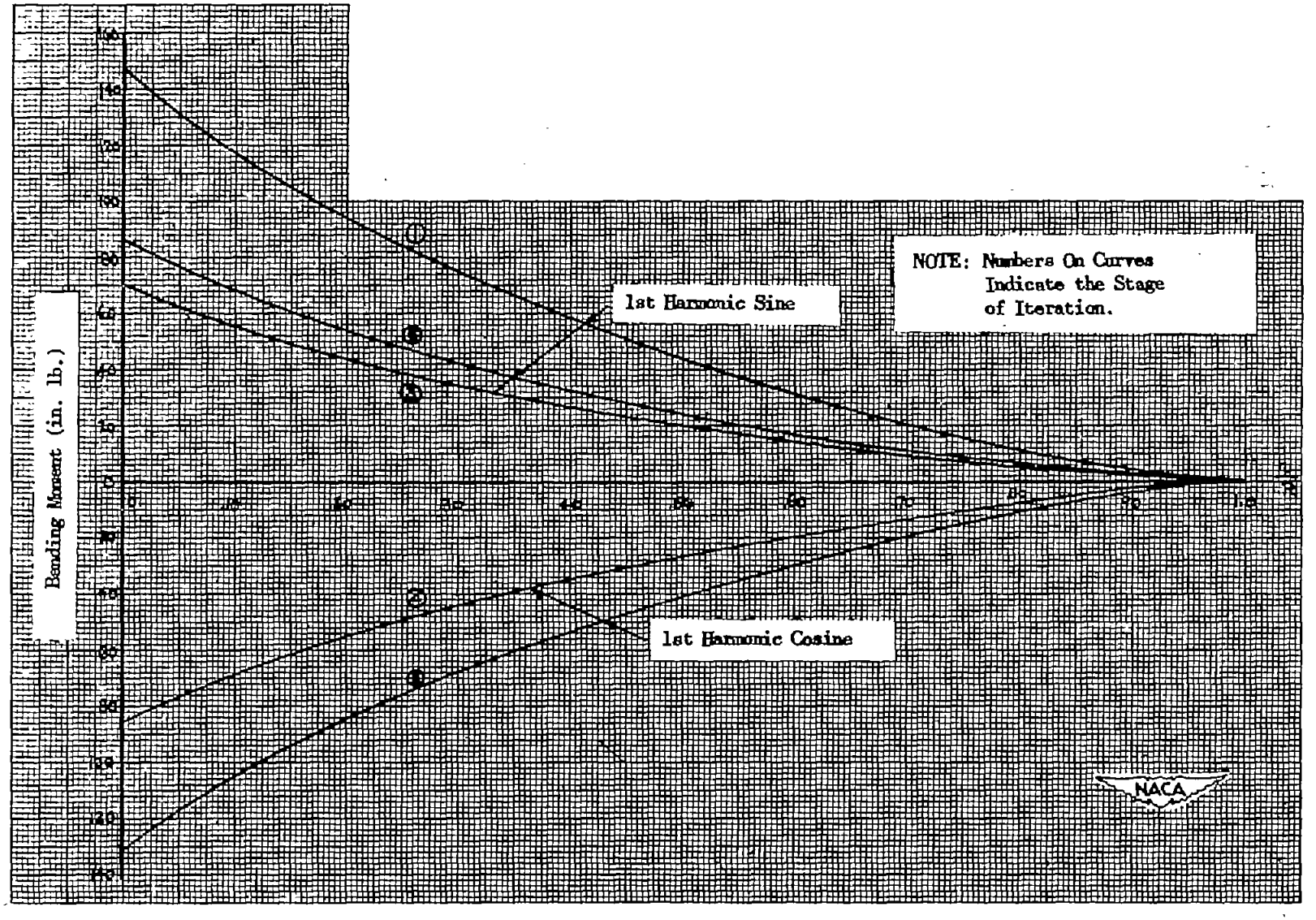

Figure 25.- Plot showing convergence of modified Goodyear method for calculating bending moment on a rigid rotor blade.

NACA-Langley - 2-23-53 - 1000